

ABSTRACT

Title of Document: MULTI-SCALE DYNAMIC STUDY OF
SECONDARY IMPACT DURING DROP
TESTING OF SURFACE MOUNT
PACKAGES

Jingshi Meng, Ph.D., 2016

Directed By: Professor Abhijit Dasgupta, Department of
Mechanical Engineering

This dissertation focuses on design challenges caused by secondary impacts to printed wiring assemblies (PWAs) within hand-held electronics due to accidental drop or impact loading. The continuing increase of functionality, miniaturization and affordability has resulted in a decrease in the size and weight of handheld electronic products. As a result, PWAs have become thinner and the clearances between surrounding structures have decreased. The resulting increase in flexibility of the PWAs in combination with the reduced clearances requires new design rules to minimize and survive possible internal collisions impacts between PWAs and surrounding structures. Such collisions are being termed ‘secondary impact’ in this study. The effect of secondary impact on board-level drop reliability of printed wiring boards (PWBs) assembled with MEMS microphone components, is investigated using a combination of testing, response and stress analysis, and damage modeling.

The response analysis is conducted using a combination of numerical finite element modeling and simplified analytic models for additional parametric sensitivity studies.

Drop tests are conducted for PWAs assembled with commercial off-the-shelf (COTS) Micro-Electro-Mechanical Systems (MEMS) microphone components under highly accelerated conditions of 20,000g (“g” is the gravitational acceleration). Under such high accelerations, the stress levels generated are well beyond those expected in conventional qualifications. Furthermore, secondary impacts of varying intensities are allowed by varying the clearance between the PWB and the drop fixture, to mimic unexpected secondary impacts in a product, if design rules fail to avoid such conditions. As a result, there are additional amplifications in stress and accelerations and reduction of repetitive drop durability. The amplification of the test severity is quantified using the characteristic number of drops to failure (η , Weibull distribution) of the population of tested MEMS components at each clearance. Multiple failure modes from drop testing are identified, ranging from package level failures to MEMS device failures. The participation of competing failure modes is also demonstrated via characteristic life representations of each failure mode at various clearances.

A multi-scale, dynamic, time-domain, finite-element analysis (FEA) approach is used to assess the response and stress histories at critical failure sites. A set of fatigue damage models is proposed, to predict the damage accumulation due to competing failure modes in MEMS components when subjected to drops with secondary impacts. The proposed damage accumulation model accounts for hydrostatic stresses

and for dynamic post-impact oscillations during each drop event. Based on the failure data and stress/strain outputs from FEA, fatigue damage model constants are determined for each failure mode when the components are facing downwards during the drop test. The proposed damage models not only provide a good fit to the measured lifetimes of the MEMS components, but also provide insights into the transitions in the dominant failure modes. This model (calibrated to failure data from drop durability of downwards facing components) is found to provide reasonable prediction of results for tests with components facing upwards.

Finally, a dynamic sensitivity study is carried out, using a simplified model structure, to gain parametric insights into the influence of secondary impact on the local stress histories at two typical failure sites in surface mount technology (SMT) PWAs. The selected model structure is an idealized representation of the MEMS PWA, to facilitate mechanistic insights using simplified analytic and numerical models. The two typical failure sites of interest included in this simplified model are representative of: (i) interconnects between the SMT component and the PWB; and (ii) miniature structures within the SMT component (e.g. MEMS diaphragm, runners, back-plate, wire bonds). The secondary impact parameters studied include: (i) width, shape, and magnitude of the impact pulse; (ii) laminated structure of the PWB; (iii) geometric constraints such as clearance magnitude and impact site; and (iv) contact stiffness. The results from this parametric study are compatible with the experimental evidence. This study clearly demonstrates the importance of accounting for the through-thickness oscillations of the PWB when considering different failure modes in SMT

components due to secondary impacts. In worst case scenarios, modeling the PWB as a shell element can introduce significant errors (5-50X, depending on the magnitude of damping) when predicting the response amplitudes of the internal miniature structures within the SMT component.

MULTI-SCALE DYNAMIC STUDY OF SECONDARY IMPACT DURING DROP
TESTING OF SURFACE MOUNT PACKAGES

By

Jingshi Meng

Dissertation submitted to the Faculty of the Graduate School of the
University of Maryland, College Park, in partial fulfillment
of the requirements for the degree of
Doctor of Philosophy
2016

Advisory Committee:
Professor Abhijit Dasgupta, Chair
Professor Amr Baz
Professor Patrick McCluskey
Dr. Michael Osterman
Professor Sung Lee (Dean's Representative)

© Copyright by
Jingshi Meng
2016

Acknowledgements

I deeply indebted to the support and guidance from my advisor, Professor Abhijit Dasgupta. He shaped my life, not only mentored me with his wisdom and vision in overcoming crucial academic and career turning points, but also as an example of a diligent scholar and a friend. I always feel honor to be his student.

I am grateful to all the committee members of my dissertation, Professor Amr Baz, Professor Patrick McCluskey, Dr. Michael Osterman, and Professor Sung Lee for their support and valuable suggestions to improve the quality of my work. Also, I would like to thank the Microsoft Mobile Oy (Nokia) team, Professor Toni T. Mattila from Aalto University, and the Lansmont Corporation for their assistance in board level drop testing in my research.

Additionally, I'd like to thank all the former and current A-Team members, CALCE sponsors and employees, and my friends in the Clark School, not only for their assistance and inspirations, but also for making my graduate school experience a fulfilled one: countless telecons, CALCE meetings, finals, reports, presentations, conferences, visiting research in Redmond ... and the list goes on.

Finally, I owe all the thanks to my parents, with all their support, love and encouragements that I always need.

Table of Contents

Acknowledgements.....	ii
List of Tables	vi
List of Figures	vii
Chapter 1. Introduction.....	1
1.1. Background and Motivation	3
1.2. Problem Statement	4
1.3. Literature Review.....	6
1.3.1. Drop Tests and Secondary Impacts.....	6
1.3.2. Fatigue Damage Modeling in Repetitive Drop Tests	10
1.3.3. Failures in MEMS Assemblies under Drop and Impact loading	13
1.3.4. Gaps in the Literature.....	16
1.4. Objectives of Dissertation.....	18
Chapter 2. Approach and Structure of Dissertation.....	21
2.1. Drop test reliability of MEMS assemblies with secondary impact.....	21
2.1.1. Experiments	21
2.1.2. System-level response simulation and stress analysis	21
2.1.3. Damage modeling for multiple competing failure modes	21
2.2. Detailed analysis of secondary impact on the dynamic response of competing failure modes.....	23
2.2.1. Impact Acceleration and PWB Flexural Strain.....	24
2.2.2. Through-thickness oscillation in PWB due to contact force	24
2.2.3. Dynamic response of competing failure modes resulting from secondary impacts.....	25
Chapter 3. MEMS Packaging Reliability in Board Level Drop Tests under Severe Shock and Impact Loading Conditions Part I: Experiment	26
3.1. Abstract.....	26
3.2. Introduction.....	28
3.3. Testing Approach.....	31
3.3.1. Secondary impact test setup & DMSA	31
3.3.2. Test vehicle and test matrix	36
3.3.3. Testing and failure analysis	37
3.4. Results and Discussion	40
3.4.1. Drop test failure sites of MEMS components.....	40
3.4.2. Characteristic life for MEMS component and each failure mode	45
3.5. Conclusions.....	50
Acknowledgement	51
Chapter 4. MEMS Packaging Reliability in Board Level Drop Tests under Severe Shock and Impact Loading Conditions Part II: Fatigue Damage Modeling.....	52
4.1. Abstract.....	52
4.2. Introduction.....	54
4.3. Modeling and Testing Methods	58

4.3.1.	Damage Models for Repetitive Drop Loading with Secondary Impacts	58
4.3.2.	Secondary impact test setup and test matrix	63
4.3.3.	Test specimen and multiscale finite element drop simulation	65
4.4.	Results and Discussions	70
4.4.1.	Failure modes and durability of MEMS components	70
4.4.2.	Simulation Results	72
4.4.3.	Damage modeling results.....	75
4.4.4.	Model Validation and Discussion.....	78
4.5.	Conclusion	82
	Acknowledgement	83
Chapter 5.	Influence of Secondary Impact on Printed Wiring Assemblies: Part I - High Frequency ‘Breathing Mode’ Deformations in the Printed Wiring Board	84
5.1.	Abstract	84
5.2.	Introduction.....	86
5.3.	Problem Statement and Approach	89
5.3.1.	Test Environments, Background and Flow Chart.....	89
5.3.2.	Calibration for secondary impact drop test model.....	91
5.3.3.	Loading Profile from Secondary Impacts	97
5.3.4.	Geometric Simplification in Thickness Direction	100
5.3.5.	Geometric Simplification: Micro-beam	102
5.3.6.	Amplitude Transfer Function.....	103
5.3.7.	Amplitude Estimation with Damping Ratio	106
5.4.	Results and Discussions	108
5.4.1.	Amplitude Response of 1-D PWB Model	108
5.4.2.	Correlation between pulse width and through-thickness oscillation response of PWBs.....	109
5.4.3.	Response of Micro-beam structure	112
5.5.	Conclusions.....	115
	Acknowledgements.....	117
Chapter 6.	Influence of Secondary Impact on Printed Wiring Assemblies Part II: Competing Failure Modes in Surface Mount Components	118
6.1.	Abstract	118
6.2.	Introduction.....	120
6.3.	Problem Statement and Approach	125
6.3.1.	Background and Approach	125
6.3.2.	Secondary Impact Model Calibration	127
6.3.3.	PWB Through-Thickness Resonance	129
6.3.4.	A 2-DOF Model for Two Typical Failure Sites of SMT	131
6.3.5.	Solutions of the 2-DOF Analytical Model.....	136
6.3.6.	Stress Estimation for FM-a and FM-b	138
6.4.	Results and Discussions	142
6.4.1.	Secondary Impact Model Outputs	142
6.4.2.	Responses of FM-a and FM-b to Input Accelerations	145
6.4.3.	The Sensitivity of each Failure Site to Secondary Impacts	149
6.4.4.	Experiments: Results and Insights	154

6.5. Summary and Conclusion	158
Acknowledgements	160
Chapter 7. Discussions and Summary	161
7.1. Conclusions	161
7.2. Contributions	164
7.3. Limitations & Future Work	166
Appendices	169
A1. MATLAB Code: Amplifications of x1 and x2 with Varying tp and fp	169
A2. MATLAB Code: γ of high frequency acceleration	173
A3. Laminated PWB's orthotropic property calculation	176
A4. Material properties used in simulation, Chapter4	180
Bibliography	184

List of Tables

Table 1: Drop test matrix (number of MEMS components).....	37
Table 2: Dominant failure site of MEMS microphone component at each drop test condition	42
Table 3: Drop test matrix (number of MEMS components).....	64
Table 4: Summary of relevant material properties	69
Table 5: Dominant Failure Sites in MEMS microphone component at each drop test condition	71
Table 6: List of model constants.....	76
Table 7: Characteristic life of each failure site, Experiment vs. Damage Modeling ..	77
Table 8: Characteristic life by failure site, estimated for components oriented upwards	78
Table 9: Dominant failure site, test vs. model	79
Table 10: Rayleigh Damping Coefficients	93
Table 11: Contact modeling parameters	96
Table 12: Material properties used in 1-D rod model.....	100
Table 13: Summary of Acceleration Response at Micro-beam Tip	110
Table 14: Parameters of the 2-DOF Model.....	133
Table 15: Outputs from the Secondary Impact Model.....	147
Table 16: Outputs from the 2-DOF Model	148
Table 17: Stress Estimations for FM-a and FM-b	149
Table 18: Experimental Results	155
Table 19: Material Properties for PWB Laminate	178
Table 20: Isotropic Elastic Material Properties	180
Table 21: Orthotropic Elastic Material Properties	181
Table 22: Plastic Material Property of Au	182
Table 23: Strain Rate Dependent Plastic Property of Solder (MPa).....	183

List of Figures

Figure 1: Objectives of this dissertation	18
Figure 2: Flowchart of Part I and Part II.....	22
Figure 3: Multi-scale dynamic response to Secondary Impact.....	23
Figure 4: Approach for Level 1 model material, damping, and contact parameters calibration	24
Figure 5: Drop tower with dual mass shock amplifier (DMSA) accessory	32
Figure 6: 20,000g acceleration history measured on top of DMSA	32
Figure 7: Finite clearance clamping method a. zero clearance b. infinite clearance c. spacers for finite clearance, d. schematic of secondary impact between PWA and fixture base.....	33
Figure 8: Drop orientations for MEMS microphone components	34
Figure 9: Test PWA with packages locations along the y axis and generic specimen design	35
Figure 10: Cross-section of MEMS microphone	36
Figure 11: Common drop test failure sites in MEMS package.....	38
Figure 12: Percentage of failure sites, for all 20,000 g tests with component oriented downwards	38
Figure 13: Failure site distribution for different clearances, components oriented down.....	41
Figure 14: Failure site distribution for different clearances, components oriented up.....	43
Figure 15: Unreliability vs. Time (cycles to failure) plot of tests at 20% clearance, package facing upwards	45
Figure 16: Drop durability results for MEMS assemblies	48
Figure 17: Drop durability results by failure sites, packages facing downwards	49
Figure 18: Flow chart of computation and validation for fatigue damage models (S-i: simulation; E-i: experimental analysis)	62
Figure 19: Acceleration amplifications setup based on secondary impacts	63
Figure 20: Test PWA with 6 packages located along the y axis of the PWB (Level 1 FEA model is also shown in the figure).....	67
Figure 21: Cross-section of MEMS microphone (Level 2 local model)	68
Figure 22: Common drop test failure sites in MEMS package.....	70
Figure 23: Calibration results of damping and contact parameters	71
Figure 24: Dynamic response output from critical failure site in die attach.....	72
Figure 25: Dynamic response output from critical failure site in solder	73
Figure 26: Dynamic bending strain response output from critical failure site in wire bond.....	76
Figure 27: Characteristic life of MEMS components, experimental vs. fatigue modeling results	80
Figure 28: Background and Approach	89
Figure 29: FE model for secondary impact tests	91
Figure 30: Free Vibration, Rayleigh Damping	93
Figure 31: Pressure-overclosure correlation, k is contact stiffness.....	96
Figure 32: Secondary impact, soft contact.....	97
Figure 33: Sample impact acceleration input to the PWB	97

Figure 34: Spectrum of Input pulses with different shapes	98
Figure 35: Multi-layered 1-D unit cell structure for PWB	99
Figure 36: Micro-beam model	102
Figure 37: Acceleration amplitude transfer function $H(\omega)$ obtained based on random vibration simulation (example condition: 3-layer model, $\zeta=0.04$)	104
Figure 38: Sample output from time domain simulation (3-layers PWB, $\zeta=0.04$, pulse shape=triangle, $t_p = 1.5E-5s$).....	105
Figure 39: Quantities used in the definition of amplitude ratio γ	106
Figure 40: Amplitude transfer functions for multi-layer PWBs	109
Figure 41: Amplitude ratio γ of high frequency acceleration	112
Figure 42: Background a) Secondary impact FEA model; b) Schematic of Test Setup; c) Simplified SMT Assembly and Its Loading Conditions.....	125
Figure 43: 2-Step Calibration Procedure and Results, PWB Strain.....	129
Figure 44: High Frequency Through-Thickness Response of Laminated PWBs to Secondary Impacts	131
Figure 45: 2-DOF Analytic Model with Two Competing Failure Modes	131
Figure 46: Parameter Extraction for Analytic 2 DoF Model from FEA Model of a MEMS Component	132
Figure 47: Transfer Functions of the 2-DoF Model.....	133
Figure 48: Sample Outputs from the 2-DOF Model, 1.2 mm Clearance, No trench, $\zeta_i=\zeta_a=\zeta_b=0.05$, $f_p=0.5MHz$	135
Figure 49: FEA Half-Symmetric Model for FA-b	138
Figure 50: Sample Contour Plot for FM-b.....	139
Figure 51: FEA Model for FA-a	142
Figure 52: Impact Acceleration Histories at the Footprints of SMT Packages, for Various Clearances	143
Figure 53: Acceleration from Direct (No Trench) and Indirect (With Trench) Impacts for 0.6 mm Clearance.....	144
Figure 54: PWB Strain underneath the Components.....	145
Figure 55: Amplifications of x_1 and x_2 for Impact Pulses with Various t_p and f_p Pulses, Based on Two Approximation of γ	148
Figure 56: Sensitivity of FM-a and FM-b to Secondary Impacts	150
Figure 57: Sensitivity of FM-a and FM-b to Direct and Indirect Impacts.....	151
Figure 58: Sensitivity of FM-a and FM-b to Clearance.....	152
Figure 59: Sensitivity of FM-a and FM-b to Contact Stiffness	153
Figure 60: Schematics of the Three Test Conditions.....	154
Figure 61: Sample Probability Density Function and Failure Mode	156

Chapter 1. Introduction

An increasingly important reliability concern in portable and hand-held electronic systems is failure under transient dynamic and vibration loadings caused by accidental drop and impact. In order to ruggedize product designs, drop testing has become an increasingly important technique to reproduce and accelerate such dynamic loading conditions. Understanding how such impacts can affect the functionality of the product is critically important in assessing and improving the robustness of portable electronic devices.

The ever-increasing density of packaging caused by continued miniaturization and increased functionality of modern electronic products, results in reduced spacing between neighboring structures and elements. Such a decrease in spacing has increased the risk of internal collisions between the structures inside the product housing: impact of circuit cards with each other, with internal surfaces of the product housing, with LCD screen, with battery case, etc. [1]–[4]. The internal collisions, termed “secondary impacts” in this dissertation, can significantly increase the severity of the impact in two ways: i) they can amplify the dynamic loads that are generated in conventional drop/impact loading by an order of magnitude [5], [6]; and ii) they can provide a new source of dynamic stress created by contact forces propagating from the contact site through the structure. Although product designers generally try to avoid possible secondary impact between internal structures in new designs, such secondary impacts are sometimes inevitable due to the complex and random nature of drop and impact loading conditions in the field. The current generation of accelerated

drop testing standards prevalent among electronics manufacturers (e.g. JEDEC-JESD22-B111 standard) quantifies reliability by counting the number of drops to failure at acceleration levels up to 2,900 g's, but does not address the role of secondary impacts. Therefore, developing a repeatable testing method which can be used to reproduce and accelerate such secondary impacts has become necessary.

According to the most widely adopted board-level-drop test standard JESD22-B111[7], rectangular PWBs are screwed on 4 stand-off metal columns at the corners of the PWBs which are mounted on the drop table of the drop tower. Stand-offs are designed sufficiently high so that no contact is expected between the PWB and the base plate during the drop test. Among the studies in literature using this test methodology [8], [9], [2], [10]–[14], failures in interconnects are mainly caused by large PWB bending strain. Due to the existence of secondary impact, the dynamic response of a PWB is different from the conventional drop tests in three different ways: 1. Accelerations are generally much higher than conventional drop tests with free vibration; 2. Participation of higher modes are more significant and complex; 3. Contact stress with a wide energy spectrum propagating through PWB can be very close to the package, interconnects, and microstructures.

The secondary impact method provides an option to conduct drop tests at acceleration ranges much higher than conventional drop towers can provide. Also, it can be used to test assemblies with much higher resonant frequencies (such as MEMS assemblies) which appear fairly rugged in conventional drop qualification tests [15], [16].

1.1. Background and Motivation

Portable electronic devices, such as smart phones, tablets, and laptops have become necessary social, recreational, and professional accessories. Naturally, better user experience is driving new products to be upgraded in functionality and decreased in overall weight, size, etc.

Modern portable electronic products utilize various surface mount technology (SMT) type MEMS: accelerometers, acoustic sensors, gyroscopes, magnetometers, radio frequency devices, etc. As the loading conditions of portable devices are dynamic, portable devices including the internal MEMS assembly have to be capable of sustaining sufficient number of drops and shocks. When secondary impacts occur in these products, relevant MEMS assemblies with miniature internal structures might be at risk.

The primary motivation of this dissertation is to facilitate durability assessment of SMT PWAs that experience secondary impacts during drop events. In a broader sense, a thorough understanding of the severity of secondary impacts and their influence on competing failure modes, is necessary. Such understanding is useful to guide product designs for eliminating or minimizing the failure risks of SMT assemblies that experience secondary impacts.

1.2. Problem Statement

SMT packages in portable devices are often indirectly subjected to shock loadings due to accidental drops. Relevant shock accelerations can range from tens of thousands to hundreds of thousands of g's. In standard drop tests (for example, JESD22-B111), since there is no contact between the PWB and the base plate, failures normally result from the combination of PWB bending strain and large inertial force.

Due to a combination of PWB large deformation and finite space with the surrounding structures, secondary impact may occur. Many sources of high frequency dynamic responses of the PWB can be excited by secondary impacts including high frequency deflection ($>1,000$ s Hz) and through-thickness oscillation (hundreds of kHz ~ MHz). Potential high transmissibility between the aforementioned high frequencies and resonant frequencies of the miniature structures in SMT assemblies (i.e. MEMS wire-bond ~tens to a hundred kHz, microstructure in MEMS device ~tens to a thousand kHz) can induce failure modes which are absent in standard drop tests.

An insightful survey is needed in order to understand the interactive dynamic response in miniature SMT packages (such as MEMS) due to secondary impacts. The following aspects of secondary impacts need further investigation:

- The influence of geometric constraints of secondary impacts on high impact accelerations;

- The dependence of the PWB's high-frequency response on material, damping, and lamination properties of the PWB, and on contact properties during secondary impact;
- The interactive dynamic response at different failure sites throughout the SMT assembly under secondary impacts to the PWB.

1.3. Literature Review

In view of the multi-scale architecture of electronic systems, three levels of drop and impact analysis have commonly been reported in the literature: product-level, board-level and package-level. Secondary impacts generated in the product level needs to be implemented in each consequential level to analyze its potential risks in hardware design. Then literatures on common failure modes in electronics under drop loading, drop test fatigue damage modeling studies, and drop test reliability and failure modes for MEMS assemblies are investigated. In the end, high impact acceleration, impact induced high frequency vibration and through-thickness oscillation, and their influence on damages in micro-structures in SMT packages are illustrated.

In view of the multi-scale architecture of electronic systems, three levels of drop and impact analysis have commonly been reported in the literature: product-level, board-level and package-level. Secondary impacts generated in the product-level needs to be implemented in each consequential levels to analyze its potential risks in hardware design. Then literatures on common drop test related failure modes, fatigue damage models are investigated. In the end, reliability of MEMS assemblies, high impact acceleration, impact induced high frequency vibration and through-thickness oscillation, and their influence on micro-structures failures are illustrated.

1.3.1. Drop Tests and Secondary Impacts

Product level drop test is designed to evaluate risks in a whole product during a drop event. Usually in product level drop test, the whole product is mounted to a drop carriage and allowed to undergo a guided free-fall in a drop tower. The product is

released from the drop carriage right before it hits the impact surface [9], [10], [17], [18]. Karppinen et al. [19] proposed another test method in which the whole product is half-constrained by guide rod and elastic bands, so that a product level free drop is performed onto a concrete contact surface with controlled velocities. To acquire data from the tests, load cells, strain gages, accelerometers, and high-speed cameras are usually used. Dynamic responses extracted from product level drop tests are essential references for characterizing the validity of finite element models [8], [9], [20]–[22]. However, product level drop tests are difficult to control and to analyze because of the uncertainties in quantifying the precise loading conditions, boundary conditions, component architecture, housing structure and material properties. For example, Lim, et al. [2], [9], Seah et al. [18] and Tan et al. [23] showed that the strains and accelerations in the PWB varied with the surface mount devices for the same drop orientation, and also varied with orientation for each PWB with the same surface mount device. Goyal, et al. [24], [25] showed that the shock response of the electronic product is dependent on its mass distribution. Moreover, even a single drop can result in a rather complex sequence of impacts (termed “clattering” in the literature (Goyal, et al. [17])). During “clattering”, the one corner that impacts first can significantly amplify the initial velocities of the other corners. The rapidly changing, extremely high net velocity causes series of velocity amplifications. Additionally, clattering of the product can lead to alternating shock that could cause resonance in suspended fragile components.

More recently, it has been reported that internal collision can be one of the reasons for internal, highly amplified contact stresses and accelerations resulting in damage to the

subsystems [1], [2], [26]. At the moment of impact, kinetic energy of a free-falling device converts into strain energy of both the external housing [1] and the internal structures of a device. These dynamic deformations combine with inertial forces caused by the mass of components to cause stress concentrations at the package interconnects ([9], [14], [19]). Studies of product level drop tests have shown that when a mobile phone is dropped on a hard surface from the height of 1.5 m, accelerations at the PWB level can reach 10,000g [26]. Therefore, drop test methods for producing acceleration impulses up to tens of 1,000g have received recent attention. Moreover, the dense packaging in high-performance, portable electronic products may generate internal collisions between the structures inside the product housing ([1], [2], [26]) after a shock event to the whole system. The concept of achieving high impact accelerations through the method of momentum transfer and velocity amplification during impacts between moving bodies were investigated by Hart and Hermann [27], Harter et al. [28] and Kervin [29]. A velocity amplifier method has already been commercialized for drop tests to achieve high accelerations, based on the dynamics of velocity amplification through pair-wise collisions between multiple masses in a chain [30], [31].

There have been several published board level drop test standards in recent years. These drop standards attempt to mimic the shock impact experienced by the PWA inside the product when it is dropped [7], [32]–[34]. For example, in JEDEC standards [7], the PWA is mounted horizontally on the drop table fixed with four or six screws. The drop table is then released from a defined height and dropped vertically along the guide rods onto the impact surface. At the moment of impact, the

PWA starts vibrating at its natural frequencies, induced by the transient impact excitation. The PWA response, according to Jing-en, et al. [35] and Wang, et al. [36], depends on the input impact force, boundary conditions (such as tightness of the screws), contact property of the impact surface, etc. Many other options to perform board level drop tests have been proposed during the past decade. One option is to constrain the PWA to remain stationary while a moving mass impacts the PWA. For example, pendulum style test setup [12] has been used to impact a constrained PWA in the in-plane and out-of-plane orientations. Varghese et al. [13] proposed a high-speed four point bending test to evaluate drop durability. The effectiveness of this test method in reproducing interconnect reliability of solder in drop test is based on the assumption that damage to the solder due to inertia force is negligible when compared with damage due to PWA curvature [37]. To implement secondary impacts in board level drop test, Douglas et al. [4] demonstrated that secondary impacts can cause a significant amplification of accelerations at the impact site by conducting a simplified analysis of a two degree-of-freedom spring-mass system. Douglas et al. [4] and the present author have shown [6], using experiments and FEA, that one of the sources of the amplification of acceleration is potentially related to the generation of multiple dynamic mode shapes of the PWB due to the secondary impact.

In terms of failure modes, in typical board level drop tests without secondary impact that are specified in most industry standards (e.g. [7]) for conventional IC packages [9], [2], [10]–[13], failures at package interconnects are mainly caused by large PWB bending deformation and inertial forces due to the mass of internal structures. Studies on drop durability of different solders have revealed that eutectic Sn-Pb solder joints

generally have better performance than Pb-free solder joints [38], [39][40]. Drop durability of Pb-free solders are also influenced by factors such as composition [41], solder finish [42], [43]–[45] Kirkendall voids induced by thermal cycling [46], and interfacial microstructure evolution in the interconnects after thermal aging [47]. By contrast, drop tests with secondary impacts can significantly increase the severity of the primary impact in two ways: i) amplification of the dynamic loads discussed above, ii) creation of a new source of stress pulse at the contact site and propagation of the stress wave through the structure. Since the drop tests in the current literature are mostly reported without secondary impacts, identifying the reliability of MEMS components assembled on PWBs under severe shock loading conditions with secondary impacts is an important, relatively new, as well as challenging task.

1.3.2. Fatigue Damage Modeling in Repetitive Drop Tests

For the last few decades, a significant amount of effort has been made to understand damage due to dynamic loading, such as shock and vibration loading, in many applications, such as consumer electronics [12], missile launch/gun fire [48], occupant safety during vehicle collisions [49] [50], random vibration induced fatigue of aircraft parts, shock and vibration in oil drilling environments, etc. In particular, the focus in this study is on portable electronic devices because they are commonly exposed to shock and impacts due to accidental drops.

To assess the drop test reliability of SMT components, typical empirical and analytical approaches were both used. Due to extensive computational expenses, a fracture mechanics based approach is generally not preferred in practice for

generating fatigue curves. Similarly, the “Damage boundary” method [51], [52] [53] which maps entirely based on experimental data is also not preferred because of its empirical, design-specific nature. By contrast, risk assessment methods based on local dynamic response at failure sites can significantly improve the prediction capability and efficiency. For example, such procedures has been conveniently applied to compare the influence of different test parameters in drop tests, such as boundary conditions [54], drop heights [55] and drop orientations [2].

In mechanics-based models, the damage metrics need to be selected as failure envelopes. A popularly used approach is based on selected metric variables (such as peeling stress [55][56], von Mises’ stress or strain, plastic strain [57], displacement and acceleration) extracted from the most critical locations [57] in an assembly. To extract the damage metrics parameters, FEA are normally relied on. Therefore, accuracy and capabilities of material models are needed. For example, different types of solder alloys used in electronic systems have been modeled as rate independent elastic materials [36], rate dependent elastic materials [58] and rate dependent bilinear material [57], over a wide range of strain rates from $E^{-4}/s \sim E^{+2}/s$.

Various types of fatigue models based on local material response have been developed in the past decades to evaluate the damages accumulated at each loading cycle. Typical fatigue models used in the electronic packaging field can be classified into two categories: stress- or strain- based [59], [60] and energy based [61], [62]. For its simplicity, elastic-plastic stress/strain based fatigue models are often adopted in

drop and shock analysis [63] [12] [64]. Classical fatigue models, such as Miner's rule for damage accumulation, Basquin-Coffin-Manson's (total strain) fatigue model [65] [66], [67], [61] and Engelmaier's model, are modified or directly used, with stress, strain values obtained experimentally and numerically. Selected metric variables, including peeling stress [63], shear equivalent stress or plastic strain [59], [60], are extracted from critical failure sites (i.e. solder joints).

To account for damages accumulated during multiple, consecutive cycles after a shock or impact, Varghese and Dasgupta [12] proposed a fatigue life model for interconnects on PWAs in ball-impact tests where PWA reversals at different natural frequencies during and after impacts are considered. Summation of accumulated damage for over 20 milliseconds was effectively conducted. A similar approach was used by Lall, et al. [64] for fatigue life estimation of solder joints in BGA under JEDEC22-B111 standard drop tests.

Often times, fatigue life is also influenced by hydrostatic stress because damage accumulation procedure can be inhibited by compressive hydrostatic stress and facilitated by tensile hydrostatic stress [62], [68]. Bridgman [68] and McClintock et al. [69] showed the considerable effect hydrostatic stress had on shear strength of most of the commonly used metals. Morrow et al [62] experimentally proved that a compressive mean stress enhances the fatigue life while a tensile mean stress shows the opposite. Brownrigg. et al, [70], in a metallography study of spheroidized 1045 steel, explained such a mechanism of hydrostatic stress that it severely retards the

nucleation and growth of voids near carbide particles. The effect of hydrostatic stress is also evidenced in board level drop tests. For example, in JEDEC22-B1111 standard drop tests, components mounted on top of the PWAs would usually sustain less damage than components mounted on the bottom [5], [63] because, even though similar strain amplitudes are expected at the footprints of solder joints, the hydrostatic stresses are different due to inertia forces from the component. To implement the observed hydrostatic stress effect on damage accumulation rate in materials, Socie and Morrow [71] added a mean stress correction factor σ_m to the high cycle fatigue term of the Basquin-Coffin-Manson fatigue model. Manson and Halford [72] argued the mean stress effect should be accounted for low-cycle fatigue as well. Varvani [73] introduced a tensile mean stress correction multiplier to address the additional fatigue damage of silicon due to mean normal stress applied to the critical plane of silicon, which writes as $(1 + \sigma_n^m / \sigma_f')$, where σ_n^m denotes the mean stress and σ_f' stands for a reference stress value termed axial fatigue strength coefficient.

1.3.3. Failures in MEMS Assemblies under Drop and Impact loading

MEMS components are widely utilized in many different applications, such as sensors, portable consumer electronics, radio frequency switches, and power devices in automotive, aerospace and military electronics. MEMS packages contains not only interconnects in first- and second- level packaging, but also microstructures. Dynamic responses of miniature moving structures in SMT assemblies (such as MEMS) [15], [16], [74] exposed to shocks and drops can cause challenging reliability issues [75][76].

Mariani et al. [77] investigated stress concentrations and fractures in brittle materials used in MEMS devices by conducting a detailed multi-scale simulation. The simulation levels ranged from MEMS package level drop tests to micro-scale crack propagation in polycrystalline microstructures. Bomidi et al. [78] studied fatigue damage and life scatter of polycrystalline metallic structures used in MEMS devices. The simulation effort includes crack initiation, propagation, and coalescence in bending fatigue tests based on continuum damage mechanics. The dominant failure mechanism in MEMS components varies depending on the structures of specific MEMS designs and loading conditions [79]. According to Srikar and Senturia [16], MEMS packaging alleviates the severity of the shock pulse, therefore the substrate was assumed as a rigid body to model the worst-case scenario. Whereas Ghisi et al. [80] showed that MEMS packaging can significantly increase the occurrence of failures when the bottom surface of a MEMS accelerometer package is subjected to a shock. Alsaleem et al. [81] pointed out that the presence of second level packaging for MEMS devices may further amplify the dynamic response of the miniature structure. This is particularly significant when the frequency of the microbeam's higher order mode is close to the natural frequency of the PWB and is within the shock pulse's energy spectrum. Tilmans et al. [82] reviewed various types of packaging relevant to MEMS and emphasized the importance of MEMS packaging to MEMS reliability.

Since MEMS components are commonly designed with high resonant frequencies [83]–[86], they appear rugged in ordinary ranges of operating frequency or in conventional drop qualification tests. Sheehy et al. [87] reported that micro-scale cantilevers were generally durable in common drop tests. Failures were insignificant

unless the shock acceleration exceeded 40,000g. Srikar and Senturia [16] studied the transient response of MEMS devices to a shock pulse at the silicon substrate. From the point of view of the microstructure's natural frequency, most shock loads experienced by MEMS devices are quasi-static due to the relatively long shock pulse's width. However, if the contact surface is too rigid, excessive deformations and failures in microstructures may occur even if the drop is just from an ordinary height. Li and Shemansky [15] analyzed the failure risks in a cantilever beam-type, micro-machined structure when subjected to a free fall onto a rigid surface. An idealized equivalent acceleration of up to 10^5 g's from a 1.2 m drop can result in a high failure rate. Ghisi et al. [80] conducted a multi-scale simulation study and analyzed the contribution of electronic packaging to the reliability of MEMS sensors when subjected to accidental drops from 150 cm in height. According to Ghisi, stress waves propagating and reflecting through the package can amplify the acceleration experienced by the miniature structure up to a multiple of 10^7 g's. The collisions between the miniature structure and a cavity limited by the electronic packaging were believed to be one source of high accelerations.

High frequency oscillations often occur in stress wave propagation problems. One major source is geometric dispersion [88]. However, if stress distribution perpendicular to the direction of wave propagation is uniform, the effect of dispersion should be negligible [89]. Another reason a stress induced acceleration pulse can cause high frequency oscillations is the heterogeneity of infinite or semi-infinite laminated materials [90]–[92]. When a finite-length media is being considered, stress waves from free-boundary reflection will be superimposed (i.e. [93]) to form elastic

vibrational signals. To some extent, as the dimension decreases, frequency of such vibrational signals increase. Even though such signals decay to negligible amplitudes soon after the shock event due to damping, hundreds of noticeable reversals still appear at high oscillation frequencies within a short duration. Kimberley et al. [94] studied the effect of impact acceleration profiles (generated by Split-Hopkinson bar tests) on the reliability of MEMS components. Kimberley et al. reported the history of impact acceleration to be equally important as the peak itself. Therefore, it becomes necessary to understand the impact-induced high frequency oscillation in PWBs and its consequential effect on failures in SMT packaging.

From secondary impacts, contact force with a short pulse duration (tens of microseconds) applied to PWBs can be very close to the footprint of packages mounted on its top. As a result, various sources of PWB's high frequency responses can be induced: high mode (kHz) PWB deflection and high frequency (MHz) oscillations in the through-thickness direction of PWB. It should be noted that the frequency range in the latter case is already close to the natural frequencies of many MEMS applications [83]–[86]. Consequently, the dynamic responses of the system are likely to have more contributions from higher frequency modes.

1.3.4. Gaps in the Literature

- **Experiment:** No available database for drop test durability and related failure mode of PWAs under secondary impact
 - Repeatable test strategies are needed for controlled secondary impacts
 - Better understanding is needed for MEMS failure modes

- **Response Modeling:** Inadequate understanding of all the dominant sources of stress under secondary impact condition, hence no guidelines for design or qualification testing
 - Response analysis: modeling strategies for secondary impact
 - The influence of contact properties on impact pulse and on PWB deformation
 - Role of dynamic “breathing mode” of laminated PWBs on response of SMT packages

- **Damage Modeling:** Limited capabilities of currently available mechanistic damage models for drop durability
 - Effects of drop orientation: there is a lack of unified damage modeling strategy that accounts for the effect of drop orientations on damage accumulation rate
 - Dynamic response after each drop event: most available drop durability models do not consider the response past the 1st half cycle
 - Multiple competing failure modes: no currently available unified drop durability modeling framework can capture it

1.4. Objectives of Dissertation

This dissertation focuses on the influence of secondary impacts on the failure risks in surface mount assemblies. To achieve this goal, detailed multi-scale analytical, numerical and mechanistic-damage models are developed. The dissertation consists of three parts, as shown in Figure 1.

In Part I, the reliability of a selected COTS MEMS microphone assembly is evaluated by testing, failure analysis, and statistical analysis. Part II adopted a mechanistic damage modeling approach to explain the experimental findings in Part I. Part III further examines the influence of secondary impact on a more generic representation of SMT packages assembled on PWBs.

I: Reliability of MEMS assemblies in drop testing with secondary impact		
Board level drop test with MEMS assembly	Failure analysis and statistical analysis of failure data	
II: Mechanistic damage modeling of failure modes in MEMS assemblies		
Multi-scale drop test simulation (“input-g”)	Damage models (Multiple competing failure modes)	
III: Detailed insights and parametric study to understand the effect of secondary impact on the dynamic response at competing failure sites of SMT		
PWB flexural deformation	Hierarchy resonant amplifications (acceleration) of miniature structures	Displacement & stress concentrations at competing failure sites of SMT

Figure 1: Objectives of this dissertation

Part I is carried out to investigate *drop test durability and failure modes* of a selected SMT assembly. Standard drop tests (as per JESD22-B111) do not include any secondary impacts. Therefore, it is necessary to experimentally study leading failure modes in PWA SMT packages and in MEMS devices, under repetitive drop loading with secondary impacts.

In Part II, a *mechanistic-based damage model* is developed to quantify repetitive impact induced damage accumulation at competing failure sites, with the following considerations in the model:

- Effect of drop orientation: Majority of the durability models used in drop tests do not consider the effect of tensile or compressive stress states. This is a limitation for interconnect materials like solder.
- Dynamic response after each drop event: Each drop event causes multiple cycles of PWB vibration response. Most available drop models do not consider the response past the 1st half cycle.
- A generic drop test damage model for three competing failure modes: Most existing board-level-drop test studies have mainly focused on the interconnect failure mode; mechanistic-based damage models available for other relevant first-level and second-level packaging failure modes (e.g. wire bond, die attach) are rarely developed for drop test conditions.

Part III is an in-depth study to analyze the detailed dynamic response of the PWB and at competing failure sites due to: (i) amplification of inertial forces from high impact accelerations; (ii) changes in PWB flexural modes; and (iii) secondary impact induced PWB through-thickness oscillation. Interconnects and microscale structures (as two possible failure sites in SMT assemblies) were thus far only independently investigated in most of the relevant analysis ([15], [16], [81]) without considering the possible interactions between them.

Part III is intended to address the following objectives:

- The influence of contact properties on impact acceleration and on PWB flexural deformation.
- “Breathing mode” high frequency oscillation of laminated material in thickness direction.
- Resonant amplifications of damages in miniature SMT structures due to the “breathing mode” behavior after secondary impacts on laminates.

Chapter 2. Approach and Structure of Dissertation

This dissertation has three parts, as presented earlier in Section 1.4. The approach for Part I and II is to be presented in Section 2.1 and detailed discussion will be available in Chapters 3 and 4. The approach for Part III is to be overviewed in Section 2.2 and in detail in Chapters 5 and 6.

2.1. Drop test reliability of MEMS assemblies with secondary impact

The overall approach for Part I and II follows the flowchart in Figure 2.

2.1.1. Experiments

This part of the study includes: test method and test matrix development, specimen and fixture design, drop testing, post-test analysis of failure modes, and statistical analysis of failure data. This part of study is presented in detail in Chapter 3.

2.1.2. System-level response simulation and stress analysis

In this step, a detailed multi-scale 3-D FEA model has been developed. It involves model calibration using dynamic strain readings from PWB and identification of the critical failure sites and model outputs. This part of study is presented in detail in Chapter 4.

2.1.3. Damage modeling for multiple competing failure modes

Based on the von-Mises' strain and hydrostatic stress at each failure mode, a damage model is proposed for repetitive drop testing. Model constants are obtained from test data for each failure mode. This part of study is presented in detail in Chapter 4.

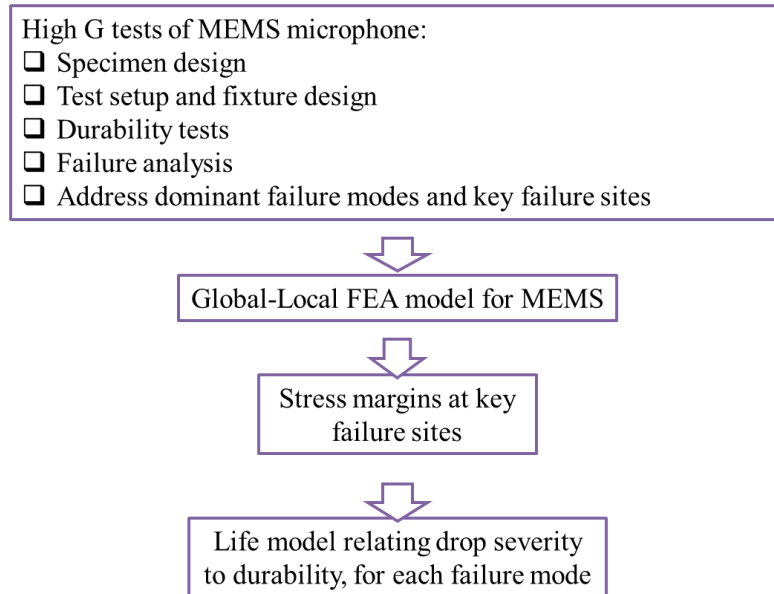


Figure 2: Flowchart of Part I and Part II

2.2. Detailed analysis of secondary impact on the dynamic response of competing failure modes

The general approach for detailed dynamic analysis of secondary impact in board-level-drop tests and competing failure modes is shown in Figure 3. Three length scales are considered in this study, defined with reference to JESD22-B111 [7]:

Level 1: a length scale of the in-plane dimensions of a typical PWB (roughly tens to more than a hundred millimeters)

Level 2: a length scale of typical MEMS packaged components and the overall height of a typical PWB, interconnect, and die (roughly one to a few millimeters)

Level 3: a length scale of each lamina of the PWB (usually ranges from tens to hundreds of microns)

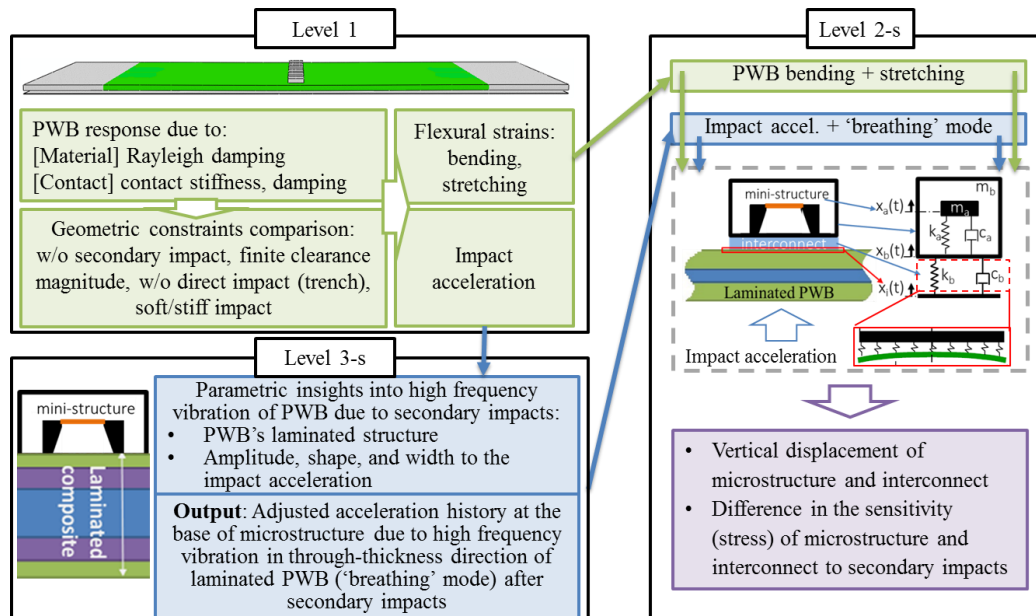


Figure 3: Multi-scale dynamic response to Secondary Impact

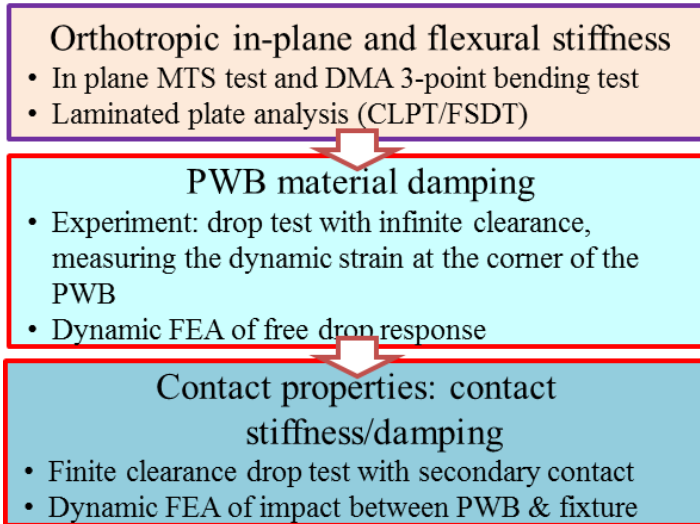


Figure 4: Approach for Level 1 model material, damping, and contact parameters calibration

2.2.1. Impact Acceleration and PWB Flexural Strain

A two-step calibration method is adopted to calibrate the PWB dynamic behavior under secondary impact. First we calibrate the two Rayleigh damping coefficients of the PWB material, by parametrically comparing the bending strain from FEA with dynamic strain readings from a free vibration experiment. The next step is to calibrate the contact stiffness and critical damping fraction between the PWB and the fixture. The parameters are obtained by comparing experimentally measured strain history from a finite clearance test with the bending strain history from FEA. This is a Level 1 length scale study and will be presented in detail in Chapter 5.

2.2.2. Through-thickness oscillation in PWB due to contact force

This is a Level 3 length scale study based on a frequency domain analysis. The impact acceleration traverses from the contact site at the bottom of the PWB to the

component on the top side of the PWB. This part of study is presented in detail in Chapter 5.

2.2.3. Dynamic response of competing failure modes resulting from secondary impacts

The goal of this section is to correlate the dynamic response of two competing failure modes in a generic SMT assembly with the participation of PWB flexural modes. Inputs are taken from both Level 1 and Level 3 models. This part of study is presented in detail in Chapter 6.

Chapter 3. MEMS Packaging Reliability in Board Level

Drop Tests under Severe Shock and Impact Loading

Conditions Part I: Experiment

This chapter presents the experimental topics of repetitive drop tests with secondary impacts, including: test method and test matrix development, specimen and fixture design, drop testing, post-test analysis of failure modes, and statistical analysis of failure data. Some preliminary test results in this chapter was published as a conference proceeding in the 13th IEEE ITherm Conference. The current draft of this chapter is submitted to Transactions on Components, Packaging and Manufacturing Technology for peer-review.

3.1. Abstract

The continuing increase of functionality, miniaturization and affordability of handheld electronic devices has resulted in a decrease in the size and weight of the products. As a result, printed wiring assemblies (PWAs) have become thinner and more flexible, and clearances with surrounding structures have decreased. Therefore, new design rules are needed to minimize and survive possible secondary impacts between PWAs and surrounding structures, because of the consequential amplification in acceleration and contact stress. This paper is the first of a two-part series and focuses on drop test reliability of commercial off-the-shelf (COTS) Micro-Electro-Mechanical Systems (MEMS) components that are mounted on printed

wiring boards (PWBs). Particularly in this paper, we are interested in gaining preliminary insights into the effects of secondary impacts (between internal structures) on failure sites in the MEMS assemblies. Drop tests are conducted under highly accelerated conditions of 20,000g (“g” is the gravitational acceleration). Under such high accelerations, the stress levels generated are well beyond those expected in conventional qualification tests. Furthermore, secondary impacts of varying intensities were allowed by changing the clearance between the PWB and the fixture. As a result, the stress and accelerations are further amplified, to mimic unexpected secondary impacts in a product if/when design rules fail to avoid such conditions. The amplification of the test severity is quantified by comparing the characteristic life (η in a Weibull distribution) of all tested MEMS components at each clearance. Multiple failure sites from drop testing are identified, from packaging level failures to MEMS device failures. The participation of competing failure sites is also demonstrated via characteristic life representations of each failure site at various clearances.

Index Terms— MEMS, Repetitive drop test, Secondary impact, Ultra-high acceleration, Durability, Failure sites

3.2. Introduction

MEMS components are widely utilized in many different applications, such as sensors, portable consumer electronics, radio frequency switches, and power devices in automotive, aerospace and military electronics. Use conditions for MEMS-based microsystems can be rather harsh in some applications (especially in sensing applications), such as harsh chemicals, extreme thermal and humidity environments, shocks and drops [75]. In particular, portable electronic devices are commonly exposed to impact loading due to accidental drops, therefore reliability of MEMS assemblies under shock and impact is critically important. Especially, the dynamic response of moving parts in MEMS [2], [3] makes identifying the root causes of failures in MEMS assemblies a very challenging task.

At the moment of impact, kinetic energy of a free-falling packaged device converts into strain energy of both the external housing [1] and the internal structures of a device. These dynamic deformations cause stress concentrations at the interconnects in the package ([9], [14], [19]). Studies of product level drop tests have shown that when a mobile phone is dropped on a hard surface from the height of 1.5 m, accelerations at the PWB level can reach 10,000g [26]. Therefore, drop test methods for producing acceleration impulses of the order of 10,000g have received recent attention. Moreover, the dense packaging in high-performance portable electronic products may generate internal collisions between the structures inside the product housing ([1], [2], [26]) after a shock experienced by the whole system. Such internal collisions, termed “secondary impact” in this discussion [4], could possibly happen

between slender circuit cards and other relatively rigid internal surfaces, such as product housing interior, displays, battery case, etc. Typical board level drop tests specified in most industry standards (e.g. [7]) for conventional IC packages [9], [2], [10]–[13] have no secondary impacts. In such tests, failures at package interconnects are mainly caused by large PWB bending deformation and inertial forces due to the mass of internal structures. By contrast, drop test with secondary impact can significantly increase the severity of the primary impact in two ways: i) amplification of the dynamic loads discussed above, ii) creation of a new source of stress pulse at the contact site and propagation of the contact stress wave through the structure.

Hart and Hermann [27], Harter et al. [28] and Kervin [29] investigated the concept of achieving high impact accelerations through the method of momentum transfer and velocity amplification through impacts between moving bodies. A velocity amplifier method is already commercially available as a shock test methodology to achieve high accelerations, based on the dynamics of velocity amplification through pair-wise collisions between multiple masses in a chain [30], [31]. This commercial device is termed a Dual Mass Shock Amplifier (DMSA) Douglas et al. [4] demonstrated that secondary impacts in a DMSA can cause a significant amplification of accelerations at the impact site, by conducting a simplified analysis of a two degree-of-freedom spring-mass system. Douglas et al. [4] and Meng et al. [6] have shown that one source of amplification in acceleration might be the multiple dynamic mode shapes of the PWB excited by the secondary impact.

Drop test reliability of MEMS is a fast growing field of research. Li and Shemansky [15] analyzed the failure risks in micro-machined structure when subjected to a free

fall drop. The theoretically calculated impact acceleration can be up to 10^5 g's from only a 1.2 m free fall to a hard surface. As a result, the micro-machined structure in the experiment encountered high failure rate. Sheehy et al., [87] reported that micro-scale cantilevers are generally durable in common drop tests, failures appear to be significant only when the input acceleration is as high as 40,000g.

The dominant failure mechanism in MEMS systems (e.g., silicon fracture, stiction, contamination) varies depending on the MEMS design and loading condition [79]. Srikar and Senturia [16] studied the transient response of MEMS devices due to a shock pulse applied to the silicon substrate. According to Srikar and Senturia, the package design in a MEMS assembly can alleviate the severity of the shock pulse, and they were therefore able to model the worst-case scenario by assuming the substrate to be a rigid body. On the other hand, Alsaleem et al. [81] pointed out that the presence of second level packaging for MEMS devices may further amplify the dynamic response of the microstructure mounted on its top. Tilmans et al. [82] reviewed various approaches for MEMS packaging, from wafer level (0-level) to chip level (1-level) packages, and emphasized the importance of MEMS packaging in MEMS reliability. In view of the importance of the package design, this study focuses on fully packaged MEMS assemblies rather than on bare MEMS devices.

In this work, we quantitatively demonstrate that drop testing of a PWA with MEMS microphones causes packaging related failures more often than MEMS device failures. In addition, this study highlights a transition of the dominant failure site as a function of clearance between the PWB and the fixture underneath.

3.3. Testing Approach

In this section, the test setup and test matrix for high-acceleration (of the order of 10,000g) drop testing are introduced.

3.3.1. Secondary impact test setup & DMSA

The setup for high-acceleration drop testing in this study is developed based on the principle of multiple secondary impacts. One secondary impact occurs at the DMSA (dual mass shock amplifier, a commercial accessory of the drop tower, as shown in Figure 5 [95], [96]). The other secondary impact is from the dynamic contact between the PWA and the fixture when the PWB deflection exceeds the designed finite clearance between them. Thus, including the primary impact, there are three consecutive impacts in this drop testing setup, to enhance the acceleration magnifications in the board level drop test.

As shown in Figure 5, the tester consists of a drop table on four primary guide rods, a seismic base on four shock absorbers, the DMSA accessory and various pulse shaping materials. Pulse shaping materials help to determine the magnitude and duration of acceleration profiles. The DMSA accessory consists of a base rigidly mounted to the top of the drop table, and a secondary drop table suspended on four secondary guide rods by four linear springs. The drop table falls along the guide rods, from a given height onto the seismic base. The primary impact between the drop table and the seismic table is capable of producing repeatable impact accelerations up to 5,000g at the DMSA base. Secondary impact is produced by the impact between the DMSA

drop table and the DMSA base, to achieve almost 20X amplifications of the acceleration level at the DMSA table (producing accelerations up to 100,000g).

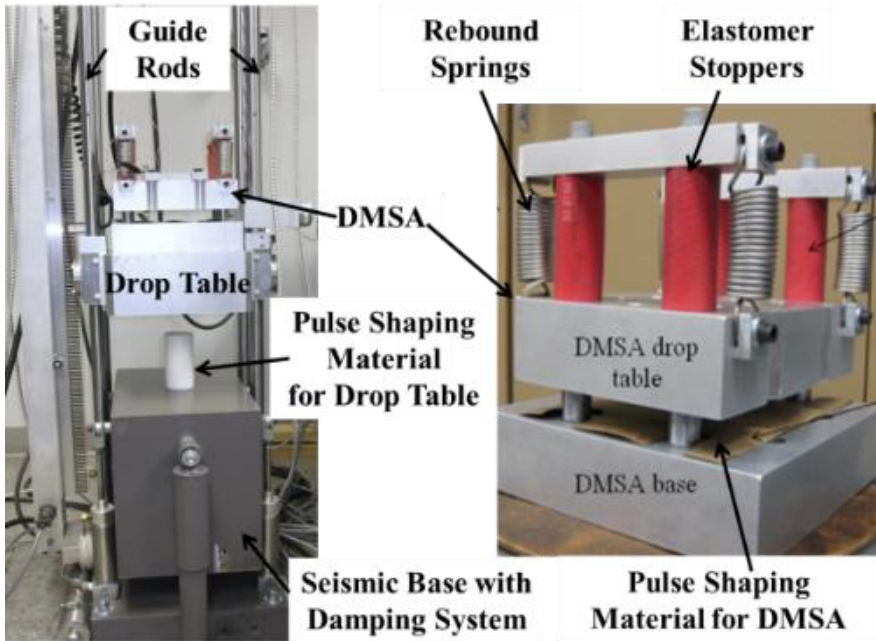


Figure 5: Drop tower with dual mass shock amplifier (DMSA) accessory

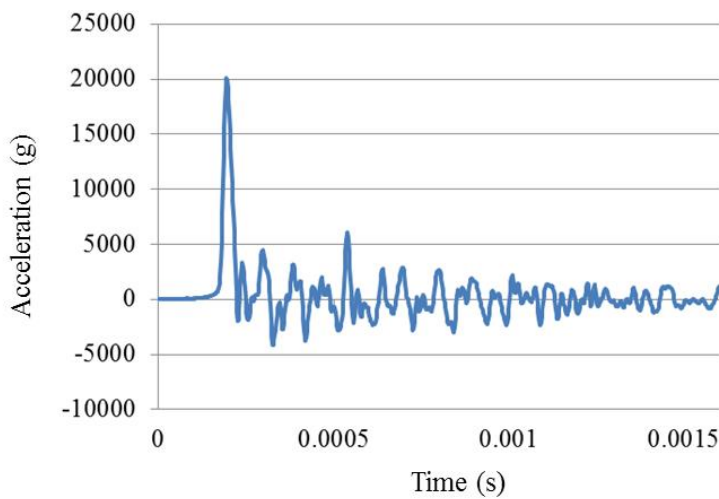


Figure 6: 20,000g acceleration history measured on top of DMSA

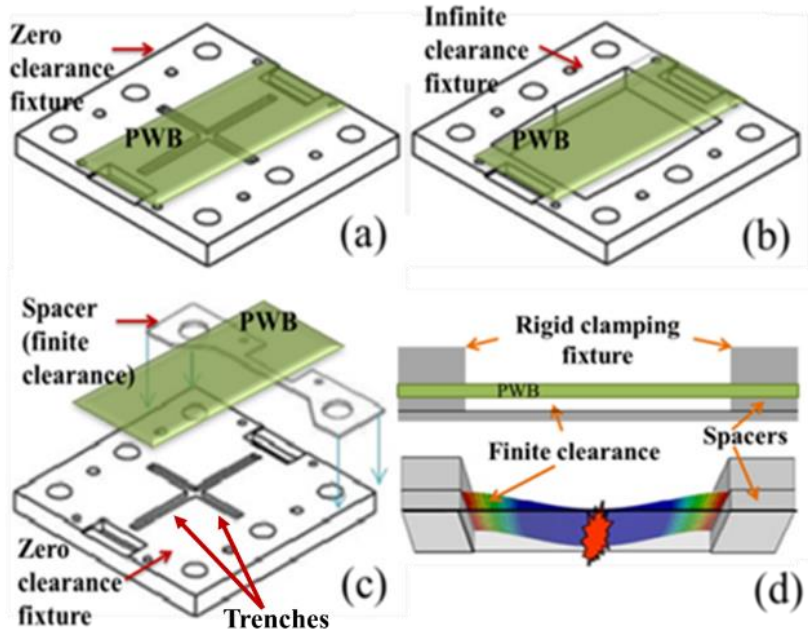


Figure 7: Finite clearance clamping method a. zero clearance b. infinite clearance c. spacers for finite clearance, d. schematic of secondary impact between PWA and fixture base.

As discussed in prior studies by the authors [97], the magnification of acceleration (left term in Equation 1) is determined by a stiffness ratio and a mass ratio of the system. The stiffness ratio is defined base on the properties of two pulse shaping materials: K_1 (placed between the contact pair of the primary impact) and K_2 (placed between the contact pair of the secondary impact). The mass ratio is taken from two impacting parts: DMSA base and drop table as one part (M_1), DMSA table and fixture as the other part (M_2). A sample acceleration history measured on top of the DMSA is shown in Figure 6. the drop tower with DMSA provides good drop-to-drop repeatability with an error range of $\pm 3\%$ for peak accelerations.

$$\frac{A_1}{A_0} = \sqrt{\frac{K_2}{K_1} \frac{M_1}{M_2} + \frac{K_2}{K_1}} \quad (1)$$

As discussed above, a special fixture design, first introduced by Douglas et al. [4] is employed to generate additional impacts between the test PWB and the fixture for even further amplification of accelerations. This “tertiary impact,” between the bottom of the PWB and the fixture placed on top of the DMSA drop table, is shown in Figure 7.d. To parametrically investigate the effect of clearance, a set of fixtures were designed with varying clearances between the PWB bottom and the fixture. The clearance ranged from zero clearance to infinite clearance, with various finite clearances in between (Figure 7.a-c, and Figure 4), ranging from 20% to 120% of the PWB thickness. The test specimen consists of MEMS microphone components assembled on a PWB, as shown in Figure 5. From the remainder of this paper, the term ‘secondary impact’ only refers to the impact between the PWB and the fixture.

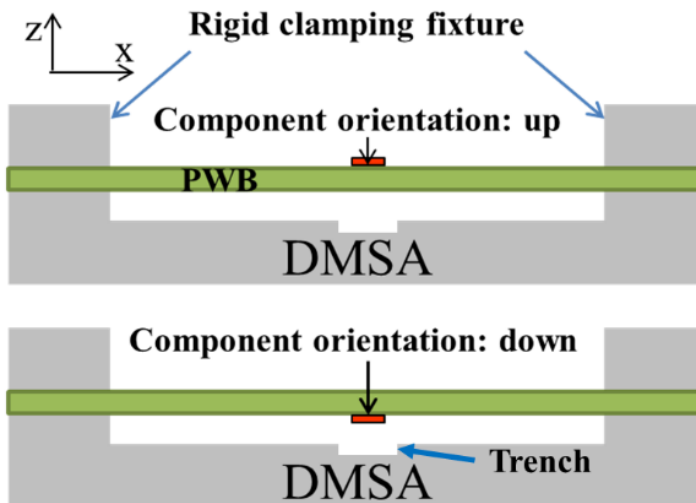


Figure 8: Drop orientations for MEMS microphone components

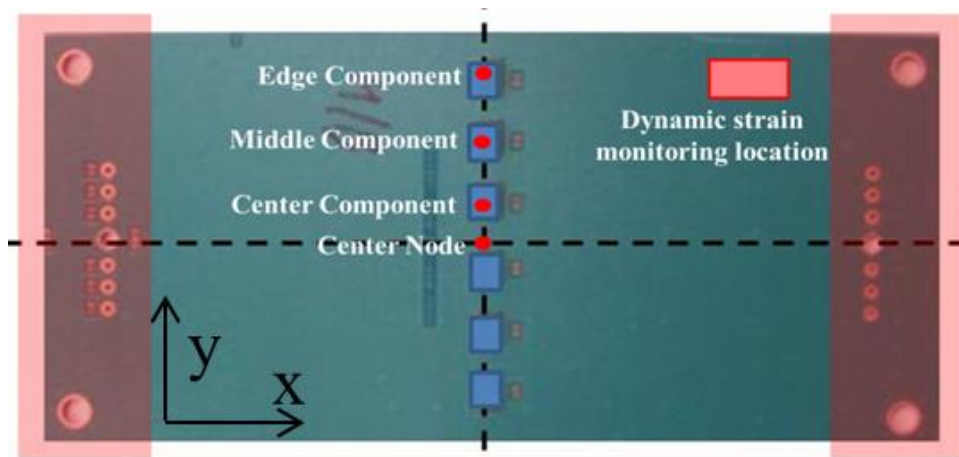


Figure 9: Test PWA with packages locations along the y axis and generic specimen design

Stress distribution in the package and interconnects also depends on the package orientation, due to the inertial force generated by the mass of the package and PWB strain at the package's footprint. To explore the effect of component mounting orientation during drop tests, PWAs are tested with the package facing two opposite directions, either upwards or downwards. As demonstrated in Figure 4, trenches are added on the top surface of the fixture, along the two orthogonal x and y centerlines containing the components being tested (Figure 7.a and c), to prevent direct impact on the MEMS components during face-down drops.

The test setup amplifies the stresses not only due to enhancement of the dynamic deformation modes of the PWB, but also by creating dynamic contact stress waves (due to secondary impact) that propagate through the test specimen. Therefore, stresses in the MEMS assemblies are amplified well beyond those experienced during typical life-cycle conditions or during traditional qualification test conditions, thus offering an opportunity for highly accelerated stress testing.

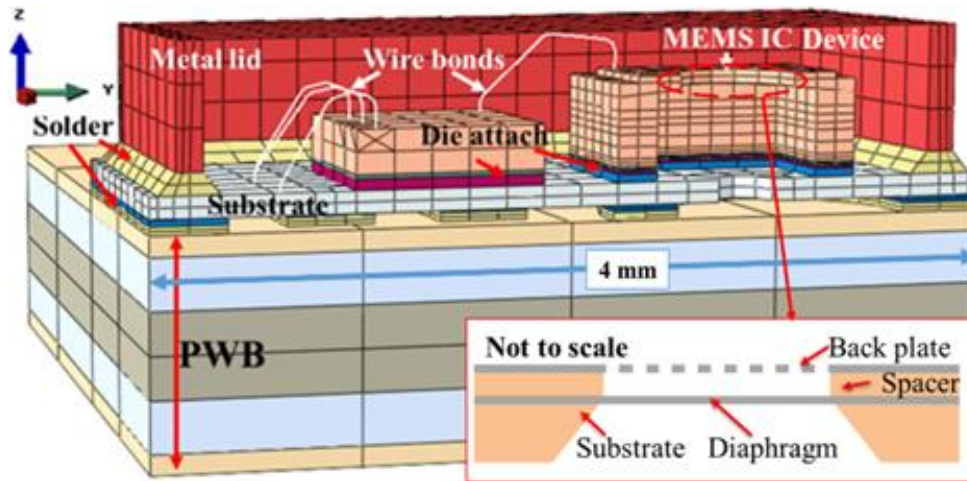


Figure 10: Cross-section of MEMS microphone

3.3.2. Test vehicle and test matrix

The test board is designed as per JEDEC standard JESD22-B111 [7]. Figure 9 shows the test board configuration, placement of the MEMS package and strain gage location for calibration of damping parameters. Unlike in JESD22-B111, in which PWAs are mounted on the fixture by four or six screws, in this work the two short edges of the PWA are completely clamped, with a 71 mm span between them. This fixture design minimizes bending of the PWB along the x-axis, so that all the MEMS components on each PWA can experience similar motion.

The test specimen contains an assembly of functional COTS MEMS microphone (Figure 10) on the PWB. All the PWBs discussed in this paper have the same thickness of 1 mm. The microphone package consists of a polysilicon MEMS microphone device, and a glob-top ASIC for signal processing, both mounted on an organic PWB substrate with die attach and interconnected together with multiple wire

bonds. The entire structure is covered with a brass lid that is soldered with SAC105 to the substrate. The multilayered substrate with copper pads in the bottom surface is soldered to matching copper pads on the PWB, using SAC105.

Table 1: Drop test matrix (number of MEMS components)

Acceleration-g, Direction	Clearance (% of PWB thickness)							
	0	20	40	60	80	100	120	∞
20,000, Down	24	24	12	18	12	18	12	18
20,000, Up	18	18	0	18	0	18	18	0

The MEMS microphone device itself, shown in Figure 10, has a poly-silicon substrate. On top of the substrate, there is a floating diaphragm and a circular back plate, separated by an annular spacer. The floating diaphragm is connected to the substrate by a cantilever-type extension, called a diaphragm runner. A corresponding structure, extended from the back plate, covers the diaphragm runner and is called the back plate runner.

The test plan, shown in Table 1, is designed to compare the effect of placement orientation of the microphone packages and the effect of secondary impacts between the PWB and the test fixture base. The total number of tested MEMS components at each drop test condition (acceleration, clearance and package facing direction) is listed in the drop test matrix presented in Table 1.

3.3.3. Testing and failure analysis

Using the fixture design shown in Figure 7, PWAs are tested at various clearances from the base fixture, with components facing either downwards or upwards. All the tests and failure analysis results in this paper are from an input acceleration profile of 20,000g magnitude and 0.05 milliseconds width. The impact pulse profile measured on the DMSA is always identical to Figure 6, with high drop-to-drop repeatability.

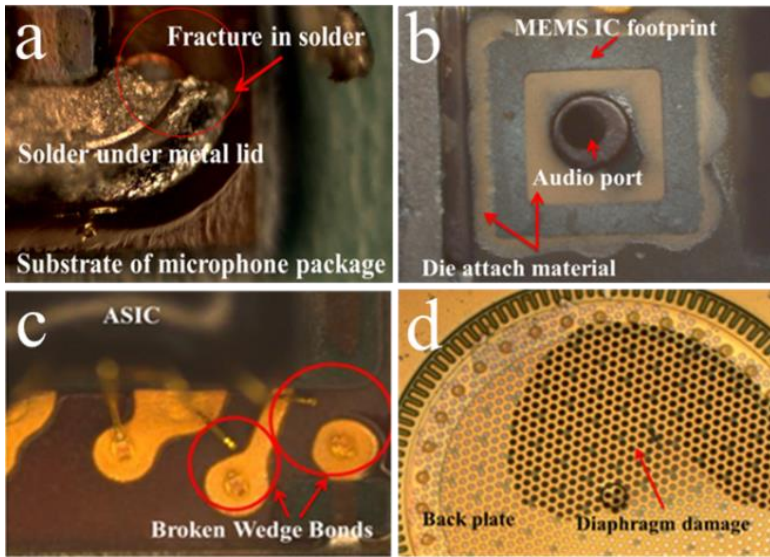


Figure 11: Common drop test failure sites in MEMS package

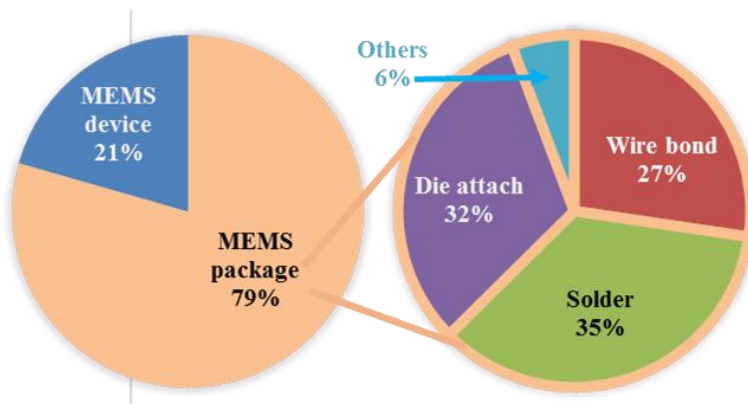


Figure 12: Percentage of failure sites, for all 20,000 g tests with component oriented downwards

Each MEMS component is functionally checked after every 25 drops. Failure analysis method consists of x-ray inspection, followed by de-lidding and microscopic inspection of the package. X-ray is used to detect wire bond failures and other internal damage modes while testing. However, the lid has to be removed to inspect the internal structures for damage. De-lidding is accomplished either mechanically or through heating & desoldering. In a prior study [6], the dominant failure sites under these highly accelerated test conditions were identified to be either in the MEMS package (wire-bond breakage/fracture, die attach delamination, fracture of the soldered package lid-seal, delamination of components soldered on PWB), or in the MEMS microphone device itself

3.4. Results and Discussion

In this section, we discuss the drop durability and the dominant failure sites of MEMS microphones assembled on PWAs at 20,000g drop tests, with and without secondary impact.

3.4.1. Drop test failure sites of MEMS components

According to the failure analysis results in [6], multiple failure sites were observed in MEMS microphone components after drop tests. Dominant failure sites can be grouped into four types, as summarized in Figure 11: a. solder fracture, b. die attach delamination (MEMS detachment from microphone package substrate) c. wire bond fracture, d. MEMS device failure. Typical MEMS device failure sites include diaphragm, back plate, diaphragm runner and back plate runner. Excessive movement of the diaphragm can fracture the diaphragm and the diaphragm runner. Additionally, being very thin and brittle, collision between the diaphragm and the back plate provides another source of failure in the MEMS device. The observed failure sites in the tested MEMS devices are in good agreement with a recent drop test study for MEMS microphone device by Li et al. [98].

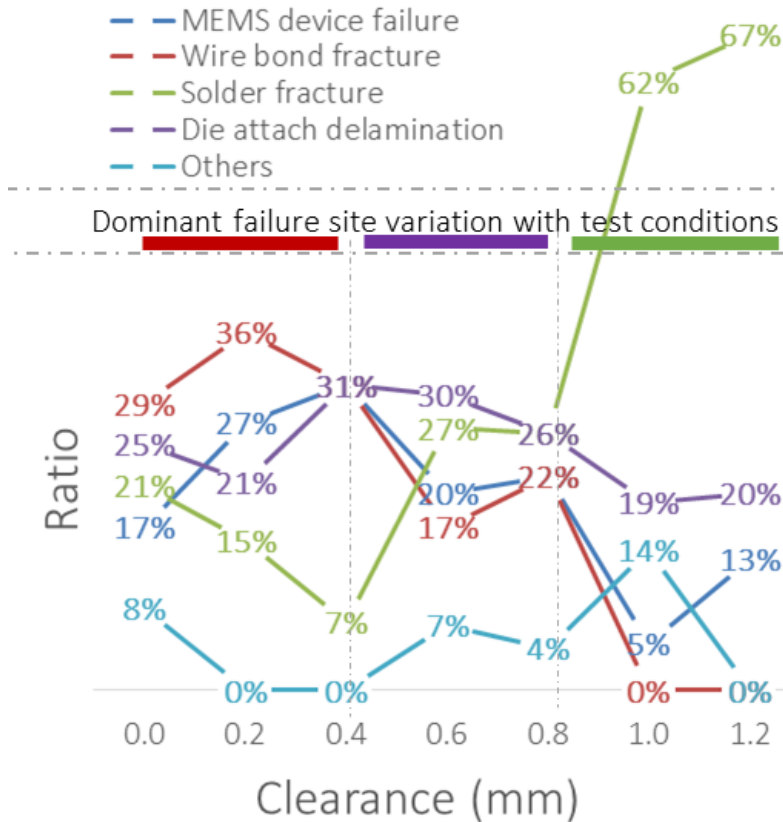


Figure 13: Failure site distribution for different clearances, components oriented down

Other than MEMS device failures, all the other three types of failure sites in Figure 11 are related to MEMS package. Wire bond fracture (Figure 11.c) is most commonly seen in the ball bond of the gold wires connecting the MEMS device and ASIC chips and in the wedge bond of the wires between ASIC chip and package substrate. Solder fracture (Figure 11.a) mainly refers to solder fracture at two locations of solder joints: one occurs between the brass lid and the substrate, the other (2nd-level) is located between the microphone module and the PWB. Figure 11.a shows the first case, where the brass lid is already detached because of solder fracture. Figure 11.b shows the top of the package substrate, with the MEMS device (IC) completely detached.

The die footprint is discernible because of the residue of the die attach material. In this case, die attach delamination occurs between the MEMS device and the substrate. Delamination of MEMS from package substrate sometimes can also induce secondary failures at other sites (i.e. fracture of the wires connecting the MEMS and ASIC chips). Such potential interactions between the detected failure sites are not further analyzed. In some MEMS components where multiple failure sites are found, all the relevant failure sites are recorded. Figure 11.b also shows an audio port located at the center of MEMS device footprint. Since the MEMS microphone is used in a non-hermetic environment, air pressure through the audio port is believed to be another source of damage in MEMS structure during the secondary impact. Further investigation regarding the effect of air pressure were reported by Li et al. [98].

Table 2: Dominant failure site of MEMS microphone component at each drop test condition

		Clearance (% of PWB thickness)		
		0-40	40-80	80-120
Component orientation	Down	Wire bond	Die attach	Solder
	Up	Wire bond		

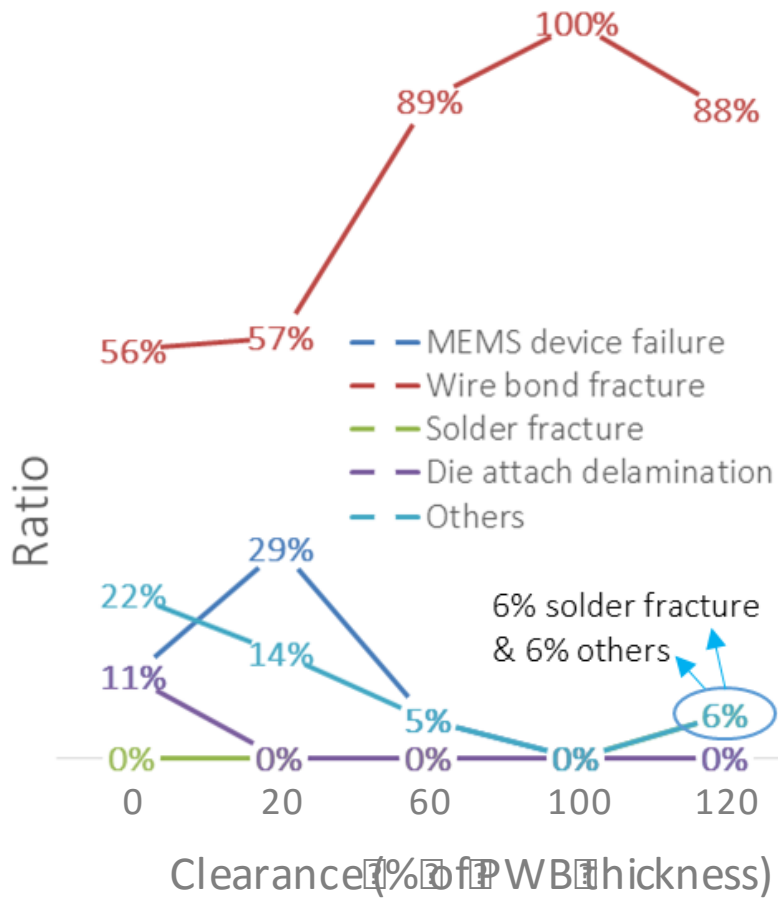


Figure 14: Failure site distribution for different clearances, components oriented up

As Tilmans et al. [82] pointed out, failures in MEMS packages are as important as failures in the MEMS device, in hampering the expected performance and reliability of MEMS. A quantitative comparison between MEMS device failures versus MEMS package related failures is presented first in Figure 12, based on the results from downwards oriented MEMS components. The result shows that only less than a quarter of functional failures in MEMS microphone were caused by MEMS device failures (Figure 11.d), all the rest are due to damage in the MEMS package.

The percentage of each failure site varies with clearance and component orientation (facing upwards or downwards). Either orientation may lead to failure site distributions that are different from the distribution in Figure 12. In order to investigate the variation in failure site distribution as a function of clearance and component orientation, the percentage of each failure site is further analyzed at each clearance level, as shown in Figure 13 and Figure 14.

Figure 13 shows the detailed percentage of failure site distribution at each clearance, when components are oriented downwards. In general, each failure site is found to have a non-monotonic dependence on the clearance amount. For example, the percentage of damage in MEMS device is highest at 40% and lowest at 100% of PWB thickness, whereas a totally opposite trend is observed for solder fractures. Noticeably, in all the test conditions, there is always at least one MEMS package failure site more likely to occur than failures of the MEMS device.

Figure 14 presents the distribution of failure sites at all clearances, with components facing upwards. Different from Figure 13, wire bond fracture in Figure 14 stands out as the only dominant failure site, independent of clearances.

Based on the analyses in Figure 13 and Figure 14, the phenomenon of failure site transition is summarized in Table 2. When MEMS components are oriented upwards, wire bond failure occurs most frequently; when MEMS components are facing downwards, the dominant failure site is observed to transition from wire bond fracture at clearances 0-40% of PWB thickness h , to die attach delamination at 40-80% h and to solder fracture at 80-120% h .

In conventional board level drop tests without secondary impacts, acceleration-strain correlations are generally monotonic. By contrast, drop test with secondary impact is more complex. The finite clearance not only generates an additional amplification in acceleration, but also invokes participation of multiple PWA flexural modes [4]. Such multi-mode interaction makes understanding the variations of acceleration and strain at each failure site very challenging. Moreover, failure sites with different natural frequencies may show different sensitivities to all the dynamic inputs above. In order to explain the observations in Table 2, Part II of this study focuses on the dependence of damage on local dynamic mechanical response at each failure site.

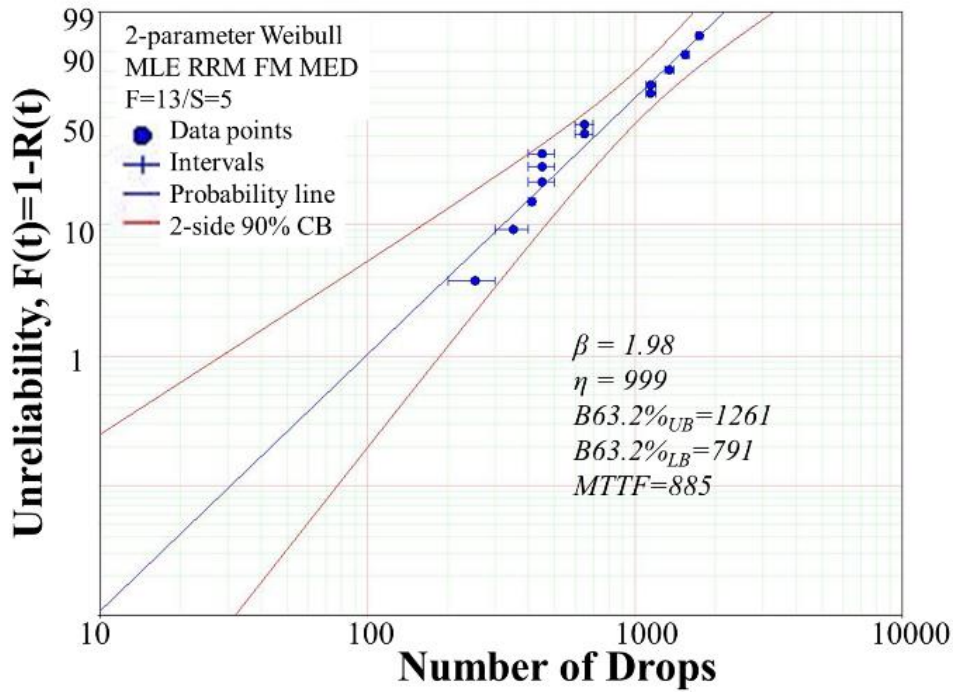


Figure 15: Unreliability vs. Time (cycles to failure) plot of tests at 20% clearance, package facing upwards

3.4.2. Characteristic life for MEMS component and each failure mode

Secondary impact drop test results for MEMS assemblies at 20,000g were partially reported earlier ([6] [5]). However, since tests were conducted at limited number of conditions and replicates, only qualitative conclusions were provided. In addition, the maximum drop count was limited to 500, when no failures were detected in some cases. Survival data were discarded in [6] and the failure distributions were based only on the data from samples that failed within 500 drops. Even though this averaging method was capable of qualitatively showing the trend of drop test durability of MEMS components as a function of clearance, the actual estimated lifetimes were unavoidably underestimated. For the same reason, two test conditions (components facing up with 20% of clearance, and components facing down with no secondary impacts) provided no failure data because all survived 500 drops.

Test results in this study improved upon all the issues listed above: 1). New tests were conducted up to 2000 drops when needed. 2). Numbers of test conditions and replicates at each condition are both increased significantly. 3). The expected drop counts to failure at each test condition was estimated based on both failure data and censored data. 4). Enabled by additional replicates, lifetimes are estimated separately for each identified failure site. These improvements provide quantitative insights into the overall reliability of MEMS microphone components in severe drop tests with secondary impacts. Moreover, the failure site in MEMS microphone components is observed to vary as a function of the clearance magnitude.

Experimentally measured durability data (Weibull characteristic life) are plotted for each test condition (clearance and component orientation). The Weibull distribution is found to do a better job of describing the failure statistics than the exponential

distribution, normal distribution, and lognormal distribution. Thus the Weibull distribution is adopted for characteristic life calculations in this study. The probability density function (pdf) of the 2-parameter Weibull distribution is defined as in Equation 2 [99]:

$$f(t) = \left(\frac{\beta}{\eta}\right) \left(\frac{t}{\eta}\right)^{\beta-1} \exp\left[-\left(\frac{t}{\eta}\right)^\beta\right] \quad (2)$$

where η is characteristic life and β is shape parameter. A sample plot for 20%h clearance test, with packages facing upwards, is plotted using Reliasoft Weibull++, as shown in Figure 15. The blue line is the Weibull probability plot, whereas the two red curves are the upper and lower bounds of two-side 90% confidence interval. Because some censored data were used for calculation, maximum likelihood (MLE) is selected as the parameter estimation method. In this example, based on the failure data obtained from 18 samples (including 5 censored data, (shown in Figure 11) the shape parameter β is equal to 2.0, characteristic life is 999. With a 90% confidence interval, upper bond reaches 1261 and lower bond is at 791. MTTF (mean-time-to failure) is equal to 885.

Figure 16 summarizes the Weibull analysis results at all the test conditions. For demonstration purpose, 2-sided 90% confidence bounds are added to the two drop orientations at 20%h clearance. It is clear that the finite clearance drop tests are significantly more severe than in infinite clearance cases. Furthermore, drop durability of PWAs tested with components facing upwards is higher than with those components facing downwards. According to Figure 16, the durability of MEMS

microphone decreases as the finite clearance between the PWA and the fixture increases. This is true for components oriented both downwards and upwards.

The Weibull characteristic life is estimated for failures at each observed failure site. Failure mode is identified for each detected failure by conducting immediate failure analysis, characteristic life of each failure site can be plotted based on all the available data for the given failure site. Figure 17 lists the durability at each failure site and clearance with components facing downwards. Multiple failure sites are observed at some test conditions (as shown in Figure 13). Therefore, characteristic life values shown in Figure 17 are expected to have larger scatter than in Figure 16. As a result, when too few failure data are available for life estimation, data point will be missing (for example, MEMS device failures with large clearances).

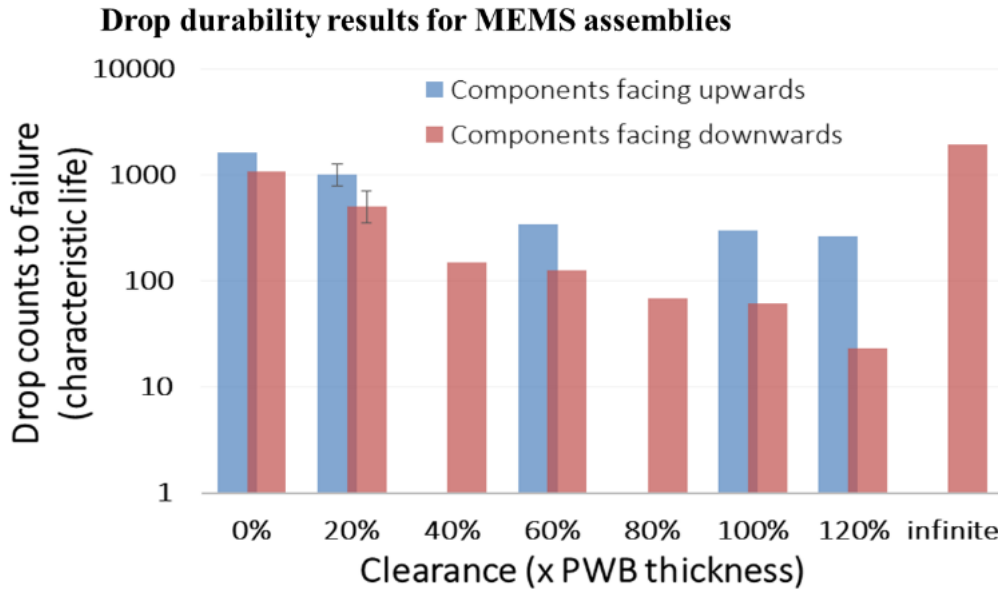


Figure 16: Drop durability results for MEMS assemblies

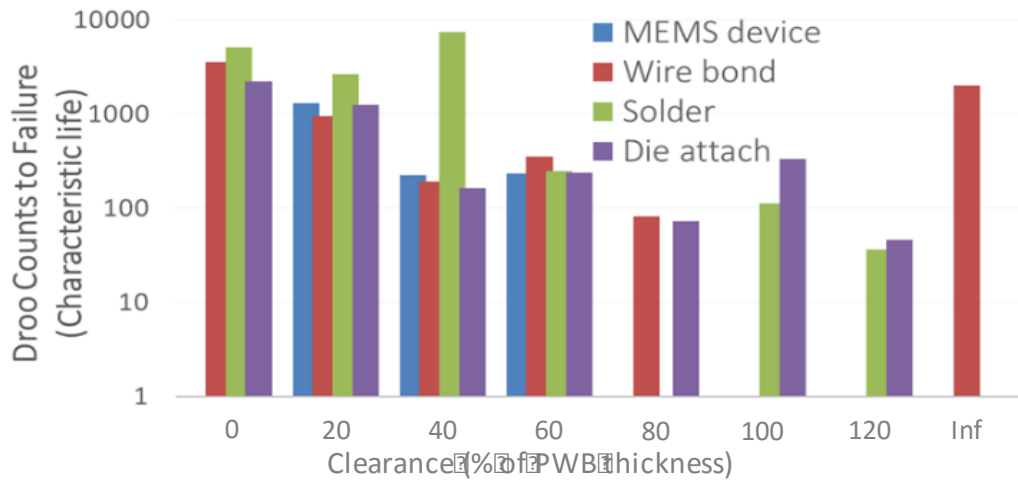


Figure 17: Drop durability results by failure sites, packages facing downwards

Ideally, the failure site with the lowest characteristic life at each clearance is supposed to be the most vulnerable (dominant) failure site. Following this pattern, small discrepancies (i.e. at 0 and 60% of PWB thickness) can be found between the results in Figure 17 and Table 2. Such discrepancies reflect the qualitative and probabilistic nature of the effect of failure site transition, which can be further improved with additional test results. Overall, the results shown in Figure 17 are compatible with the information in Table 2, when taken in the context of the sources of variabilities discussed earlier.

3.5. Conclusions

In this highly accelerated drop test study, secondary impact between test board and fixture is found to significantly amplify the impact, even with a fully supported, tightly clamped PWA, as indicated by the drop durability results of the MEMS microphone. The durability of MEMS microphone decreases as the clearance between the PWA and the fixture increases. At any given clearance, the drop durability of PWAs tested with components facing upwards is higher than that of PWAs with components facing downwards. This indicates that the inertial force due to component weight plays a significant role in failures.

The majority of functional failures in the tested MEMS microphone components are caused by failure sites in the MEMS package, including wire bond fracture, solder fracture and die attach delamination. Less than a quarter of all failures are due to MEMS device failures. Furthermore, the failure site is observed to change, with changes in clearances for secondary impacts. Participation of multiple bending modes could contribute to the rapid change in the dominant failure site.

Using suitable statistical distribution functions, the characteristic life is estimated for each failure site. The calculated characteristic life data for each failure site provide additional qualitative verification of the failure site transition.

Acknowledgement

We would like to thank the Microsoft Mobile Oy (Finland) and the Lansmont Corporation for their assistance in all our drop testing and research. We wish to acknowledge the members of Center for Advanced Life Cycle Engineering (CALCE) at the University of Maryland for sponsoring this study.

Chapter 4. MEMS Packaging Reliability in Board Level

Drop Tests under Severe Shock and Impact Loading

Conditions Part II: Fatigue Damage Modeling

In this chapter, a proposed mechanistic damage model for repetitive drop testing is presented, based on the von-Mises' strain, and hydrostatic stress at each failure mode. Model constants are obtained from test data for each failure mode. The FEA model is calibrated using dynamic strain readings from PWB. The FEA model is used for both the identification of critical failure sites and the computation of stress and strain histories used for damage modeling. Some preliminary test results in this chapter was published as a conference proceeding in the EuroSimE 2012 Conference. The current draft of this chapter is submitted to Transactions on Components, Packaging and Manufacturing Technology for peer-review.

4.1. Abstract

Damage in handheld electronic devices due to accidental drops is a critical reliability concern. This paper is the second of a two-part series and focuses on damage models for drop test durability of commercial off-the-shelf (COTS) Micro-Electro-Mechanical Systems (MEMS) components that are mounted on Printed Wiring Boards (PWBs). The modeling approach is based on experimental results presented in the first part of this two-part series. In particular, the focus of this paper is on damage due to drop events under extremely high accelerations (20,000g, "g" is the

gravitational acceleration) achieved by a series of secondary impacts. Impacts with such high accelerations can occur in handheld electronic devices due to collisions between internal neighboring structures and can generate stress levels well beyond levels previously anticipated in typical use, or in conventional qualification tests. A calibrated dynamic multiscale finite element model is used to evaluate the stresses at the relevant failure sites. Utilizing the local stress at each failure site, a fatigue damage modeling approach is proposed to predict the interaction of the competing failure mechanisms in MEMS components. The proposed damage model is based on the deviatoric stress (or strain) at the failure site and uses a hydrostatic stress correction factor to address the influence of mean stress (depending on component orientation). The model estimates the damage accumulation rate for a given stress condition and integrates the accumulated damage over the entire response history. This approach makes it possible to address the influence of post-impact transient response on fatigue damage accumulation. The damage-model constants are determined for each failure site of interest, by relating the failure data to the corresponding stress/strain metrics. Damage modeling results are not only capable of matching the lifetimes of MEMS components in drop testing, but also provides an explanation of transitions in dominant failure sites observed in MEMS assemblies under different drop conditions.

Index Terms— Drop test, damage modeling, fatigue model, secondary impact, input-g, ultra-high accelerations, multi-scale FE modeling

4.2. Introduction

This is the second part of a two-part paper that addresses the role of ‘secondary impacts’ on the drop-durability of MEMS assemblies. In Part I, experimental results from an extensive drop testing program were presented. Drop tests were conducted under a highly accelerated condition of 20,000g (“g” is the gravitational acceleration). Secondary impact between test board and fixture is found to significantly amplify the impact, even with a fully supported, tightly clamped PWA. From drop testing with secondary impacts, multiple failure sites in MEMS components are identified: from packaging to MEMS device. The participation of competing failure sites is also demonstrated via characteristic life representations of each failure site at various clearances. The present paper is Part II, proposes a damage modeling approach to describe the experimental findings in Part I.

The dynamic response of moving parts [15], [16] to impact and drop can cause reliability challenges in MEMS technologies [75]. Mariani et al. [77] investigated stress concentrations and fractures in brittle materials used in MEMS devices by conducting a detailed multi-scale simulation. The investigation includes MEMS packaging-level drop test, and crack propagation analysis of polycrystalline microstructures. Bomidi et al. [78] studied fatigue damage and variability of polycrystalline metals used in MEMS devices, by simulating crack initiation, propagation and coalescence in bending fatigue tests based on continuum damage mechanics. The dominant failure mechanism in MEMS components is structure-specific and also depends on the loading conditions [79]. According to Srikar and

Senturia [16], MEMS packaging can alleviate the severity of the shock pulse, therefore the substrate was assumed to be a rigid body to model the worst-case scenario. In contrast, Alsaleem et al. [81] pointed out that the presence of second level (PWB-level) packaging for MEMS devices may further amplify the dynamic response of the microstructure. Ghisi et al. [80] conducted drop testing and simulation for an off-the-shelf MEMS accelerometer and investigated the effect of packaging on the reliability of MEMS devices. The study showed that MEMS packaging did not reduce the MEMS device failure rate, although failures in the MEMS packaging occurred more frequently than failures in the MEMS device.

According to prior experimental studies by the authors [6], failure mechanisms of the MEMS components include device-related failures such as silicon fracture, stiction between moving parts and contamination, as well as packaging-related failures such as solder interconnection fracture, wire bond yielding and fracture, and die attach delamination. MEMS device failures were experimentally found to contribute less than 25% of all the functional failures of the MEMS microphone assemblies when subjected to secondary impacts during drop events. As discussed in Part I, the severity of the ‘secondary impacts’ was controlled by parametrically varying the clearance between the test PWB and the test fixture. Both the durability and the severity-ranking of the dominant failure sites are found to vary as a function of the clearance between the PWB and the fixture. Therefore, quantitative fatigue life estimation for each failure site/mode is needed, to accurately capture the observed failure site transition for different test conditions.

To assess the drop durability of surface mount technology (SMT) components, researchers have used both empirical and analytical approaches. Due to the intensity of computational expenses, dynamic fracture mechanics based approach is generally not preferred in practice for generating drop-durability curves from repetitive drop conditions. On the other hand, empirical “Damage boundary” method [51] mapped entirely based on experimental data is also not preferred because of its empirical approach and design-specific nature. By contrast, FEA-based methods can significantly improve the prediction capability and efficiency because they use local dynamic response at the failure site to assess the damage severity. For example, FEA-based life modeling approach has been conveniently applied before to compare the influence of different drop test parameters, such as boundary condition [54], drop height [55] and drop orientation [2].

The focus of this Part II is on drop test durability modeling of commercial off-the-shelf (COTS) Micro-Electro-Mechanical Systems (MEMS) components that are mounted on PWBs. Based on the experimental results in the first part, a fatigue damage model is proposed and applied to each failure site/mode observed in MEMS microphones. The model considers the effect of both hydrostatic and equivalent deviatoric (von Mises’) stresses. The layout of this paper is as follows: first, a fatigue damage modeling method is proposed for each competing failure site/mode in MEMS assemblies. Then the test procedure and the simulation framework are introduced as inputs to obtain the fatigue model constants. Because of the structural complexity in PWA with MEMS components, a hierarchical dynamic multi-scale FEA stress modeling technique is employed to demonstrate the effect of drop and impact on local

dynamic response in a complex miniature structure. Then, the damage model constants are derived for each failure site by correlating the stress analysis results with selected experimental results. The model constants are then verified by comparing the predictions with the remaining test results.

4.3. Modeling and Testing Methods

In this section, a fatigue damage model is first proposed for repetitive drop loading with secondary impacts. Then a multi-scale global-local FEA modeling approach is introduced, for estimating the stress response during drop events with secondary impacts. The stress history and the experimental results from Part I are both jointly used for evaluating the model constants for the proposed fatigue damage models in this study.

4.3.1. Damage Models for Repetitive Drop Loading with Secondary Impacts

Various types of fatigue models based on local material response have been developed in the past few decades to evaluate the cyclic damage accumulated from repetitive loading. Typical fatigue models used in electronic packaging field can be classified into two broad categories: models based on mechanics variables (stress or strain) [59], [60] and models based on thermodynamic variables (energy or entropy) [61], [62], [100]. Elastic-plastic stress/strain histories at the failure site are often used for fatigue models in high strain-rate (drop, impact and vibration) analysis [63] [12] [64]. Examples of classical fatigue models include the generalized Coffin-Manson's (total strain) fatigue model [65] [66], [67], [61].

In the event of multiaxial deformation fields at the failure site, typical damage metrics can be: equivalent (von Mises') or principal shear stress (or corresponding total strain or plastic strain values, or distortional inelastic work density) for ductile materials [59], [60]; principal normal stress (or strain) for brittle materials; peeling or shear interfacial stresses for interfacial delamination.

Some multiaxial situations may require more sophisticated approaches that combine both the equivalent stress (which is related to the octahedral shear stress at the failure site) with the local hydrostatic stress, since the equivalent stress metric cannot distinguish between a tensile loading condition and a compressive loading condition. This combined-stress approach allows us to account for the fact that fatigue damage accumulation can be inhibited by compressive hydrostatic stress and facilitated by tensile hydrostatic stress [62], [68]. Bridgman [68] and McClintock et al. [69] showed a profound effect of hydrostatic stress on the shear strength of most commonly used metals. Morrow et al [62] experimentally proved that a compressive mean stress enhances the fatigue life while a tensile mean stress shows the opposite. Brownrigg. et al, [70] explained that compressive hydrostatic stress severely retards the nucleation and growth of voids near carbide particles in a metallography study of spherodized 1045 steel. The effect of hydrostatic stress is also evidenced in board level drop tests. For example, in JEDEC22-B1111 standard drop tests, components mounted on top of the PWAs would usually induce less damage than components mounted on the bottom [5], [63], even though similar strain amplitudes are expected at the footprints of solder joints. This difference comes from the fact that the hydrostatic stresses are different due to inertial forces from the component mass.

To implement the observed hydrostatic stress effect on the damage accumulation rate in materials, Socie and Morrow [71] added a mean hydrostatic stress correction factor σ_m to the high cycle fatigue term of the generalized Coffin-Manson fatigue model. Manson and Halford [72] argued that the mean stress effect should be considered in low-cycle fatigue as well. Varvani [73] introduced a tensile mean stress correction

multiplier to address the additional fatigue damage in silicon due to the mean normal stress applied to the critical plane of a silicon crystal. This correction is often written as $(1 + \sigma_n^m / \sigma_f')$, where σ_n^m denotes the hydrostatic stress. σ_f' stands for a reference stress value termed axial fatigue strength coefficient. Similar approaches have been used by many researchers, including in electronics systems [101], [102].

The fatigue modeling approaches discussed above generally work well when the cyclic loading has a constant amplitude. In the event of variable amplitude loading, some researchers use cycle counting techniques to break up the entire history into a set of bins of constant-amplitude loading and a suitable damage superposition technique to add up the damage from each bin. Alternatively, we can use an integral approach to treat each cycle individually. In the present case, each drop event results in a damped transient response that decays and disappears after a few cycles. To account for damage accumulated during such multiple consecutive cycles after an impact event, Varghese and Dasgupta [12] proposed a fatigue life model where PWA reversals at different natural frequencies during and after impacts are considered. The accumulated damage was obtained by summing the damage for the dominant dynamic response modes. A similar approach was used by Lall, et al. [64] for estimating fatigue life of solder joints of BGA in JEDEC22-B111 standard drop tests.

Based on the above considerations for drop and impact loading, a unified fatigue model is proposed to predict the fatigue durability at competing failure sites in MEMS packages. We define an incremental damage model:

$$D_i = A \int_{t=0}^{t=T} \left(1 + \frac{\sigma_m(t)}{\sigma_m'} \right) \left(\frac{\varepsilon_{eq}(t)}{\Delta\varepsilon_{eq}'} \right)^B dt \quad (3)$$

where D_i ($0 < D_i < 1$), is the normalized incremental scalar damage index of a single drop event at each critical failure site. The subscript i denotes each failure site. The index is normalized so that its cumulative value reaches 1 when the material at the i^{th} failure site completely loses its functional capability and is regarded to have failed. Transient histories of two damage metrics are included in this model: von Mises' equivalent strain history $\varepsilon_{eq}(t)$ and hydrostatic stress history $\sigma_m(t)$. Two selected material coefficients are utilized as reference scalar model constants: $\Delta\varepsilon_{eq}'$ is the cyclic fatigue ductility coefficient and σ_m' is the pressure correction coefficient. Correlation constant A and power exponent B are both model constants for each failure mechanism. The hydrostatic stress correction multiplier is added to the equivalent strain portion, emphasizing that an equivalent shear strain will cause more fatigue damage with hydrostatic tension than with hydrostatic compression. In an extreme case when $\sigma_m(t) = -\sigma_m'$, no instantaneous damage would be accumulated if the hydrostatic pressure is significantly large. Damage accumulated during each incremental dt is integrated from time 0 to t_i , where t_i stands for the total duration of significant dynamic response.

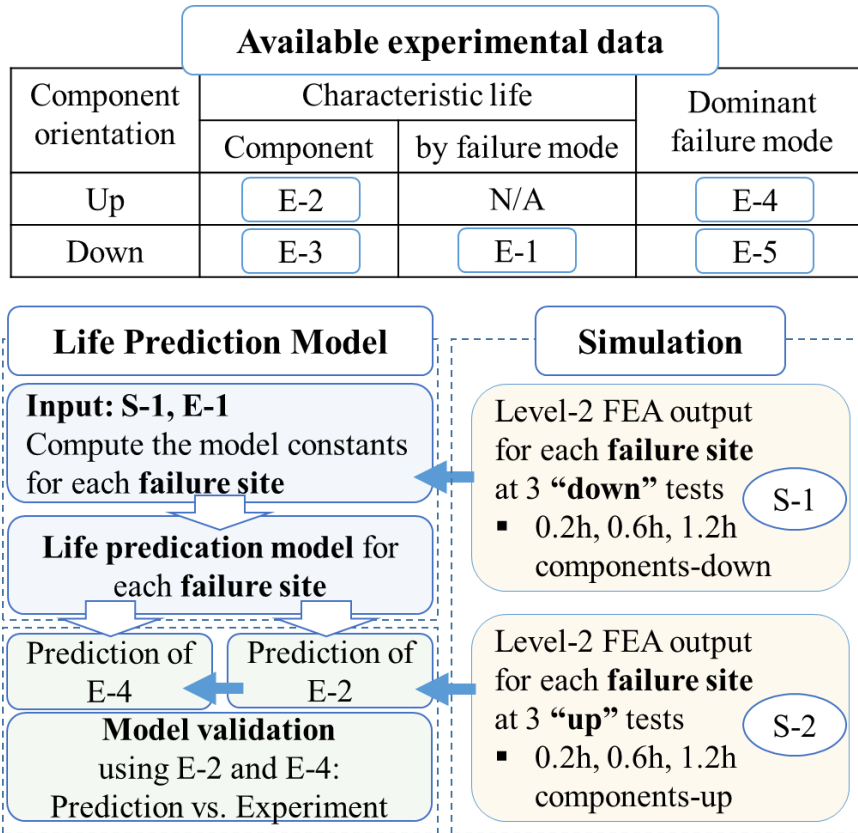


Figure 18: Flow chart of computation and validation for fatigue damage models (S-*i*: simulation; E-*i*: experimental analysis)

The procedure of obtaining the model constants for each failure site is illustrated in Figure 18. As discussed in Part I of this two-part series (and further explained below in Section 2.2 of the present paper), the severity of secondary impact is varied by introducing various clearances between the bottom of the test PWB and the top of the fixture base. So three clearances (0.2h, 0.6h and 1.2h) are considered in this paper (where h is the thickness of the PWB). First, experimentally obtained characteristic life data is segregated by different failure mechanisms from each secondary impact condition (results are presented in Part I of this two-part series). Test vehicles with components facing downwards (experiment and simulation) are used to extract the

model constants for each relevant failure site. Subsequently these model constants are validated by simulating the cases with components facing “up” and comparing the predicted durability with experimentally measured values (E-2 defined in Figure 18). The predictive capability of the proposed damage model is assessed from two perspectives: a. quantitative comparison of durability results of MEMS components (E-2), b. qualitative ranking of the dominant failure site (E-4).

For completeness, Section 4.3.2 summarizes the experimental description presented earlier in Part I.

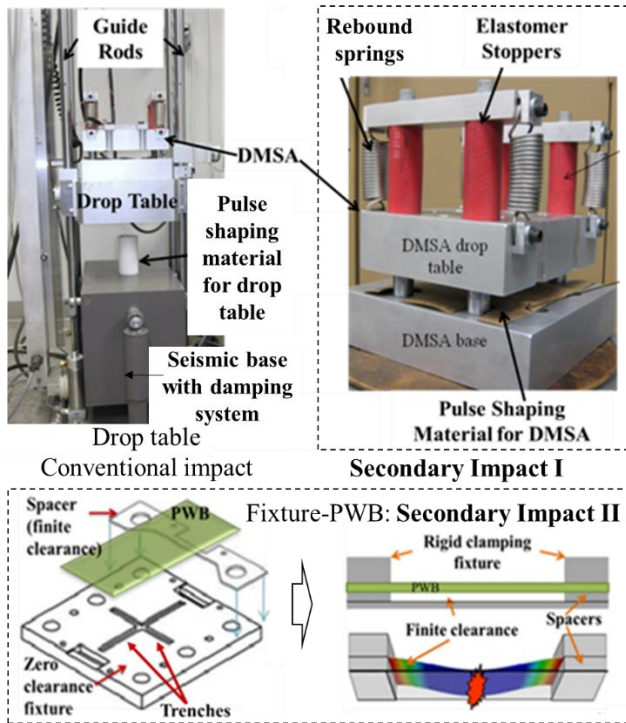


Figure 19: Acceleration amplifications setup based on secondary impacts

4.3.2. Secondary impact test setup and test matrix

As described in Part I of this two-part paper, a high acceleration test setup is developed based on the principle of multiple secondary impacts: first in the drop test setup using a commercial DMSA (dual mass shock amplifier) another intentional contact between the PWA and the base of the fixture by introducing a finite clearance between them. In total, three consecutive impacts (one primary impact and two secondary impacts) are used to magnify the acceleration levels in board-level drop test.

Table 3: Drop test matrix (number of MEMS components)

Acceleration (G), Direction	Clearance (h, thickness of PWB)							
	0.0	0.2	0.4	0.6	0.8	1.0	1.2	∞
20,000, Down	24	24	12	18	12	18	12	18
20,000, Up	18	18	0	18	0	18	18	0

Table 3 shows the drop tester which consists of a drop table, seismic base, and pulse shaping materials (termed programmer materials). The primary impact at the drop table is capable of reaching repeatable impact accelerations up to 5,000g. The first of the two secondary impacts is produced by the impact between the DMSA drop table and the DMSA base (which is rigidly mounted on the tower drop table), and amplifies the drop table acceleration by over an order of magnitude, to provide extremely high accelerations up to 100,000g. Pulse shaping materials are used to tailor the magnitude and duration of the acceleration profiles. The drop tower with DMSA provides good drop-to-drop repeatability with an error range of $\pm 3\%$ for peak accelerations.

The two short edges of the test PWA were rigidly clamped in a fixture which was rigidly mounted on the DMSA drop table. The second secondary impact, occurs between the bottom surface of the PWA and the top surface of the fixture. This is achieved by introducing finite clearance of various magnitudes between the PWA and the fixture, using spacers of various thickness ($0.1h$ and $0.2h$, where h is the PWB thickness). Two limiting cases were also added as benchmarks: one with zero clearance (no spacer) and one with no secondary impact (by removing the fixture base plate so the PWA was free to vibrate without any impacts. This case has been termed the infinite clearance case. The PWAs were tested with components facing either upwards or downwards, to explore the effect of drop orientation. The test matrix is presented in Table 3: numbers of tested MEMS components at each test condition (acceleration, clearance and package facing direction) are listed.

4.3.3. Test specimen and multiscale finite element drop simulation

In [103], the drop test simulation framework utilized in this paper were initially introduced, and sample dynamic strain outputs at the critical failure sites of MEMS components were presented. For completeness, the contents discussed in [103] are briefly summarized in this section.

Accelerated board-level drop tests are conducted to quantify the drop durability of MEMS microphone components. The test specimen is a PWA consisting of COTS SMT MEMS microphone components mounted on a 1 mm thick laminated FR-4 PWB. The small dimensions of the features in the MEMS component limit the ability to deploy sensors to physically measure the local mechanical response at the site of

the secondary impact and at potential failure sites within the MEMS components. As a result, it is important to use calibrated FEA models to estimate the response histories, based on sensor measurements at the nearest convenient locations. Due to the structural complexity of the MEMS component assembled on the PWB, a multi-scale global-local FEA modeling method is adopted. The overall global model (termed Level 1 model here) is used to capture the dynamic response of the overall PWA under the drop and secondary impact events. The local model (termed Level 2 model) is a detailed FEA representation of the structural details of the MEMS microphone component and includes only the portion of the PWB that is directly under the footprint of the microphone component. The boundary history for the Level 2 model is imported from the Level 1 model, at the footprint of the MEMS microphone on the PWB. Dynamic stress and strain histories at the critical failure sites in the MEMS package are monitored in the Level 2 model for further damage analysis. Since the failure sites of interest in this paper are in the MEMS package rather than within the MEMS device itself, failures of the elements within the MEMS device are not discussed further.

Figure 20 shows the PWB configuration, MEMS component placement and strain gage location. The geometry of the 1 mm-thick PWB design follows JESD22-B111 [7]. Six MEMS components are mounted on one side of each PWB along the short centerline. Dynamic strain signals, collected using strain gage while drop testing, are used for FEA model calibration. The specimen mounting conditions used in this study are different from the mounting recommended in JESD22-B111. In this study, the two short edges of PWA are rigidly clamped in the fixture, with a 71 mm unsupported

span between them. This fixture design minimizes bending of the PWB along the x-axis, so that all the MEMS components on each PWA can experience similar deformation. To be consistent, fatigue damage computations in this study are all based on simulation outputs from the edge component (Figure 20).

The Level 1 (global) model uses a simplified FEA representation for computational efficiency. The PWB is modeled with shear-deformable, orthotropic, 15-ply shell elements and the fixture is represented with a rigid body. The acceleration history recorded on the DMSA drop table during drop experiments is imposed as an “input-g” [20] boundary condition for the Level 1 FEA model. By using the dynamic explicit iteration method in FEA, local acceleration and flexural strain histories at the footprints of MEMS components are obtained from the Level 1 model.

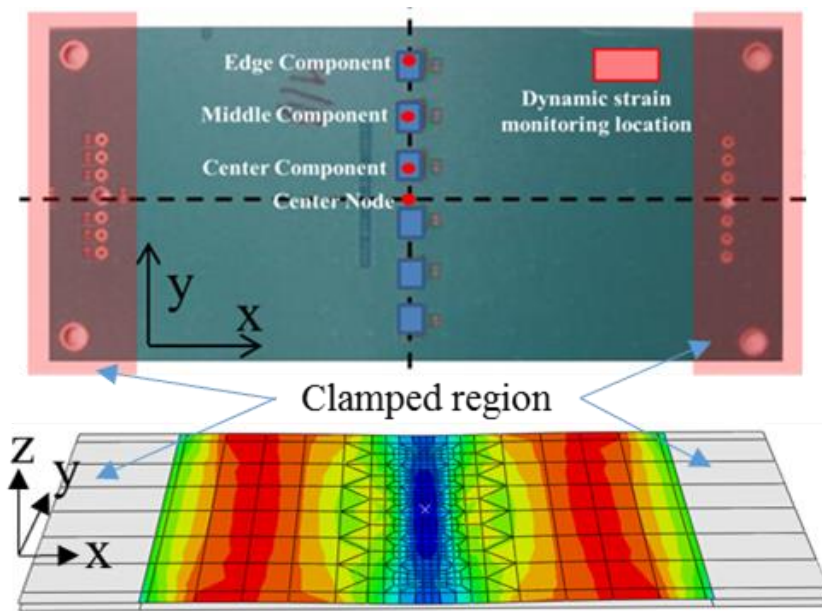


Figure 20: Test PWA with 6 packages located along the y axis of the PWB (Level 1 FEA model is also shown in the figure)

Figure 21 shows the Level 2 model built for the MEMS microphone component, consisting of a polysilicon MEMS microphone IC device, and a glob-top ASIC for signal processing, both mounted on an organic PWB substrate with die attach and interconnected together with multiple wire bonds. The entire structure is covered with a brass lid that is soldered to the substrate with SAC105 solder. The substrate has copper pads on the bottom surface, which are used to solder the component to matching copper pads on the PWB using SAC105 solder. Unlike in the Level 1 model, the multi-layered PWB and most of the other structures in Level 2 model use 3D solid brick elements, to better capture the PWB deformation along the z-axis. The only exceptions are the bond wires which are modeled with 3D beam elements. The deflection history applied to the PWB in the Level 2 model is captured from the Level 1 global model. For computational expedience, only half of the component is simulated, with a symmetric boundary condition applied on the y-z plane of symmetry.

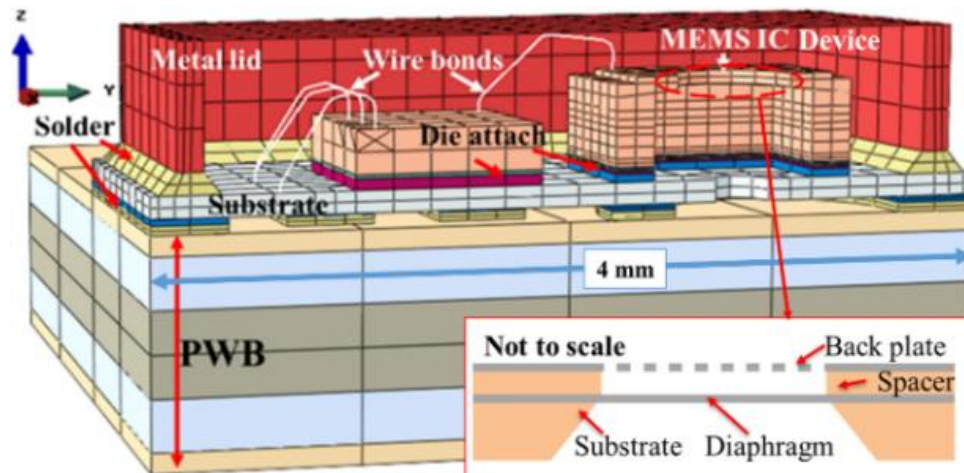


Figure 21: Cross-section of MEMS microphone (Level 2 local model)

Relevant material properties for Level 1 and Level 2 models are summarized in Table 4. Properties of ten materials are featured by four categories: isotropic elastic (“Elastic-i”), orthotropic elastic (“Elastic-o”), plastic with isotropic hardening (“Plastic-i”) and strain-rate dependent (“Rate”). For example, solder is modeled as a strain-rate dependent, elastic-plastic material, therefore it is labeled by “Y” under three columns: “Elastic-i”, “Plastic-i”, and “Rate”. Further details of the material properties are presented in Appendix-a.

Table 4: Summary of relevant material properties

Materials	Elastic-i	Elastic-o	Plastic-i	Rate
Solder	Y		Y	Y
Au	Y		Y	
Brass	Y			
Copper	Y			
Die attach	Y			
Silicon	Y			
Solder mask	Y			
RCF –PWB	Y			
Conduct-PWB		Y		
FR-4		Y		

4.4. *Results and Discussions*

In this section, results of drop test simulation and fatigue damage modeling are discussed.

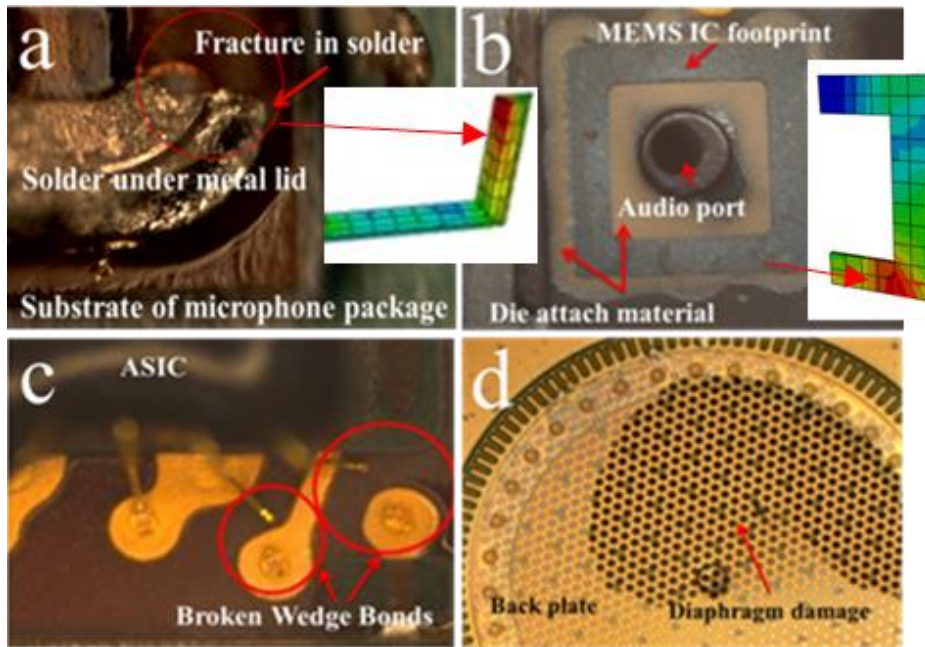


Figure 22: Common drop test failure sites in MEMS package

4.4.1. Failure modes and durability of MEMS components

The dominant failure sites in the MEMS components analyzed in this study under secondary impact drop test conditions are summarized in Figure 11. The critical failure sites in the MEMS package are identified from the Level 2 model (high stress concentration is marked in red).

As reported in Part I of this two-part series, only less than a quarter of functional failures during drop testing of the MEMS microphone components are in the MEMS

device. Part I also reported that the dominant failure site varies with drop conditions, as summarized in Table 2. For example, when the PWA is oriented with the MEMS components facing upwards, wire bond failure occurs most frequently. Conversely, when the MEMS components are facing down towards the bottom fixture, the dominant failure site is observed to change to the die attach and the solder joints.

Table 5: Dominant Failure Sites in MEMS microphone component at each drop test condition

Clearance (mm)		0.0-0.4	0.4-0.8	0.8-1.2
Component orientation	Down	Wire bond	Die attach	Solder
	Up	Wire bond		

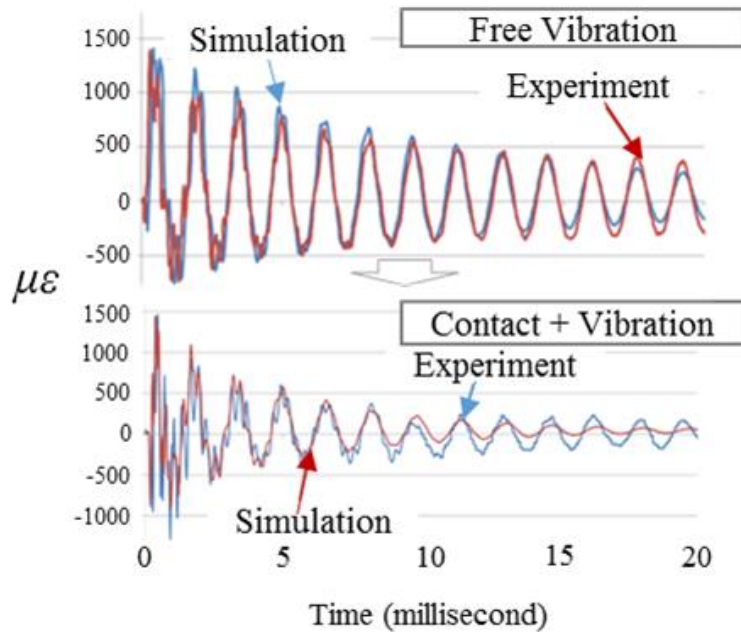


Figure 23: Calibration results of damping and contact parameters

4.4.2. Simulation Results

The multi-scale (global-local) FEA model is calibrated with experimentally obtained dynamic strain histories, measured on the PWB. Four model parameters are calibrated using this procedure: two vibration damping coefficients of the bulk PWB material (mass coefficient of Rayleigh damping α , linear bulk viscosity c) and two soft contact properties (contact stiffness K and critical damping fraction ζ). The bulk damping properties are first calibrated from free vibration tests conducted in addition to the drop test. The contact properties are subsequently obtained from the response after secondary impact during drop tests.

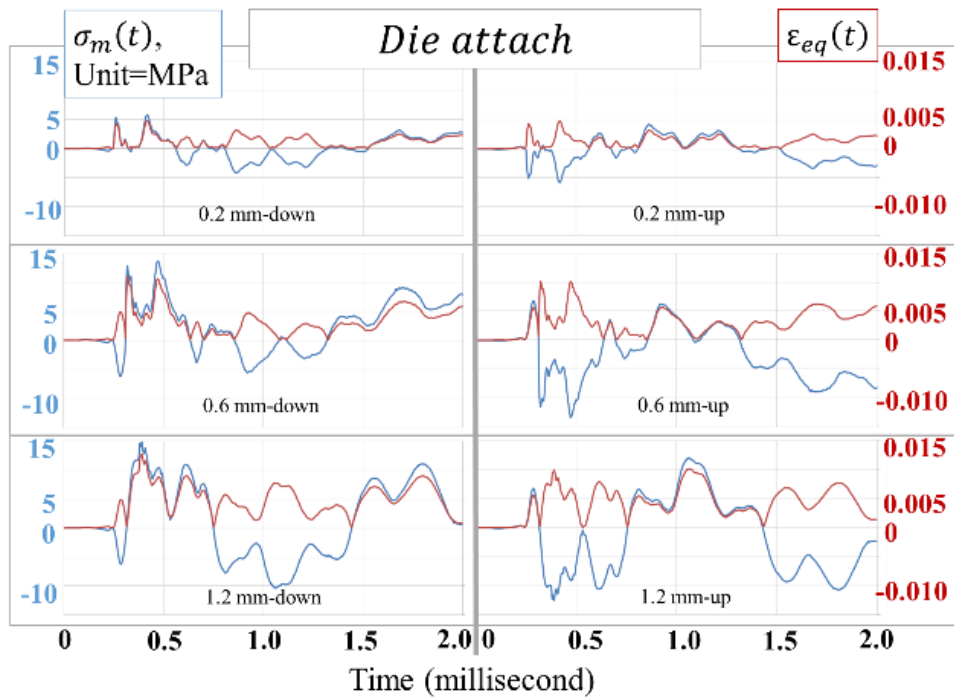


Figure 24: Dynamic response output from critical failure site in die attach

According to the definition of Rayleigh damping: $[C] = \alpha[M] + \beta[K]$, the damping matrix $[C]$ is defined as a linear combination of the system mass matrix $[M]$ and the system stiffness matrix $[K]$. The mass proportional damping coefficient, α , dissipates energy in the lower frequency modes by introducing forces caused by the absolute velocities of the model. The stiffness proportional damping coefficient, β , dissipates energy in the higher frequency modes. The linear bulk viscosity parameter c is adjusted by calibrating the simulation with the test results, for the free vibration response. With $\alpha=375$ and $c=1.0$ in the FEA model, the free vibration strain response of the calibrated FEA model agrees well with the measured strain history (Figure 23) A discussion of calibrating the Rayleigh damping coefficients with further details is available in [104] where non-zero β is used. In is paper, $\beta=0$ is adopted for computational efficiency.

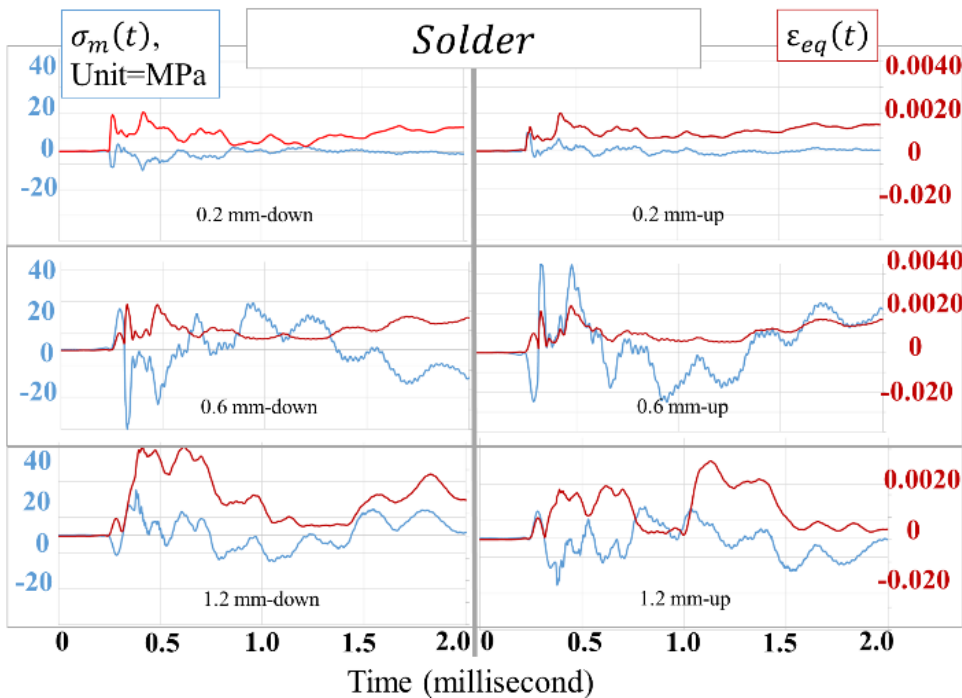


Figure 25: Dynamic response output from critical failure site in solder

The impact between the PWB and the rigid fixture underneath during the drop event is modeled as a soft contact event. The pressure-overclosure relationship (contact stiffness, K) is assumed to be linear. In addition, a dimensionless contact damping coefficient, ζ , called the critical damping fraction, is defined to correlate mass, contact stiffness and relative contact velocity.

After the bulk damping properties of the PWB material are calibrated with free vibration tests, the two contact parameters (K and ζ) are calibrated using the experimental dynamic strain response from the PWB under secondary impact. The simulated strain history is found to match well with the experimental values from the secondary impact drop test (Figure 23), for $K=10$, and $\zeta=1.5$.

The dynamic response at each critical failure site in the MEMS package is extracted from the Level 2 model and plotted in Figure 24-Figure 26, for die attach delamination, solder fracture and wire-bond fracture, respectively. The characteristics of all the presented metrics (e.g. displacement, strain and stress histories) at the critical sites are significantly non-monotonic as the secondary impact severity varies (by changing the clearance between the PWB and the fixture).

In Figure 24 and Figure 25, the hydrostatic stress (negative sign denotes compression) and von Mises' strain histories are shown for six secondary impact conditions with progressively increasing clearance (0.2h, 0.6h and 1.2h); with components oriented either upwards or downwards at each clearance. In particular, bending strain is presented in Figure 26 as the only metric variable for analyzing the wire bond fracture

because wire bond failure is found to be independent of hydrostatic stress. Details are further explained in Section 4.4.3.

Side-by-side plots in Figure 24 and Figure 25 show the dynamic signals from components with opposite facing orientations and same clearance magnitude. It is observed that the von Mises' strain $\varepsilon_{eq}(t)$ histories are almost identical for both downwards-facing and upwards-facing components; whereas the hydrostatic stress histories $\sigma_m(t)$ are almost opposite in phase. This difference in the hydrostatic stress histories provides important insights into the reason why the components facing up have significantly longer lifetime than those facing down during the drop/impact tests.

4.4.3. Damage modeling results

The life prediction model proposed in Equation (1) is used for all the failure sites in this study. The stress/strain inputs are based on simulation of the first drop event of the assembly. The approximation here is that damage accumulated at the first drop is considered as a representative metric for the sequence of all the drop events until complete failure. In this scheme, damage accumulated from each drop can be approximated to be the reciprocal of the characteristic life at the i^{th} failure site; *i.e.* $D_i = 1/\eta_i$.

There are five damage model constants in Equation (1). Three of these constants (t_i , $\Delta\varepsilon_{eq}$, and σ_m) are selected based on the limits of the test conditions, and the remaining two constants (A and B) in Equation (1), are obtained from the drop test results (segregated by failure site) using least square regression. t_i is selected as 2

milliseconds (about forty times the impact pulse duration in drop tests) to capture sufficient duration which may cause damage from significant consecutive local reversals after the impact. Pressure coefficient σ_m' is selected to be $35MPa$ for the relevant models, based on the maximum compressive hydrostatic stress magnitude in all simulated cases. As a result, incremental damage is never a negative value. Fatigue ductility coefficient $\Delta\epsilon_{eq}'$ is selected based on the maximum range of von mises' strain at each failure site among all the simulated cases. Model constants for all three packaging related failure sites are computed, as listed in Table 6.

Table 6: List of model constants

Failure Site	t_i	$\Delta\epsilon_{eq}'$	σ_m' (MPa)	A	B
Die attach	2ms	8.05E-3	35	19.02	2.54
Solder	2ms	1.58E-3	35	4.97	2.88
Wire bond	N/A	3.55E-2	N/A	1.05E-3	0.95

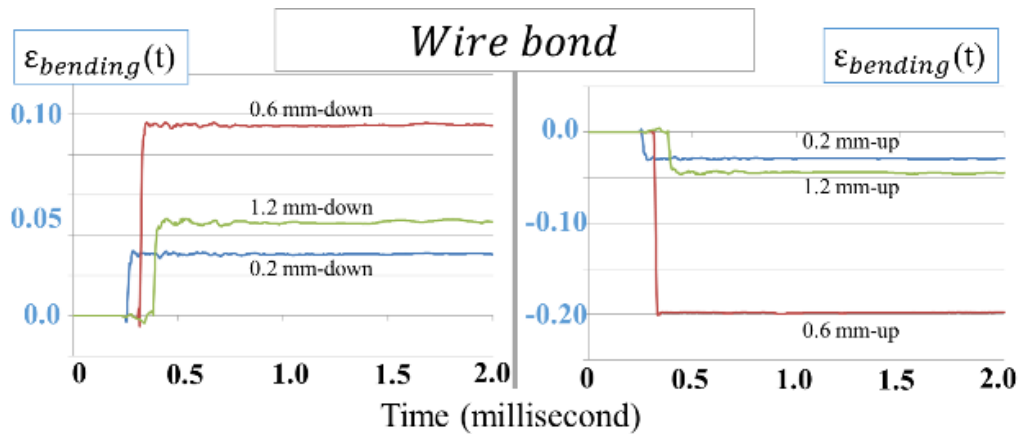


Figure 26: Dynamic bending strain response output from critical failure site in wire bond

Deflection of bond wires can be locally modeled as flexure of curved beams with circular cross-section, where the cyclic mean value of the hydrostatic stress remains zero. The large plastic strain (Figure 26) at the fixed (bonded) ends of the beam makes the effect of post-impact reversals in strain response negligible. Therefore, the integration feature in Equation (1) can be eliminated as well for wire bond failure. Consequently, t_i and σ_m' are not defined in the fatigue damage model for wire bond failure, leading to a fatigue damage model similar to Engelmaier's model for solder joint failures:

$$D_i = A \left(\frac{\Delta \varepsilon_{bending}}{\Delta \varepsilon_{eq}'} \right)^B \quad (4)$$

Using the model constants in Table 6, $\eta_i (=1/D_i)$ prediction for each failure site is fitted with the experimental result. The comparison is summarized in Table 7.

Table 7: Characteristic life of each failure site, Experiment vs. Damage Modeling

Life\MEMS Downwards clearance	0.2h	0.6h	1.2h
Die attach –Experiment	1258	240	46
Die attach -Prediction	1313	119	54
Solder –Experiment	2672	247	36
Solder –Prediction	1003	313	31
Wire bond –Experiment	948	350	N/A
Wire bond –Prediction	952	353	664

Table 8: Characteristic life by failure site, estimated for components oriented upwards

Predicted characteristic life, Components facing UP			
Failure site\Clearance	0.2h	0.6h	1.2h
Solder	5919	323	70
Wire Bond	987	183	679
Die Attach	1382	185	77
Overall	987	183	70

4.4.4. Model Validation and Discussion

To validate the damage model constants for all three failure sites, the model is used to predict the life time at the simulation outputs from drop test simulation in Figure 24- Figure 26. In particular, the damage constants are evaluated from drop tests with the components facing downwards, and the subsequent verification cases had the components facing upwards. The prediction results are compared with the experiments in two ways: (i) characteristic life of MEMS components (only the MEMS package-related failure sites are considered) and (ii) prediction of the dominant failure site for each test condition. Table 7 presents the predicted characteristic life of each failure site for the three test conditions with components facing up, based on simulation results and the model constants in Table 8.

The expected overall lifetime of a MEMS component under each test condition is defined by the lowest predicted characteristic life among the three competing failure sites that were modeled. The overall durability of the MEMS components is estimated for all the six test conditions based on the predicted characteristic life at each failure. The failure predictions are compared with the corresponding experimental results, as plotted in Figure 27. Given the fact that three out of these six conditions are calibrated with the experiment while the other three results are used to test the validity of the simulation outputs, the predicted results are matching quite well with the experiment results.

Table 9: Dominant failure site, test vs. model

Test conditions	Prediction	Experiment
0.2mm-Up	Wire bond	Wire bond
0.6mm-Up	Wire bond	Wire bond
1.2mm-Up	Solder	Wire bond
0.2mm-Down	Wire bond	Wire bond
0.6mm-Down	Die attach	Die attach
1.2mm-Down	Solder	Solder

From another perspective, the proposed fatigue damage models can be further validated by experimental evidence of transition in dominant failure site. In Table 9, predicted dominant failure sites are compared with experimental observations. An expected good agreement is achieved when the components are oriented downwards,

as part of the calibration procedure. For components facing up, predicted dominant failure sites are accurate for 0.2h-Up and 0.6h-Up tests, but an inconsistency occurs for the 1.2h-Up test.

Overall, the proposed damage models show reasonably good prediction capability and are adequate for describing the general experimental trends, both qualitatively and quantitatively. Partial disagreement of dominant failure site (e.g. for the 1.2h-Up test) might be because the model constants obtained for wire bond failure are based on only two test data points (0.2h-Down and 0.6h-Down), while the other two failure sites (die attach and solder joint) are both fitted with three test datasets each (0.2h-Down, 0.6h-Down and 1.2h-Down). Confidence levels for the model constants, especially for wire bond fatigue, are expected to improve when additional test results are used for model calibration.

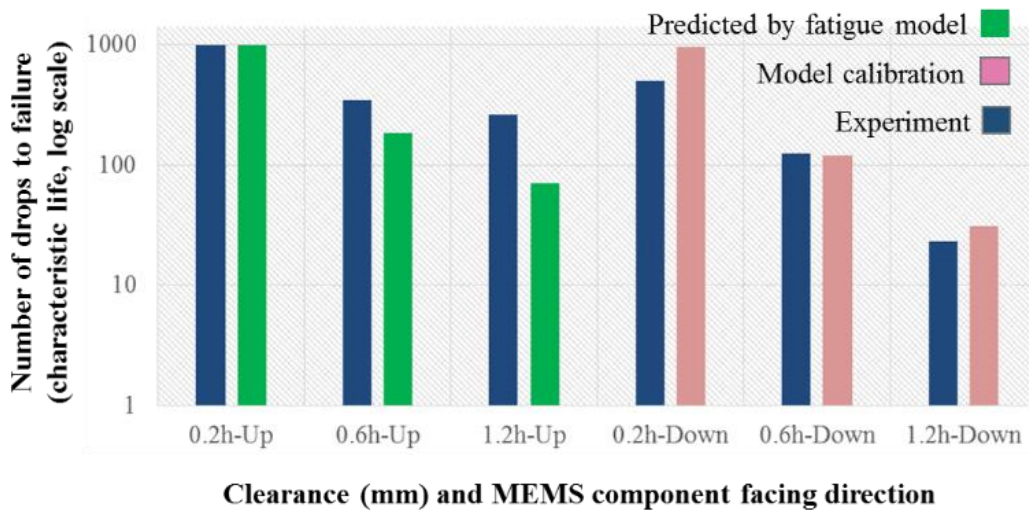


Figure 27: Characteristic life of MEMS components, experimental vs. fatigue modeling results

In summary, the model accuracy is currently limited by: (i) the limited data available to capture the probabilistic variations in the failures; and (ii) approximations in the simplified simulations and in the proposed damage models. Examples of such simplifications include the influence of through-thickness high frequency vibration of the PWB (due to secondary impact) on failure sites with high resonant frequencies (*e.g.* wire bond die attach, solder joint and MEMS device).

4.5. Conclusion

The ‘global-local’ multi-scale FEA simulation approach used in this study is useful to capture the detailed dynamic material responses at various failure sites of the MEMS package in a MEMS PWA when subjected to drop and shock loading. Calibration using dynamic strain response measured on the PWB is found to be efficient for estimating PWB bulk damping properties and the soft contact parameters for the secondary impact.

A 2-parameter, power-law, fatigue damage modeling method is introduced, for predicting the competition of failure modes at competing failure sites in MEMS components assembled on a PWB. In the proposed model, a hydrostatic stress correction factor and a time domain integration approach are both incorporated to address the influence of mean stress and local post-impact vibrations on fatigue damage accumulation in drop tests. The damage model constants are obtained from experimental results of failures at the corresponding sites. During the model verification tests, the models are found to demonstrate good prediction capability when describing the transition phenomenon of dominant failure sites, as well as for estimating the overall durability of MEMS microphone components in drop tests with secondary impacts.

Acknowledgement

We would like to thank the Microsoft Mobile Oy (Finland) and the Lansmont Corporation for their assistance in all our drop testing and research. We wish to acknowledge the members of Center for Advanced Life Cycle Engineering (CALCE) at the University of Maryland for sponsoring this study.

Chapter 5. Influence of Secondary Impact on Printed Wiring Assemblies: Part I - High Frequency ‘Breathing Mode’ Deformations in the Printed Wiring Board

This presents a frequency domain analysis in the SMT assembly length scale. The impact acceleration traverses from the contact site at the bottom of the PWB to the component on the top side of the PWB. The dependence of the dynamic response of the PWB’s top surface on the impact acceleration profile is investigated. Some preliminary results in this chapter was published as a conference proceeding in the ASME InterPACK 2015 Conference, and has been recommended for inclusion in a special ASME JEP issue. The current chapter is published on Journal of Electronic Packaging, 2016 March.

5.1. Abstract

Design rules for portable electronic device are continuously striving for thinner printed wiring assemblies (PWAs) and smaller clearances because of ever-increasing demand for functionality and miniaturization. As a result, during accidental drop and impact events, there is an increased probability of internal secondary impact between a PWA and adjacent internal structures. In particular, compared to the initial impact, acceleration pulses caused by contact during secondary impacts are typically characterized by significant increase of amplitudes and frequency bandwidth. The resonant response in thickness direction of printed wiring boards (PWBs) (termed the dynamic ‘breathing mode’ of response, in this study) acts as a mechanical bandpass

filter and places miniature internal structures in some components (such as MEMS) at risk of failure, if any of them have resonant frequencies within the transmitted frequency bandwidth. This study is the first part of a two-part series, presenting qualitative parametric insights into the effect of secondary impacts in a printed wiring assembly (PWA). This first part focuses on analyzing the frequency spectrum of: (i) the impulse caused by secondary impact; (ii) the energy transmitted by the dynamic ‘breathing’ response of multi-layer PWBs; and (iii) the consequential dynamic response of typical structures with high resonant frequencies that are mounted on the PWB. Examples include internal deformable structures in typical surface mount technology (SMT) components and in MEMS components. The second part of this series will further explore the effects of the ‘breathing mode’ of vibration on failures of various SMT components of different frequencies.

Keywords: portable, drop test, high resonant frequency, laminate, PWB, damping, nonlinear contact properties, MEMS

5.2. Introduction

Impact loading is commonly seen in portable devices due to accidental drops. Relevant shock accelerations can reach up to tens of thousands of g's ("g" is the gravitational acceleration) [15], [26], [105]–[107], especially in the presence of secondary impacts between internal structures. Understanding how such secondary impacts can affect the functionality of the product is critically important in assessing and improving the robustness of portable electronic devices. Secondary impact is one of the reasons for highly amplified internal contact stresses and accelerations, resulting in damage to the internal subsystems [1], [2], [26], [108]. During secondary impacts, contact force pulses with extremely short duration (tens of micro-seconds) are experienced by PWBs, at locations that can be very close to the footprint of packages mounted on top of the PWBs. As a result, various high frequency dynamic response modes can be induced in the PWB, including higher mode (kHz) PWB flexural modes and high frequency (MHz) 'breathing' vibrations in the thickness direction of the PWB. It should be noted that the frequency range in the latter case is already close to the natural frequencies of the internal structures of many surface mounted components, especially of many MEMS components [83]–[86]. This study is the first part of a two-part series exploring the effect of secondary impacts in a printed wiring assembly (PWA). This first part focuses on analyzing the resulting 'breathing mode' of vibration in the PWB due to the propagation of the contact stress through the thickness. The second part of this series will further explore the effects of this 'breathing mode' of vibration on failures of various SMT components of different frequencies.

High frequency oscillations are a natural result of stress wave propagation through the thickness of laminated heterogeneous structures like PWBs, due to multiple reflections at internal interfaces and at the free surfaces [90]–[92]. When a finite-thickness medium is being considered, stress waves from free-boundary reflection will be superimposed on the wave signals caused by multiple reflections and transmissions at internal interfaces (i.e. [93]), giving rise to elastic vibration in the thickness direction of the PWB. This vibration mode in the thickness direction is being termed the ‘breathing mode’ of vibration in this study. As the thickness of the PWB layers decreases, and the material stiffness increases, the frequency of the ‘breathing mode’ increases. Even though the contact stress waves propagating through the thickness decay to negligible amplitudes soon after the impact event due to damping, hundreds of noticeable reversals can still appear at high oscillation frequencies within a short duration.

This study focuses on the drop durability of MEMS components that are mounted on laminated PWBs and subjected to drop events with secondary impacts. Typical MEMS structures have natural frequencies that are well above frequencies encountered in common usage. As a result, MEMS appear rugged in conventional drop qualification tests. However, tests that generate high-frequency oscillations in board-level drop tests were shown to facilitate damage to micro-scale structures in SMT components and in MEMS devices [81], [6], [4]. Such high frequency oscillations of the PWB can either be caused by high flexural modes of the PWB [81], or by contact stress wave generated from secondary impacts [4], [6]. Identifying the influence of such high frequency oscillations on potential damage modes in micro-

scale structures mounted on the PWB is therefore important. This paper provides qualitative parametric insights into the dependence of these high frequency oscillations on relevant structural parameters such as material properties and the multilayer architecture.

The layout of this paper is as follows: A detailed parametric analysis is carried out to gain insights into the influence of secondary impacts on a PWB containing a surface mounted micro-scale structure with high natural frequency. The secondary impact parameters being studied include: (i) pulse width; (ii) pulse shape; and (iii) number of layers in PWB. High frequency ‘breathing mode’ of vibration response through the thickness of PWBs is characterized at the PWB surface opposite to the impact side, using a frequency domain analysis method. Finally, the effect of the high frequency ‘breathing’ vibration on the dynamic response of a micro-scale structure mounted on top of the PWB is investigated.

5.3. Problem Statement and Approach

In this section, background and motivation are introduced, followed by an overview of the analysis approach. Model geometry, other model features and parameters are discussed in detail. Finally, relevant analysis methods are described.

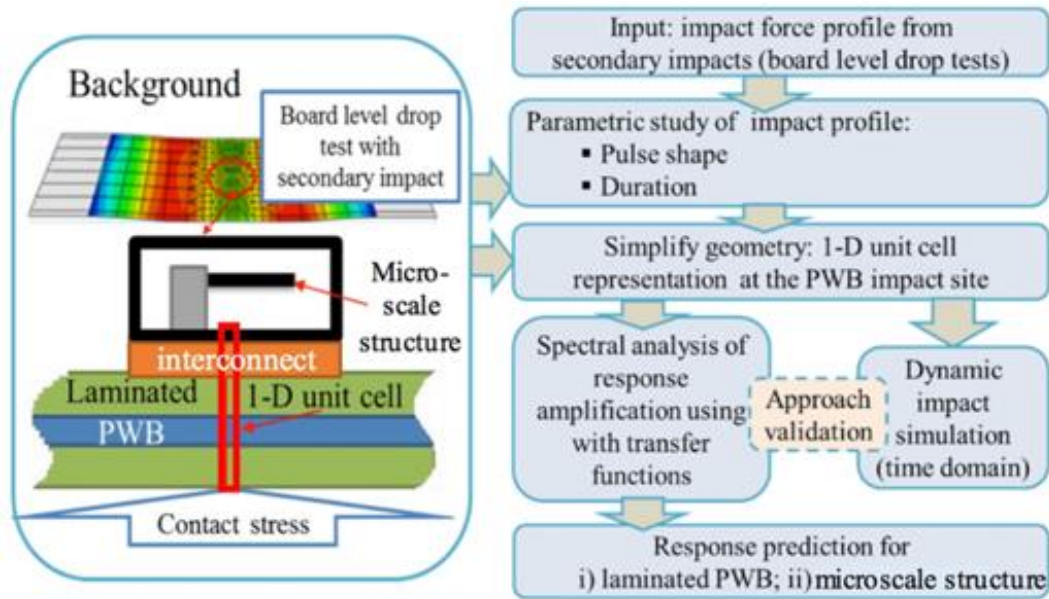


Figure 28: Background and Approach

5.3.1. Test Environments, Background and Flow Chart

Direct impacts on a PWB during a drop event have several effects on the dynamic response. This study is focused on the resulting competing failure modes in MEMS components that are mounted on the PWB during such secondary impacts [6]. Common failure modes within the component include those with high natural frequencies such as wire bonds and fractures in the MEMS device itself, because of the high frequency response of the PWB after secondary impacts.

In [4], [6], [103], [109], drop tests were conducted on a commercially available drop tower equipped with a mechanical acceleration amplifier termed DMSA (Dual Mass Shock Amplifier), to provide shock pulse with a width less than 0.1 millisecond and acceleration peaks of 20,000g. This acceleration profile was selected to mimic the conditions of potential secondary impact events, that can arise in conventional electronic products [15], [26], [110]. A PWA (101 mm x 48 mm, 1.048 mm of thickness) assembled with six MEMS microphone components along its centerline is mounted on top of the DMSA. Finite clearance is introduced between the PWB bottom surface and the fixture base, by using spacers of appropriate thickness, to allow secondary impacts between the test specimen and the mounting fixture. Such secondary impacts can generate acceleration pulses (and contact stress pulses) with even higher amplitudes and shorter pulse widths than those measured from the DMSA.

In Figure 28, a frequency domain analysis approach is described. The analysis starts by characterizing the acceleration pulses from secondary impact tests. Then, the amplitude transfer functions (transmissibility) for ‘breathing mode’ response of PWB structures with varying numbers of layers are extracted from random vibration analysis [111], [112]. The frequency domain approach, validated by time domain finite element analysis (FEA), is further applied to estimate the dynamic response of the PWB itself, as well as of the micro-scale structure mounted on the PWB.

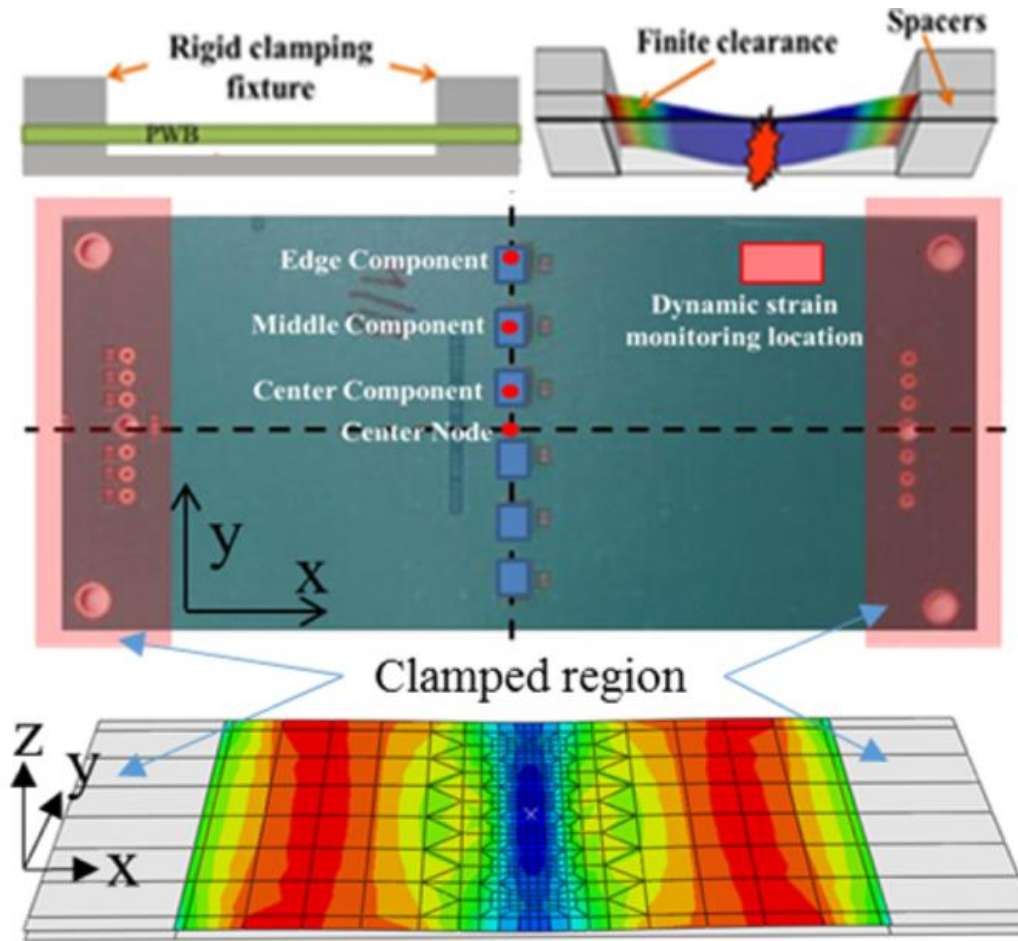


Figure 29: FE model for secondary impact tests

5.3.2. Calibration for secondary impact drop test model

Acceleration histories during secondary impact events are used to quantify the severity of the event. Due to the extremely high acceleration, short duration, and limited satisfactory methods for accelerometer attachment, monitoring data directly from the impact site of the PWB is not practical. The behavior of the PWB is obtained from a calibrated transient dynamic FE model, as shown in Figure 29. In the PWB-level FE model, dynamic bending behavior of the PWB is modeled with shear-deformable, orthotropic, 15-ply shell elements. Mass of each component is

considered in the FE model to account for the effect of inertia force. Vertical acceleration inputs from the drop tower are applied to the rigid clamping fixture as boundary conditions (termed “input-g” method [20]). Secondary impact between test specimen and the mounting fixture is simulated as “soft contact”, which will be explained in more detail in Section 0.

In the simulation, vibration damping and contact parameters are determined systematically using two sets of dynamic strain data recorded during the drop tests: one is from a vibration drop test without any secondary impact (with peak acceleration of 8,000 g), the other is from a drop test with secondary impact (with peak acceleration of 20,000 g, and with 60% PWB thickness of clearance). All the strain data are measured from the strain gage attachment location shown in Figure 29.

5.3.2.1. Rayleigh Damping Calibration

The non-conservative energy dissipation in the PWB during vibration is modeled via Rayleigh damping. As shown in Equation (5) a, the damping matrix $[C]$ is a linear combination of the mass matrix $[M]$ and the stiffness matrix $[K]$ of the system. For the i th mode with damping factor ζ_i , α and β are correlated by the corresponding natural frequency ω_i .

$$\begin{aligned} [C] &= \alpha[M] + \beta[K] \\ \alpha + \omega_i\beta &= 2\zeta_i\omega_i \end{aligned} \tag{5}$$

The two unknowns in Equation (5), α and β , can be evaluated based on two modes, m and n , with known natural frequency and damping factor of each mode. Therefore, the Rayleigh damping coefficients can be obtained as:

$$\alpha = \frac{2\omega_m \omega_n^2 \zeta_m - 2\omega_n \omega_m^2 \zeta_n}{\omega_n^2 - \omega_m^2}, \beta = \frac{2\omega_m \zeta_m - 2\omega_n \zeta_n}{\omega_m^2 - \omega_n^2} \quad (6)$$

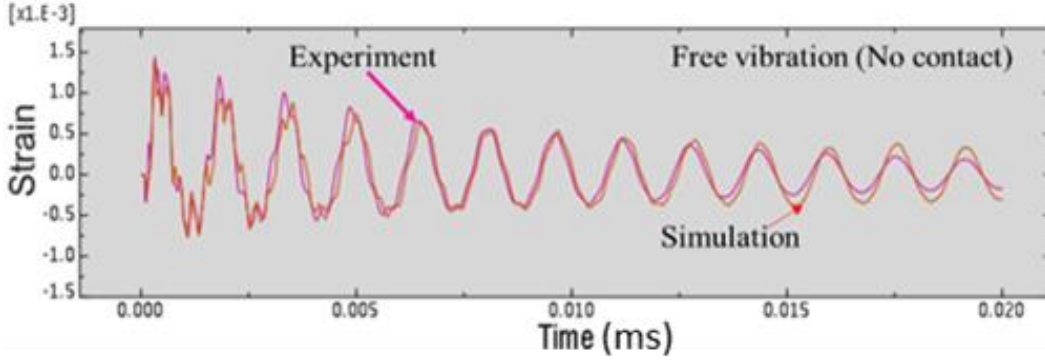


Figure 30: Free Vibration, Rayleigh Damping

Table 10: Rayleigh Damping Coefficients

	Mode 1	Mode 3
Natural Frequency (rad/s)	3836	21911
ζ	0.023	0.015
α (rad/s)	163	
β (s/rad)	1.04E-06	

Based on the strain signal from the experiment, half-power point method [113] is utilized to calculate the damping factor of each mode. Spectrum of the strain signal is obtained by applying fast Fourier transform (FFT) algorithm to the time domain strain signal, yielding peaks for different modes of the PWB. Since Mode 1 and Mode 3 have the highest magnitudes, they are used for calculating α and β . The results are summarized in Table 10.

Using the Rayleigh damping coefficients in Table 10, the simulation result is in good agreement with the experiment, as shown in Figure 30.

5.3.2.2. Contact Stiffness

The impact between PWB and the rigid fixture underneath is modeled as penalty soft contact [114]. The penalty contact method approximately enforces the contact constraints using weight functions that represent contact stiffness. Different from the kinematic contact algorithm [114], the penalty contact method allows for finite penetration of the nodes of the slave body into the master body, represented by a pressure-overclosure behavior of the contact pair. A non-dimensional damping ratio is defined as a fraction of critical damping associated with the contact stiffness. The induced damping forces are related to nodal mass, nodal contact stiffness and relative contact velocity [114].

To evaluate the contact stiffness used in the simulation, Young's modulus and surface roughness of the PWB are measured using a nano-indentation tester. The PWB is a multi-layered, heterogeneous material-system with complex orthotropic stiffness distribution. In the range of interest of the contact pressures shown in Fig 4 of this study, the surface layers (and not the inner layers) play the dominant role in the contact dynamics. In our test specimen, these surface layers are non-reinforced homogeneous isotropic materials. Since our intent in this paper is to provide qualitative parametric insights into the general effects of the contact dynamics in multilayers structures, we have elected to represent the effective contact stiffness of this surface layer with a single averaged isotropic value. Furthermore, to limit the

length scale of our measurement to the approximate thickness of the surface layer, we have used a nano-indentation method (rather than a micro-indentation method which could be contaminated by the properties of the inner layers). The tests are performed at five random locations of the topmost layer, yielding an average Young's modulus of 6.9GPa with 0.6GPa standard deviation. Contact stiffness of a perfectly smooth PWB surface is estimated as $k_{\max}=E_{\text{PWB}}/(1-\nu^2)/d_{\text{th}}$, where E_{PWB} , ν and d_{th} are Young's modulus, Poisson's ratio and PWB thickness, respectively. However, the actual surface of PWB has certain roughness which can introduce extra non-linearity to the pressure-overclosure correlation of the contact pair. The classical analytical correlation between applied load and surface asperities with a statistic distribution $\phi(z)$ was proposed by Greenwood and Williamson [115] for an elastically deformed contact pair:

$$P(d) = \frac{4}{3} \eta A_n E R^{0.5} \int_d^{\infty} (z-d)^{1.5} \phi(z) dz \quad (7)$$

where P is the applied load, A_n is the nominal contact area, E is the composite elastic modulus for the two contacting surfaces defined as $E=E_1E_2/[E_2(1-\nu_1^2)+E_1(1-\nu_2^2)]$, η is the areal density of asperities, R is the radius of curvature of asperity summits, d is the mean separation based on asperity heights. Polycarpou et al. [116] proposed a closed-form solution of Equation (7) by describing the asperity height distribution at the rough surface using an exponential distribution: $\phi=ce^{-\lambda d/\sigma}$, with c , λ being model constants and σ representing the RMS roughness of the surface. Therefore, the nominal applied contact pressure p is derived as:

$$p(d) = \frac{P(d)}{A_n} = \frac{c\sqrt{\pi}\eta\sigma RE}{\lambda^{5/2}} \left(\frac{\sigma}{R}\right)^{1/2} e^{-\lambda d/\sigma} \quad (8)$$

Assuming the contact begins at $d=5\sigma$, then the overclosure value h can be expressed as $h=5\sigma-d$. As h further increases (d decreases), the surface asperities are progressively flattened and the contact stiffness increases to reach k_{max} . Following this method, the pressure-overclosure correlation computed for the contact pair is shown in Figure 31, using the parameters summarized in Table 11. Among them, η , R , c , λ are obtained from the literature [116], [117].

Table 11: Contact modeling parameters

E_{pWB} (GPa)	6.9	η (μm^{-2})	0.13
ν_{pwb}	0.3	R (μm)	2.4
$E_{substrate}$ (GPa)	71.7	σ (μm)	0.2
$\nu_{substrate}$	0.33	c	17
E (GPa)	6.93	λ	3

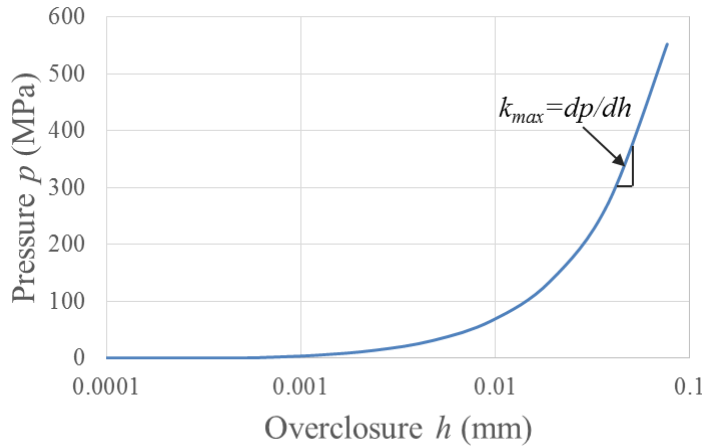


Figure 31: Pressure-overclosure correlation, k is contact stiffness

With the non-linear pressure-overclosure correlation in Figure 31 and the Rayleigh damping parameters in Table 10, the critical damping fraction is calibrated to match

the strain outputs from simulation with the experiment. As shown in Figure 32, the calibrated simulation result agrees well with the experiment.

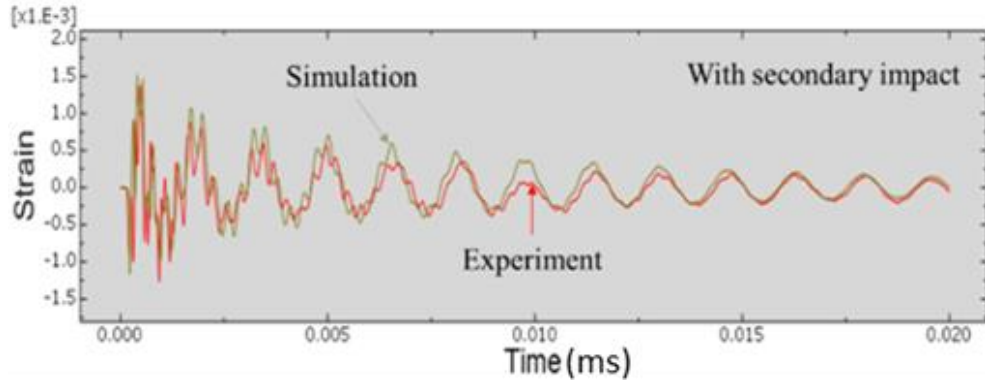


Figure 32: Secondary impact, soft contact

5.3.3. Loading Profile from Secondary Impacts

Using the calibrated secondary impact model with a boundary condition of 20,000g of acceleration, secondary impact induced acceleration histories are extracted for different clearances between the PWA bottom and the top of the fixture, varying from 20% to 120% of the PWB thickness.

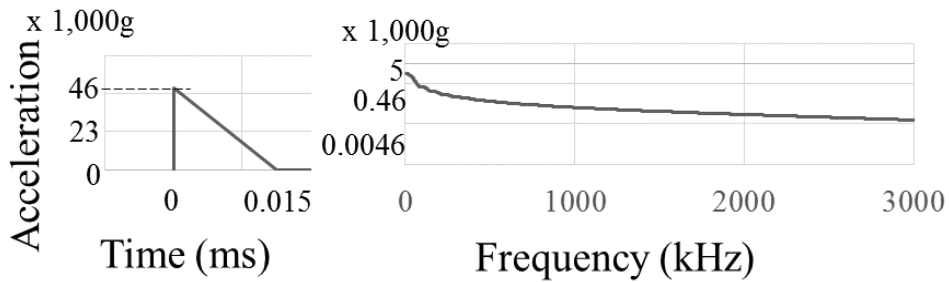


Figure 33: Sample impact acceleration input to the PWB

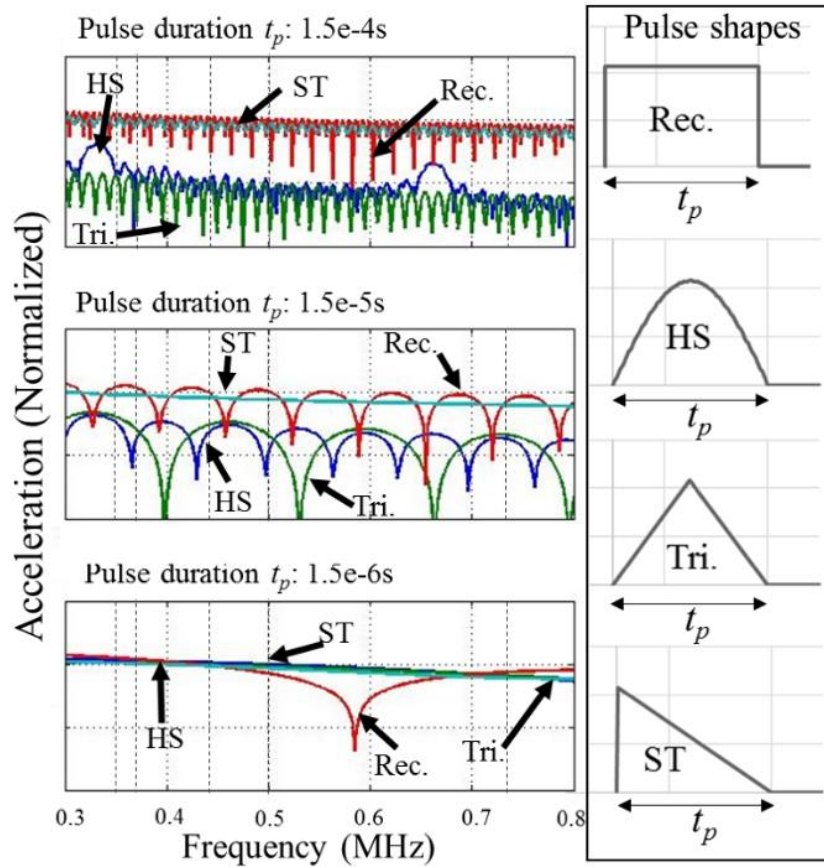


Figure 34: Spectrum of Input pulses with different shapes

The acceleration pulse duration, t_p , at the footprint of the SMT components in secondary impact tests ranges from microseconds to 10s of microseconds. The impact induced acceleration contains a sharp rise followed by a relatively slower decay. This can be visualized as a combination of saw-tooth and half-sine curves. An idealized saw-tooth shaped representation of acceleration pulse due to secondary impacts to the PWB is shown in Figure 33. In this study, since the response profile is much longer than the impulse profile, the sampling frequency and record length in the simulations are fixed at $\Delta=5e-4$ s with 5000 data points. The theoretical frequency bandwidth is therefore up to 5.0 MHz, considering the Nyquist frequency.

For a dynamic system at a specific frequency, the higher the excitation amplitude, the higher the response magnitude would be. Therefore, with a fixed t_p , the difference made by the pulse shape can be viewed in the frequency domain. Figure 34 shows the acceleration spectrum for different pulse shapes. In terms of magnitudes, it is observed that saw-tooth (ST) and rectangle (Rec) shaped pulses are not very much different as t_p changes, because of the same sudden increase at the beginning of each ST and Rec pulse profiles. However, t_p does is an important parameter when it comes to the spectrum amplitudes for half-sine (HS) and triangle (Tri) pulses: the shorter the t_p , the higher the amplitude is. Overall, high response magnitude of a pulse signal is determined by its high ramp rate.

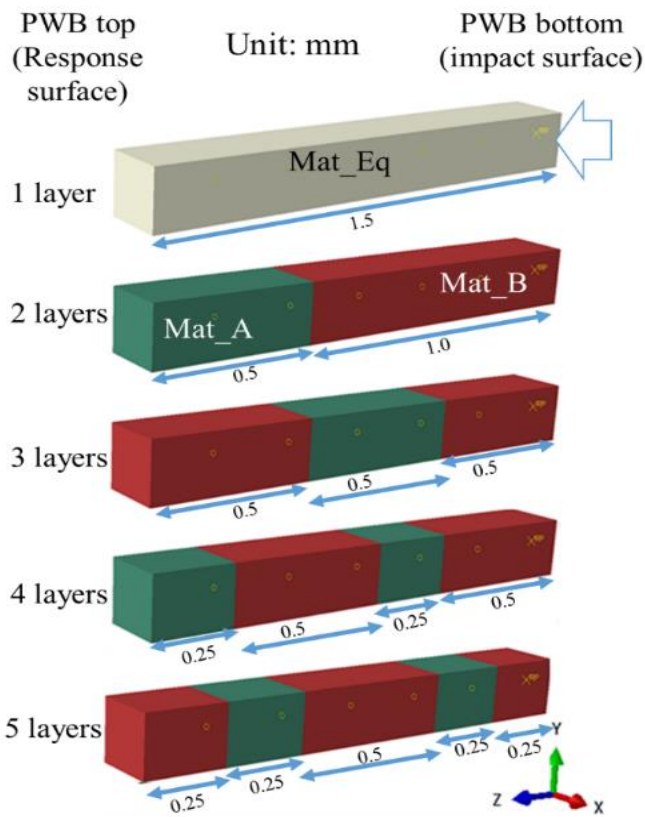


Figure 35: Multi-layered 1-D unit cell structure for PWB

5.3.4. Geometric Simplification in Thickness Direction

During the impact, the maximum contact area is above 100 mm^2 . It is more than ten times of the MEMS component's footprint area, whereas the thickness of laminated PWB is only 1.048 mm. Therefore, stress at the impact site on the PWB is approximated with a uniform distribution, and the corresponding stress wave propagating from the contact surface is approximately planar. This assumption allows a 1-D approximation for analyzing the dynamic response and stress wave propagation through the thickness of the multi-layered PWB. The analysis is therefore simplified with a 1-D rod to represent a unit cell of the PWB. To mimic the actual loading condition, one side of the 1-D rod is subjected to impact while a micro-scale device, with high resonant frequency, is mounted at the other end of the rod.

Table 12: Material properties used in 1-D rod model

	Mat_A	Mat_B	Mat_Eq
Modulus of elasticity (GPa)	8	80	36
Density (mg/mm^3)	2	5	4
Poisson's ratio	0.3	0.3	0.3
Wave speed (mm/s)	2E+06	4E+06	3E+06

Since neither the interconnect layer, nor the micro-device substrate are independently modeled, their thicknesses are included as additional 0.5 mm thickness of the multi-layered PWB. The dimensions of these 1-D unit cell PWB models, with up to five

layers through the thickness (z-axis), are illustrated in Figure 35. Idealized linear elastic material properties, as listed in Table 12, are assigned to the individual layers of the laminated PWB models. “Mat_A” and “Mat_B” with fixed volume ratio are periodically distributed through the PWB thickness. “Mat_Eq” is a reference material, used in the single layer model, so that the smallest stress wave transit time from one side to another is $0.5e-6s$ for all the cases.

FEA is conducted for the multi-layer PWB models, both in the time-domain and also in the frequency domain. Frequency domain analysis is conducted with a ‘white-noise’ input, to parametrically extract the transfer function (transmissibility) for each structure. In the time domain transient dynamic analysis, the phase relationship of dynamic response at natural frequencies is investigated. Moreover, time domain analysis serves as a reference to verify the frequency domain analysis results.

5.3.4.1. Stress wave reflections and resonance

Governing equation of motion for one layer, 1-D rod structure can be solved based on D’Alembert’s principle. Further, the first natural frequencies [118] and the periodic reflection frequency of stress wave [119] can be proved to be identical. Therefore, frequencies of periodic stress wave reflection and propagation should agree with the natural frequencies of the structure.

5.3.4.2. Damping ratio

The influence of damping on high frequency response of multi-layered structure is analyzed. Damping ratio ζ , defined with respect to critical damping, can influence the peaks of amplitude response curve in the following pattern [113]:

$$H_{\max} = \frac{1}{2\zeta\sqrt{1-\zeta^2}} \quad (9)$$

In this paper, PWB models are defined with a range of damping ratio between 0.01 and 0.1.

5.3.5. Geometric Simplification: Micro-beam

Acceleration response on top of 1-D PWB models are further applied to a micro-beam model, with high resonant frequency, as shown in Figure 36. In the micro-beam model, uniaxial acceleration inputs along z-axis are applied to the bottom of rigid body substrate. The left end of a horizontally placed cantilever beam is fixed in all degrees of freedom to the substrate. Vertical acceleration response at the free end is monitored as outputs.

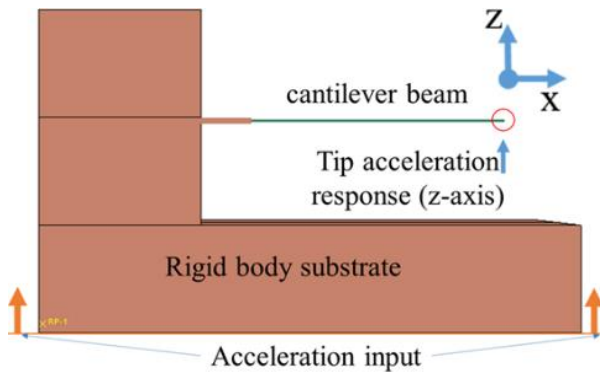


Figure 36: Micro-beam model

Resonant frequencies of MEMS devices and packages have a wide range from kHz to MHz ([83], [85], [86]). Therefore, in this study, the first natural frequency of the cantilever beam is arbitrarily selected to be 0.44 MHz, based on the natural frequencies of the multi-layered 1-D unit cell models described in Figure 35.

5.3.6. Amplitude Transfer Function

The amplitude transfer function, $H(\omega)$, for each condition (number of layers and damping ratio) is obtained from white-noise random vibration analysis. This transfer function also represents the dynamic transmissibility of the structure.

In frequency domain analysis, magnitudes of dynamic signal input $X(\omega)$ and output signal $Y(\omega)$ can be correlated by $H(\omega)$ [113]. Input and output Power spectrum density (PSD), $S_X(\omega)$ and $S_Y(\omega)$, can be defined as the magnitude square at each infinitesimal frequency bandwidth df . Therefore, $H(\omega)$ at the response surface of a structure can be obtained by comparing the PSD curves of the input and output signals:

$$H(\omega)^2 = \frac{Y(\omega) \cdot Y^*(\omega) / df}{X(\omega) \cdot X^*(\omega) / df} = \frac{S_Y(\omega)}{S_X(\omega)} \quad (10)$$

White noise acceleration PSD input with constant PSD magnitude is applied to a bandwidth of $(f_2 - f_1)$. $f_1=0.2\text{MHz}$ and $f_2=5.0\text{MHz}$ are defined to include all the first five natural frequencies of all the laminate combinations. Based on Equation (10), an example of $H(\omega)$, based on the ratio between input and output PSD curves, is demonstrated in Figure 37. Random vibration FEA conducted in the frequency domain is based on modal superposition method with no material non-linearity being considered. The $H(\omega)$ curves are dependent on material properties, laminated structure, and damping ratio.

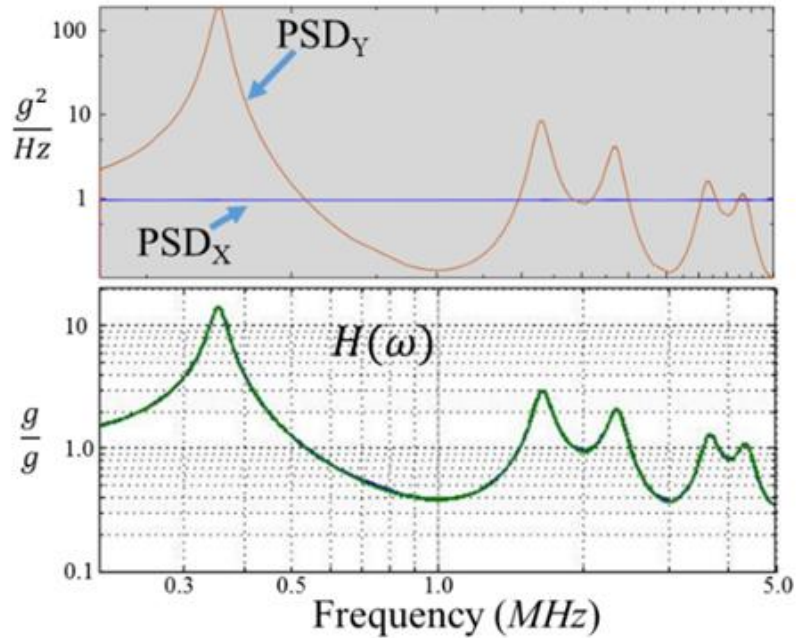


Figure 37: Acceleration amplitude transfer function $H(\omega)$ obtained based on random vibration simulation (example condition: 3-layer model, $\zeta=0.04$)

For comparison, Figure 38 shows the output from a sample time domain dynamic simulation. It shows that the high frequency oscillation becomes significant after the input pulse reaches its peak (around 9 micro-second in Figure 38). Thus we can consider the extraction procedure of $H(\omega)$ to produce the same results as those from time domain dynamic simulation.

The transfer function obtained from random vibration analysis is utilized twice: once for the laminated PWB model and once for the response of the micro-beam on top of the PWB. The drawback of not using impact force as inputs to the PWB bottom is of course the expected slight shift in natural frequencies and amplitudes of high frequency oscillations at the PWB top surface. However, for qualitative

demonstration purpose of high frequency oscillation due to secondary impacts, the approximation is believed to be acceptable.

Since the mass of micro-scale structures is comparatively small, inertial effects are neglected and the input acceleration to the micro-beam model is equal to the output from the 1-D PWB unit cell models. Therefore, the response of PWB and micro-beam structure can be respectively correlated with the impact pulse as:

$$\begin{aligned} |Y_{PWB}(\omega)| &= H_{PWB}(\omega) \cdot |X_{impact}(\omega)| \\ |Y_{microbeam}(\omega)| &= H_{microbeam}(\omega) \cdot H_{PWB}(\omega) \cdot |X_{impact}(\omega)| \end{aligned} \quad (11)$$

where $|Y_{pwb}(\omega)|$ and $|Y_{microbeam}(\omega)|$ denote the acceleration response spectrum at the PWB top and tip of micro-beam, $|X_{impact}(\omega)|$ is the spectrum of input acceleration applied to the bottom of PWB, and $H_{microbeam}(\omega)$ and $H_{pwb}(\omega)$ are the amplitude transfer functions for the micro-beam and PWB ‘breathing’ models, respectively.

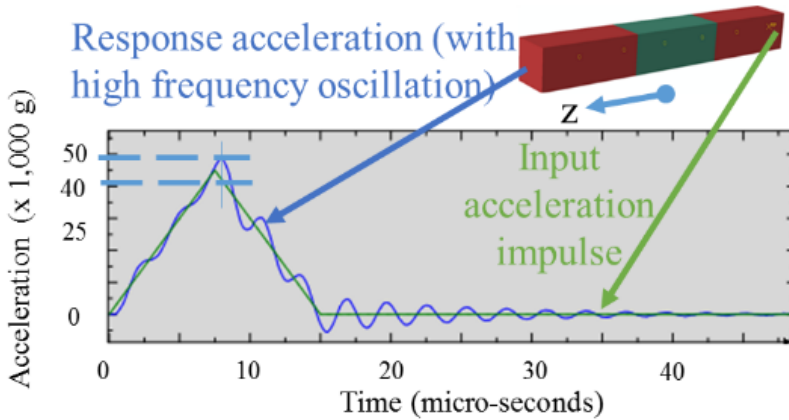


Figure 38: Sample output from time domain simulation (3-layers PWB, $\zeta=0.04$, pulse shape=triangle, $t_p=1.5E-5s$)

5.3.7. Amplitude Estimation with Damping Ratio

After the PWB is subjected to an impact acceleration, its response acceleration contains ‘breathing mode’ oscillations. Based on an understanding of the time domain signals, an amplitude estimation method of high frequency oscillations using the outputs from frequency domain analysis is carried out.

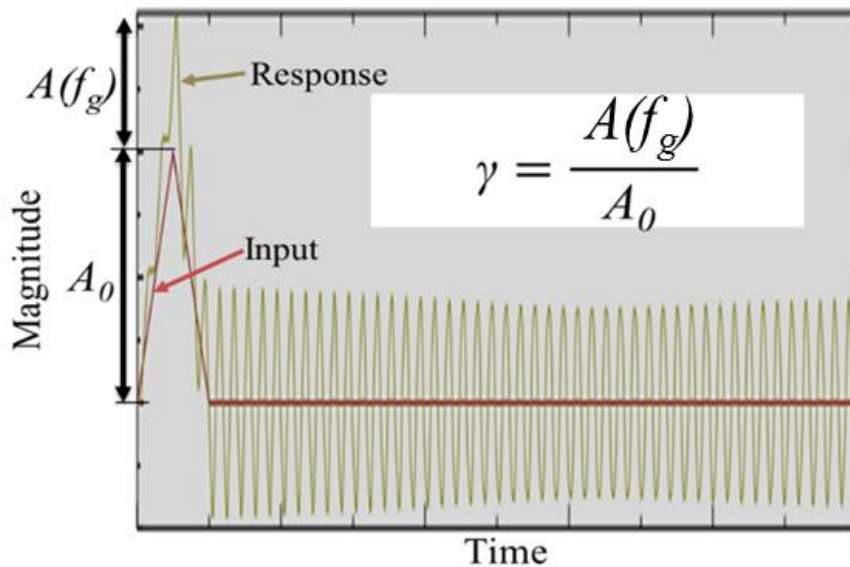


Figure 39: Quantities used in the definition of amplitude ratio γ

For convenience, an amplitude ratio γ is defined and illustrated in Figure 39. The ratio is defined as the difference between the maximum time domain magnitude of ‘breathing mode’ oscillation, $A(f_g)$ in Figure 39, and the magnitude of the input signal (A_0 in Figure 39). γ should be a damping independent value, whereas damping factor can be derived from $A(f_g)$ and a damped amplitude via the logarithmic decrement method [113].

From time domain analysis, it can be observed that the high frequency oscillation decays rapidly following an exponential decay rate. Such exponential decay on damped signals can be mathematically expressed as $\exp(-\zeta\omega t)$, where ζ is the damping ratio, ω is the angular frequency of the resonance oscillation at the top surface of the PWB, Δ is the total duration of the time domain signal. With a high oscillation frequency, the ratio of cumulative amplitude between a damped signal and an undamped signal, starting at the same magnitude, can be approximated as a ratio, q . This ratio is estimated as follows

$$q = \frac{\int_0^{\Delta} e^{-\zeta\omega t} dt}{\int_0^{\Delta} dt} = \frac{1 - e^{-\zeta\omega\Delta}}{\zeta\omega\Delta} \quad (12)$$

q can be utilized to correlate the ‘breathing mode’ response magnitude in frequency domain. By definition of q in Equation 12, frequency f_p and magnitude values A_p from peaks in a spectrum of a damped signal can be utilized to calculate the initial magnitude A before damping:

$$A(f_p) = \frac{A_p(f_p)}{q(\zeta, f_p, \Delta)} \quad (13)$$

As a brief validation using the example in Figure 38, the spectrum of the response signal peaks at ($f_p=0.35MHz$, $A_p=230g$). Using equations (12) and (13) with the given ζ and t_d , A is calculated to be $10,200g$, which is close to the highest magnitude of high frequency oscillation in time domain analysis, shown as the magnitude between the two dash lines in Figure 38. In this example, γ is estimated as $10,200g/46,000g=0.22$.

5.4. Results and Discussions

In this section, the influence of the number of PWB layers and the damping ratio on the response of PWB models is studied. Then, the response of the micro-beam on top of the PWBs is compared to quantify the role of high frequency oscillations in PWB.

5.4.1. Amplitude Response of 1-D PWB Model

Following the procedure discussed in Section 5.3.6, transfer function curves $H(\omega)$ for each of the multi-layer 1-D PWB model is plotted in Figure 40.

For each structure, $H(\omega)$ with damping ratio of 0.01 and 0.1 are compared, to evaluate the range of amplification due to damping. The first five natural frequencies (amplitude response peaks) for all structures are less than 5MHz. Among them, the highest amplitude response is expected at the first natural frequency. As expected, the amplitude response decreases with increase in the damping ratio. Increasing the damping ratio by a factor of 10 (from 0.01 to 0.1) drops the peak of the amplitude response at each resonant frequency by about one order of magnitude, which agrees well with Equation (9).

Natural frequencies are generally different as the number of layers change and there is a non-monotonic trend between natural frequencies and number of layers. The first natural frequencies from different cases range from 0.35 MHz to 0.73 MHz, where 3-layer and 5-layer cases have the lowest first natural frequency and the 2-layer case has the highest. As a result, the 2-layer case also has a very small separation between its first and second natural frequencies, which contributes to a further amplification at both frequencies. By contrast, the 3-layer case has the largest separation between its

first two natural frequencies, and therefore has one of the lowest amplitudes in the second mode.

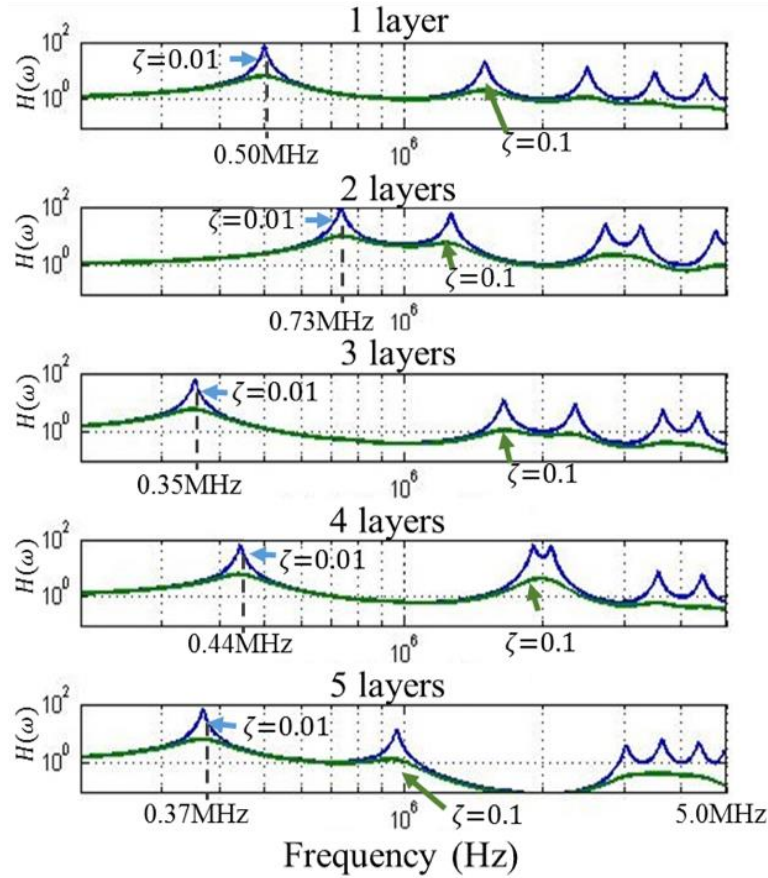


Figure 40: Amplitude transfer functions for multi-layer PWBs

5.4.2. Correlation between pulse width and through-thickness oscillation response of PWBs

As demonstrated earlier, the spectrum of PWB response, $|Y_{pwb}(\omega)|$, can be obtained using Equation (11). $H(\omega)$ for PWBs of different number of layers are already obtained in Section 5.4.1. The significance of high frequency oscillation due to acceleration pulse excitations with different t_p are parametrically studied in this section.

First, a half-sine pulse is generated:

$$a(t) = A_0 \sin(\omega_0 t)[u(t) - u(t - \pi / \omega_0)] \quad (14)$$

where $u(t)$ is step function, A_0 is the magnitude. t_p of $a(t)$ is defined as π/ω_0 .

Table 13: Summary of Acceleration Response at Micro-beam Tip

ζ , micro-beam		0.05		
ζ , 1-D PWB model		0.01	0.1	Rigid (ref.)
1 Layer	f_p (MHz)	0.50	0.44	0.44
	q	0.013	0.014	0.015
	A_p (g)	19,572	4,365	1,030
	A (g)	1,534,404	302,711	70,754
Amplification		22	4	
2 Layers	f_p (MHz)	0.73	0.44	0.44
	q	0.009	0.014	0.015
	A_p (g)	5,373	1,973	1,030
	A (g)	617,641	136,243	70,754
Amplification		9	2	
3 Layers	f_p (MHz)	0.35	0.43	0.44
	q	0.018	0.015	0.015
	A_p (g)	16,453	2,172	1,030
	A (g)	914,866	147,919	70,754
Amplification		13	2	

4 Layers	f_p (MHz)	0.44	0.44	0.44
	q	0.014	0.015	0.015
	A_p (g)	58,145	6,158	1,030
	A (g)	4,050,643	423,192	70,754
Amplification		57	6	
5 Layers	f_p (MHz)	0.37	0.43	0.44
	q	0.017	0.015	0.015
	A_p (g)	22,355	3,074	1,030
	A (g)	1,291,871	209,349	70,754
Amplification		18	3	

Then, the spectrum of $a(t)$ is obtained using the FFT function in Matlab. The spectrum of the input acceleration is multiplied by $H_{pwb}(\omega)$ to get $|Y_{pwb}(\omega)|$. The coordinate of the peak response, (f_p, A_p) , is identified for each $|Y_{pwb}(\omega)|$ plot. Finally, using Equations (12) and (13), γ is computed for each t_p ranging from 1E-7 to 1E-4 seconds.

The γ plots for different multi-layer PWBs are shown in Figure 41. Since γ is a damping independent parameter, only the $H_{pwb}(\omega)$ curves of $\zeta=0.01$ in Figure 40 are used for computation. The amplification for the high frequency ‘breathing mode’ can be as high as 4 for a half-sine pulse excitation for the 2-layer PWB case. The highest amplification occurs generally when t_p is between 1 and 2 microseconds. In other words, when the value of $1/2t_p$ is close to the first natural frequency of the PWB, a

high amplification is expected in the breathing mode response signal. As t_p increases or decreases from 1~2 microseconds, the magnitude of high frequency oscillation decreases. The trend can be approximated by a piecewise power-law (solid line), shown as the last plot of Figure 41.

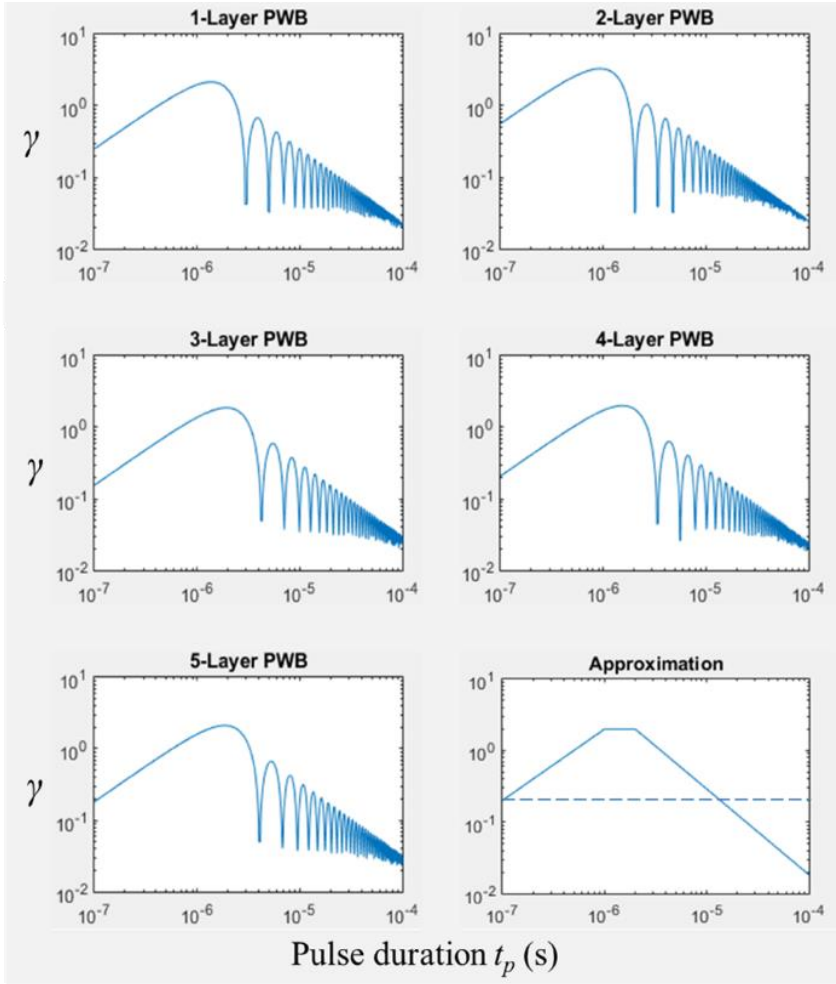


Figure 41: Amplitude ratio γ of high frequency acceleration

5.4.3. Response of Micro-beam structure

The tip response of the micro-beam is computed based on Equation (11), and correlated with the impact acceleration via a two-step analysis of amplitude response:

one from the multi-layered 1-D PWB model and one from the micro-beam itself. The following analysis is based on the idealized saw-tooth input acceleration profile, illustrated earlier in Figure 33, with a fixed $t_p=1.5e-5$. Also, the micro-beam in this section is defined with a fixed damping ratio, $\zeta=0.05$.

For further analysis, multilayer PWBs are studied under three conditions: small damping ratio 0.01, a relatively large damping ratio 0.1, and infinitely rigid in the thickness direction. The rigid case is selected as hypothetical reference case so we can identify the relative contribution of the breathing mode vibration in the deformable case. Since breathing mode response does not occur in PWB that is rigid in the thickness direction, the input acceleration applied to the substrate of the micro-scale structure is identical to that on the PWB bottom.

The results of acceleration response at the tip of micro-beam structure are summarized Table 13. At each condition, five parameters are evaluated: f_p and A_p are frequency and amplitude coordinates of peaks in a spectrum, q is the ratio of accumulated amplitude between damped and undamped condition as defined in Equation (12), and A is the maximum amplitude of the corresponding frequency with damping, calculated as per Equation (13). Amplification factor is calculated for the selected damping ratios, using the A value from a certain damping ratio divided by the A value of rigid body PWB case.

It is observed that when small damping ratio ($\zeta=0.01$) is considered in PWBs, amplification in micro-beam's tip response can go up to 57 times higher than a rigid PWB case for a four-layer PWB. This is reached in special cases when the natural

frequency of multi-layered PWB coincides with the fundamental natural frequency of the micro-beam structure. Even with 66% mismatch of the PWB and micro-beam natural frequencies in the 2-layer case, the response can still amplify nine-fold. When the damping ratio is increased by an order of magnitude ($\zeta=0.1$), the amplification factor can be reduced several-fold, but within one order of magnitude. Still, the micro-beam's tip response can be 2-6 times higher than the rigid body case.

5.5. Conclusions

This study is the first part of a two-part series for the qualitative parametric exploration of the effect of secondary impacts in a printed wiring assembly (PWA). This first part focuses on analyzing the resulting ‘breathing’ mode of vibration in the PWB due to the propagation of the contact stress through the thickness. The second part of this series will further explore the effects of this ‘breathing’ mode of vibration on failures of various SMT components that contain internal structures of different resonant frequencies.

This first part of the two-part series study focuses on the length scale of PWB in through-thickness direction. The analyses illustrate secondary impacts on PWAs can generate high frequency oscillations due to the resonance of multi-layer PWB in the thickness direction (termed ‘breathing mode’ here). The characteristics of such breathing mode vibrations depend on the number of layers in the PWB and are analyzed here using a frequency domain approach. The approach utilizes white noise inputs and finite element simulations to extract the breathing mode transfer functions (transmissibility) of damped PWB structures with different stack-up architectures. Then, the dynamic response spectrum of micro-scale structures mounted on top of the PWB is analyzed by correlating the spectrum of the transmitted profile with the amplitude response curves. This frequency domain approach has been validated with time domain analysis. Using the proposed approach, the dynamic responses of both PWBs and microscale structures mounted atop the PWBs is efficiently evaluated. The response depends on the pulse shapes and durations of impact accelerations,

number of layers in the PWB, and material properties (elastic stiffness and damping ratios). A spectral analysis indicates that with a given pulse width, pulse shapes with steeper rise slopes can induce higher magnitudes in the corresponding dynamic responses of the PWB.

When the inverse of a half-sine pulse's duration is close to two times the first natural frequency of the PWB, the magnitude of high frequency oscillation of the PWB can reach up to 4X that of the input. Results also show that secondary impacts experienced by the PWB in drop tests contain the right frequency content to cause high frequency resonant 'breathing' vibrations in the PWB, resulting in high amplifications in the response of microscale structures mounted on the PWB. These amplifications can range from 2X to 57X, depending on two factors: one is the damping ratio, the other the proximity of the natural frequencies of the micro-scale structures mounted on the PWB to those of the 'breathing' mode response of the PWB.

Acknowledgements

We wish to acknowledge the members of Center for Advanced Life Cycle Engineering (CALCE) at the University of Maryland for sponsoring this study. We would like to thank Microsoft Mobile (Finland) for the continuous support of this research.

Chapter 6. Influence of Secondary Impact on Printed Wiring Assemblies Part II: Competing Failure Modes in Surface Mount Components

The goal of this chapter is to correlate the dynamic response of two competing failure modes in a generic SMT assembly with the participation of PWB flexural modes. Inputs are taken from both the board-level length-scale simulation and PWB's lamina (through-thickness direction) length-scale analysis discussed in Chapter 5. The current draft of this chapter is submitted to Journal of Electronic Packaging for peer-review.

6.1. Abstract

Portable electronic devices are commonly exposed to shock and impact loading due to accidental drops. After external impact, internal collisions (termed “secondary impacts” in this study) between vibrating adjacent subassemblies of a product may occur if design guidelines fail to prevent such events. Secondary impacts can result in short acceleration pulses with much higher amplitudes and higher frequencies than those in conventional board level drop tests. Thus such pulses are likely to excite the high frequency resonances of printed wiring boards (PWBs) (including through-thickness ‘breathing’ modes) and also of miniature structures in assembled surface mount technology (SMT) components. Such resonant effects have a strong potential to damage the component, and therefore should be avoided. When the resonant frequency of a miniature structure (e.g. elements of a SMT MEMS component) in an

SMT assembly is close to a natural frequency of the PWB, an amplified response is expected in the miniature structure. Components which are regarded as reliable under conventional qualification test methods, may still pose a failure risk when secondary impact is considered. This paper is the second part of a two-part series exploring the effect of secondary impacts in a printed wiring assembly (PWA). The first paper in this series focused on the 'breathing' mode of vibration generated in a PWB under secondary impact and this paper focuses on analyzing the effect of such 'breathing' modes on typical failure modes with different resonant frequencies in SMT applications. The results demonstrate distinctly different sensitivity of each failure mode to the impacts.

Keywords: portable electronics, secondary impact, drop test, SMT, MEMS, interconnect, FEA

6.2. Introduction

The ever increasing portability, miniaturization and functionality of consumer electronic products have driven the move to thinner printed wiring assemblies (PWA) and smaller clearances between adjacent components. Accidental drop and shock to the product can not only damage the exterior housing (including screen, micro-switch buttons), but can also cause functional issues within the internal modules. Studies of product level drop tests have shown that when a mobile phone is dropped on a hard surface from the height of 1.5 m, internal accelerations experienced by the PWB can already reach 10,000g [26] (“g” is the gravitational acceleration). Moreover, increasingly dense packaging in leading-edge portable electronic products may further increase the risk of collisions between the internal structures inside the product housing ([1], [2]). Such collisions, termed “secondary impacts” in this study [4], commonly cause acceleration pulses with much higher amplitudes and much shorter pulse widths than those featured in conventional board level drop tests [7]. The new source of contact stress at the impact site would result in a different dynamic response throughout the structure. In JEDEC standard board level drop tests [7] for SMT IC packages, the study of reliability of interconnect materials focuses mainly on stresses due to large PWB bending strain [9]–[11], [19]. When secondary impacts are considered, interconnect failures may be attributed to the bending strain, the large impact acceleration, and the propagation of contact stresses. This paper is the second of a two-part sequence addressing issues of secondary impact in PWAs. The first paper in this sequence discussed the generation of high-frequency ‘breathing mode’ of vibration in PWBs due to propagation of contact stresses. This second part focuses

of the effect of such ‘breathing modes’ of PWB vibration on the failure modes of SMT components with different resonant frequencies.

Many prevailing SMT packages contain miniature deformable structures. For example, MEMS components are widely utilized in several applications: sensors/actuators, portable consumer electronics, radio frequency switches, etc. Depending on the application, MEMS are often operated in harsh environments which include drops and shocks [75]. Since MEMS components are commonly designed with high resonant frequencies [83]–[86], they appear rugged in ordinary operating frequency ranges or in conventional drop qualification tests. Sheehy et al. [87] reported that micro-scale cantilevers were generally durable in common drop tests; failures were insignificant unless the shock acceleration exceeded 40,000g. Srikar and Senturia [16] studied the transient response of MEMS devices due to a shock pulse at the silicon substrate. From the point of view of the microstructure’s natural frequency, it was indicated that most shock loads experienced by MEMS devices are ‘quasi-static’ because the shock pulse is quite long relative to the natural frequencies of the internal structures. However if the contact surface is too rigid, excessive deformations and failures in microstructures may occur even if the drop is just from an ordinary height. Li and Shemansky [15] analyzed the failure risks in the a cantilever beam-type micro-machined structure when subjected to a free fall drop onto a rigid ground. Idealized equivalent acceleration up to 10^5 of g’s from a 1.2 m of free fall have been documented. Such drops have been observed to result in high failure rates.

The reliability of miniature structures is often influenced by packaging. Ghisi et al. [80] conducted drop testing and simulation for a commercial off-the-shelf (COTS) MEMS accelerometer and investigated the effect of packaging on the reliability of MEMS devices. It was shown that MEMS package design can significantly increase the occurrence of failures when the bottom surface of the package is subjected to a shock. Alsaleem et al. [81] pointed out that the presence of second level packaging for MEMS devices may further amplify the dynamic response of the miniature structure. This effect is particularly significant when natural frequency of the miniature structure in MEMS device is close to the natural frequency of the PWB and is within the shock pulse's energy spectrum. During secondary impacts, a wide impact acceleration spectrum is expected due to a short pulse width. Consequently, the dynamic response of the system is likely to have more contributions from higher frequency modes. Such modes include high-order PWB flexural deflection modes, high frequency through-thickness vibration of the PWB (termed PWB 'breathing' mode for the purpose of this study), and resonant vibration of miniature structures within SMT packages.

Prior drop test studies presented by the authors [6], [103] have demonstrated how the secondary impact test method was utilized in board level drop tests, and resulted in multiple competing failure modes of the MEMS assembly. The identified failure sites include those locations where natural frequencies are close to those of the PWB in the through thickness direction. Examples of such failure sites include wire bonds and MEMS structures. In [108], the high frequency content was quantified for the dynamic response of multi-layer PWBs, caused by secondary impacts. Since the

frequency range was evaluated to be close to the natural frequencies of specific structures in MEMS packages [83]–[86], resonant response of those structures is possible. In SMT assemblies, dynamic behavior at one failure site can be affected by other adjacent failure sites. Such interactions between failure sites are not fully understood in most of the relevant studies ([15], [16], [81]). Therefore, the objective of this study is to investigate the interactive dynamic response that drives two competing failure modes under secondary impacts.

The layout of this paper is as follows: In 6.3.1, the background of board level drop tests with secondary impacts is presented. In 6.3.2, a calibrated finite element analysis (FEA) model is demonstrated to simulate the secondary impact event. Sections 6.3.3-6.3.5 presents a displacement response analysis approach for the system consisting of a PWB assembled with a SMT package and a micro-scale structure inside the package. Real world examples include MEMS microphone components with micro-scale deformable elements such as wire bonds and diaphragm structures. In Sections 6.3.6, a stress estimation methodology is demonstrate based on a quasi-static FEA model for each failure mode. Section 3.1 provides a detailed analysis of acceleration and strain signals associated with various secondary impact test conditions. In Section 6.4.2, a detailed parametric study is carried out, analyzing the displacement response at each failure site while varying the impact acceleration parameters. In Section 6.4.3 and 6.4.4, stress concentration in each failure mode is estimated by comprehensively considering the vertical displacement response of the system, in-plane stretching, and bending strain of the PWB. The results demonstrate influences of secondary impacts

on the two failure modes using qualitative comparisons. These influences provide some further insights to interpret the experimental evidence.

6.3. *Problem Statement and Approach*

In this section, background and an overview of the approach used in this study are introduced. Then a series of analytical and finite element (FE) models are presented to analyze the dynamic response of the SMT assembly are presented. Finally, relevant stress estimation methods for relevant failure modes are described.

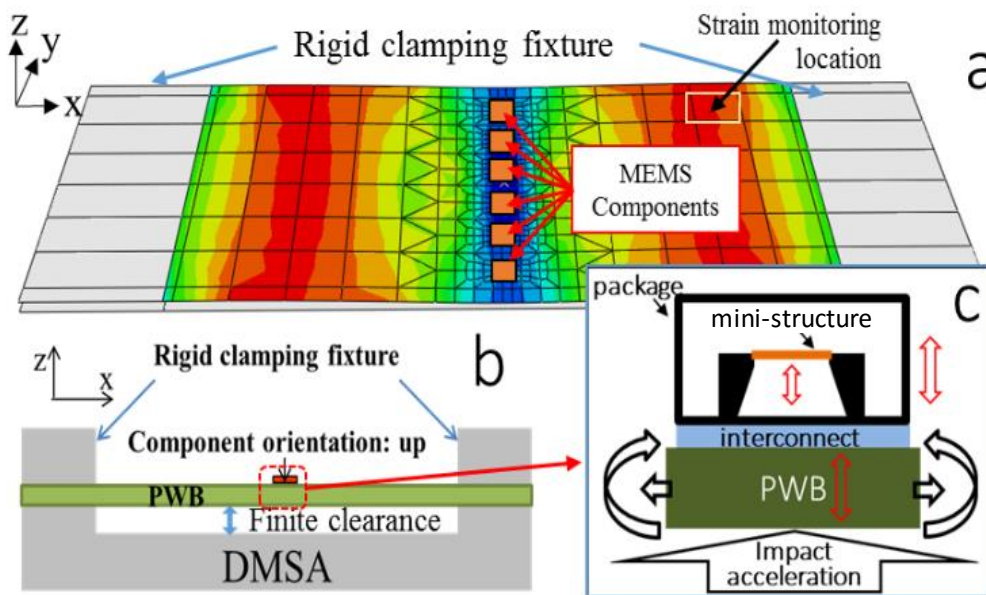


Figure 42: Background a) Secondary impact FEA model; b) Schematic of Test Setup; c) Simplified SMT Assembly and Its Loading Conditions

6.3.1. Background and Approach

In [6], board level drop tests were conducted on a commercially available drop tower equipped with a mechanical acceleration amplifier termed DMSA (Dual Mass Shock Amplifier). This drop setup was used to provide highly repeatable impact acceleration pulses with a width of 0.05 milliseconds and a magnitude of 20,000 g.

PWA test specimens were mounted on specially designed fixtures with finite clearance between them to generate secondary impacts between the PWB and the fixture during drop events. Six MEMS microphone components are assembled on each PWA test specimen. In this study, drop tests were conducted with MEMS components oriented either upwards or downwards. Trenches were added on the top surface of the fixture to prevent direct impacts on the MEMS components when they are facing downwards. As a result, secondary impacts occurred adjacent to the footprints of the SMT packages.

Secondary impacts on PWAs containing SMT assemblies have several effects on the dynamic response of the SMT assembly. These effects include high frequency (hundreds of kHz) through-thickness ‘breathing’ oscillations in the PWB and impact acceleration [108]. When an impact pulse with acceleration of such high frequency and amplitude is applied to the SMT substrate, resonant vibration is excited in the miniature structures within the SMT package. A systematic dynamic analysis approach is developed to investigate the interactive response of the SMT assembly when subjected to such secondary impacts.

Schematics of the experimental setup and the FEA model for the secondary impact test configuration are presented in Figure 42-b and Figure 42-a, respectively (both were discussed in [103]). The transient dynamic FEA model is used to obtain local strain and acceleration signals at the impact site. In Figure 42-c, a simplified side-view of a representative SMT assembly is shown. Three inputs are experienced by the SMT representation: (1) inertia force due to impact acceleration (2) stretching of the PWB, and (3) bending of the PWB. Then, using a frequency domain analysis

approach [108] and a 2-degree of freedom (2-DOF) dynamic analysis approach, vertical displacement responses of three moving parts are analyzed: the micro-scale deformable structure, the package and the PWB itself. Finally, the PWB strain histories and the displacement histories of the three moving parts are further utilized to evaluate the stress concentrations in both failure modes via quasi-static FEA models. Detailed descriptions of the quasi-static FEA models are to be presented later in Section 6.3.6.

6.3.2. Secondary Impact Model Calibration

Acceleration histories at the secondary impact site are very difficult to measure directly because they have extremely high amplitudes with extremely short durations. Therefore, a carefully calibrated transient dynamic FEA model is developed, as shown in Figure 42-a, to provide semi-quantitative insights, as a proxy for actual measurements. The vertical acceleration history during the drop test, measured on the fixture at the PWA edge, is applied to the clamped edge of the PWA model in the drop simulation, as a boundary condition (referred as the “input-g” method [20]). The PWB is modeled with orthotropic, shear-deformable, shell elements, and is located a finite distance above the base fixture plate, which is modeled as a rigid body. Additional elements are attached to the PWB’s top surface, as a simplified representation of the SMT MEMS components, to account for the local stiffening, addition of local mass, and local change in the neutral surface.

Vibration damping and contact parameters are systematically determined from the dynamic strain histories recorded during two drop tests: one without secondary

impact ('infinite clearance' test) and one with secondary impact ('finite clearance' test). The Rayleigh damping coefficients, α and β , representing non-conservative energy dissipation, are iteratively estimated by fitting the model predictions to the strain history measured in the infinite clearance drop test, as shown in Figure 43-a.

Next, the contact between the PWB and the metal fixture base during the secondary impact is modeled as a soft contact, using the penalty method in the FEA dynamic model [114]. A non-linear contact stiffness for the pressure-overclosure correlation [114] is estimated using the Young's modulus and surface roughness magnitude, obtained from indentation tests and profilometry using a nano-indentor tester. Finally, the critical damping fraction is iteratively estimated by matching the simulation results to the strain output from a drop test with secondary impact, as shown in Figure 43-b.

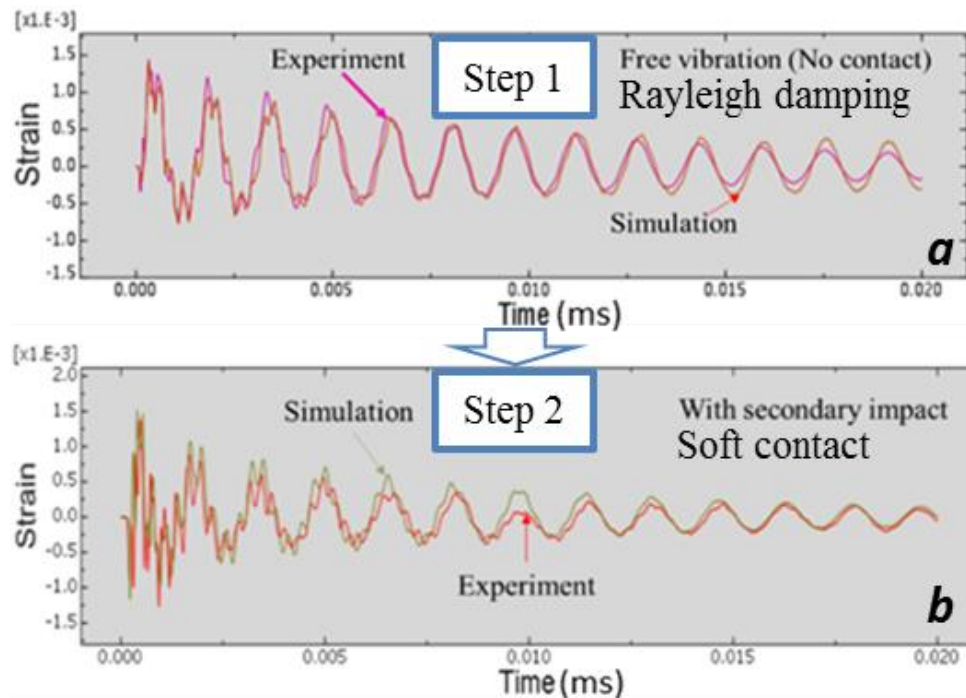


Figure 43: 2-Step Calibration Procedure and Results, PWB Strain

6.3.3. PWB Through-Thickness Resonance

When the PWB is an acceleration pulse caused by a secondary impact, its response acceleration spectrum at the opposite surface contains high frequency contributions at the natural frequency of through-thickness ‘breathing’ mode of vibration. The problem is approximated as a 1-D wave propagation, in order to obtain preliminary insights. Thus, a compound 1-D rod approximation [108] is used to quantify such high frequency oscillation contents in typical laminated PWB structures. As shown in Figure 44-a, one side of the 1-D rod (representing the “PWB bottom” surface) is subjected to a sharp impact pulse, while a SMT package is located at the other end of the rod (representing the “PWB top” surface). The natural frequencies and transfer functions vary with the number of layers of the laminated PWB [108]. The amplitude ratio between the maximum magnitude of transient high frequency response oscillation, $A(f_p)$, and the magnitude of the input signal pulse A_0 is defined as γ (illustrated in Figure 44-b). The minimal time delay between the two peaks is equal to the wave’s transit time from the impact surface to the opposite surface. Since the wave’s transit time through the PWB thickness is much shorter than duration of the impact acceleration, the peak of the response signal in Figure 44-b appears almost simultaneously with the peak of the input signal.

Using the frequency domain analysis approach in [108], $A(f_p)$ of an assumed acceleration pulse $a(t)$ can be obtained in the following procedure. First, a half-sine impact acceleration pulse $a(t)$ with pulse width of t_p and magnitude of A_0 is generated.

The spectrum of $a(t)$ is defined as $|X_{impact}(\omega)|$. The response spectrum, $|Y_{pwb}(\omega)|$, can be computed by multiplying $|X_{impact}(\omega)|$ with the PWB's transfer function, $H_{pwb}(\omega)$. Then, the coordinate of the peak response, (f_p, A_p) , can be identified from $|Y_{pwb}(\omega)|$. Finally, following the magnitude estimation approach in [108], $A(f_p)$ is evaluated as:

$$A(f_p) = \frac{A_p(f_p)\zeta 2\pi f_p \Delta}{1 - e^{-\zeta 2\pi f_p \Delta}} \quad (15)$$

where ζ is the damping ratio, f_p is the resonant frequency for through-thickness 'breathing' mode of vibration of the PWB. Δ is the total duration of the time domain signal $a(t)$. Figure 44-c shows the γ history for a 3-layer PWB using a half-sine shaped $a(t)$ [113] while t_p varies from 10^{-7} to 10^{-4} seconds. γ is observed to reach its peak at a magnitude of 2 when t_p is equal to $2 \cdot 10^{-6}$ s. A linear (dashed line) and piecewise power-law (solid line) approximations are obtained (shown in Figure 44-d) by considering the γ plots for all five laminated PWBs.

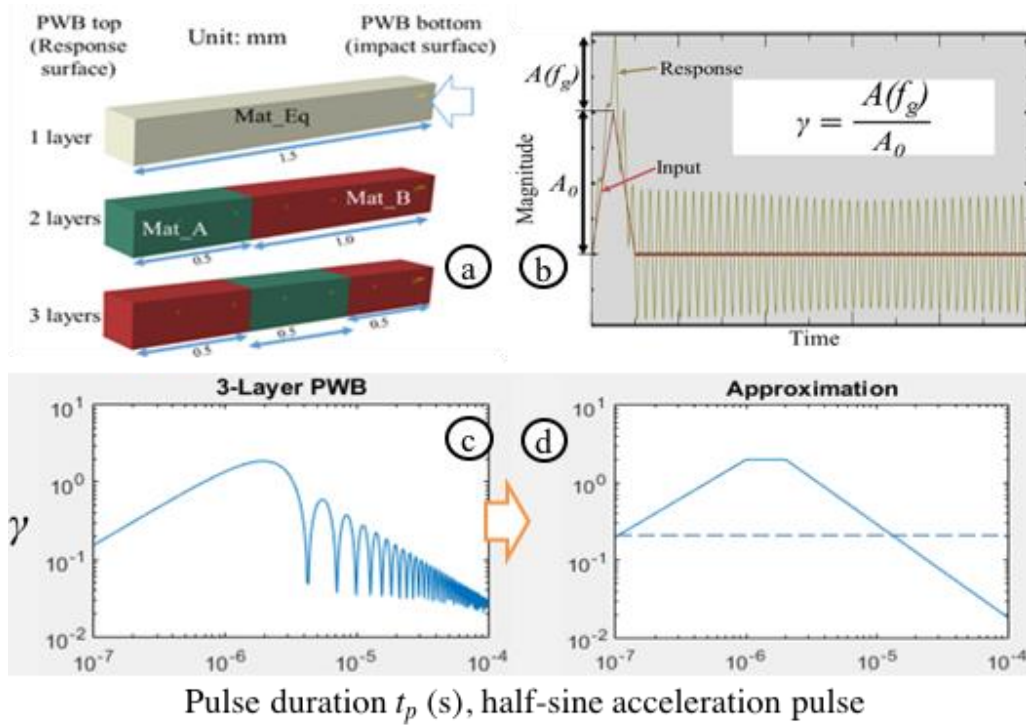


Figure 44: High Frequency Through-Thickness Response of Laminated PWBs to Secondary Impacts

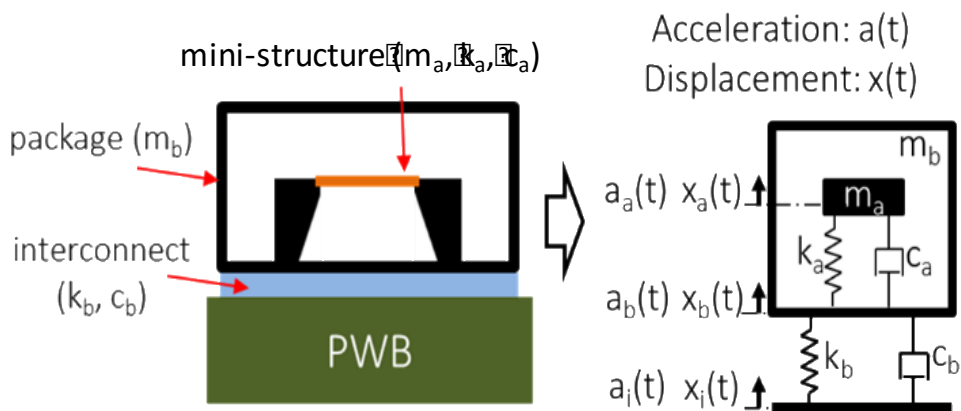


Figure 45: 2-DOF Analytic Model with Two Competing Failure Modes

6.3.4. A 2-DOF Model for Two Typical Failure Sites of SMT

A simplified 2-DOF lumped-parameter representation for the SMT assembly, consisting of the interconnect and an SMT component with internal miniature structures, is developed for quick parametric sensitivity studies. The two representative failure sites are: (i) the surface mount interconnect between the component and the PWB; and (ii) a miniature internal structure (representing a typical internal structural element within the SMT component, e.g. wire bond or MEMS elements). The goal here is to provide semi-quantitative insights into the interactions between these two relevant failure modes, as demonstrated in Figure 45.

Failure Mode-a (FM-a) represents fracture of miniature internal structures in a component. The resonant frequency for typical structures of this kind ranges from tens of kHz to MHz [83]–[86]. Failure Mode-b (FM-b) denotes fracture in the interconnect material between the package and the PWB’s top surface. In this study we will be interested in the changes in the dynamic response at the failure sites for these two failure modes.

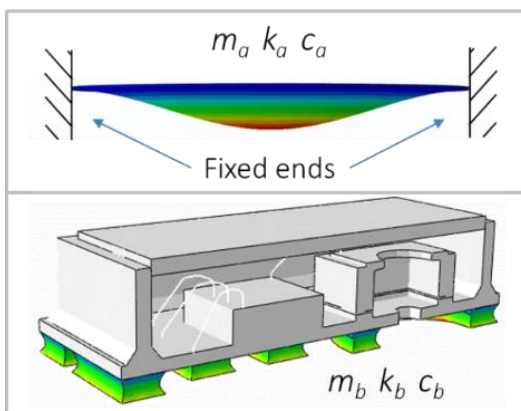


Figure 46: Parameter Extraction for Analytic 2 DoF Model from FEA Model of a MEMS Component

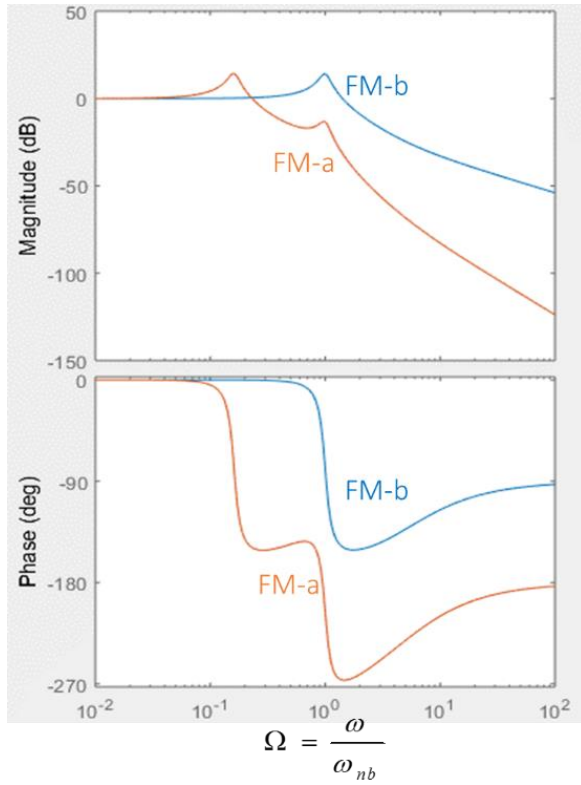


Figure 47: Transfer Functions of the 2-DoF Model

According to Figure 45, when an input excitation $a_i(t)$ is applied to the base, the dynamic response of both the package (m_b) and the micro-scale structure (m_a) within the component can be derived by solving the 2-DOF system. Furthermore, by taking the relative displacement history $x_1(t)=x_a(t)-x_b(t)$, the deflection history of the micro-scale structure with respect to its substrate can be obtained. Similarly, $x_2(t)=x_b(t)-x_i(t)$ is equivalent to the vertical deformation history of the interconnect material.

Table 14: Parameters of the 2-DOF Model

	FM-a	FM-b
E (GPa)	112.4	47.0

ν	0.28	0.35
$\rho(\text{kg/m}^3)$	2329	7330
$k(\text{N/m})$	4.75E+04	3.40E+09
$m(\text{mg})$	5.13E-3	9.53
ω (rad/s)	3.04E+06	1.89E+07
$\omega/2\pi$ (Hz)	4.84E+05	3.01E+06
m_r	0.00054	
ω_r	0.16	

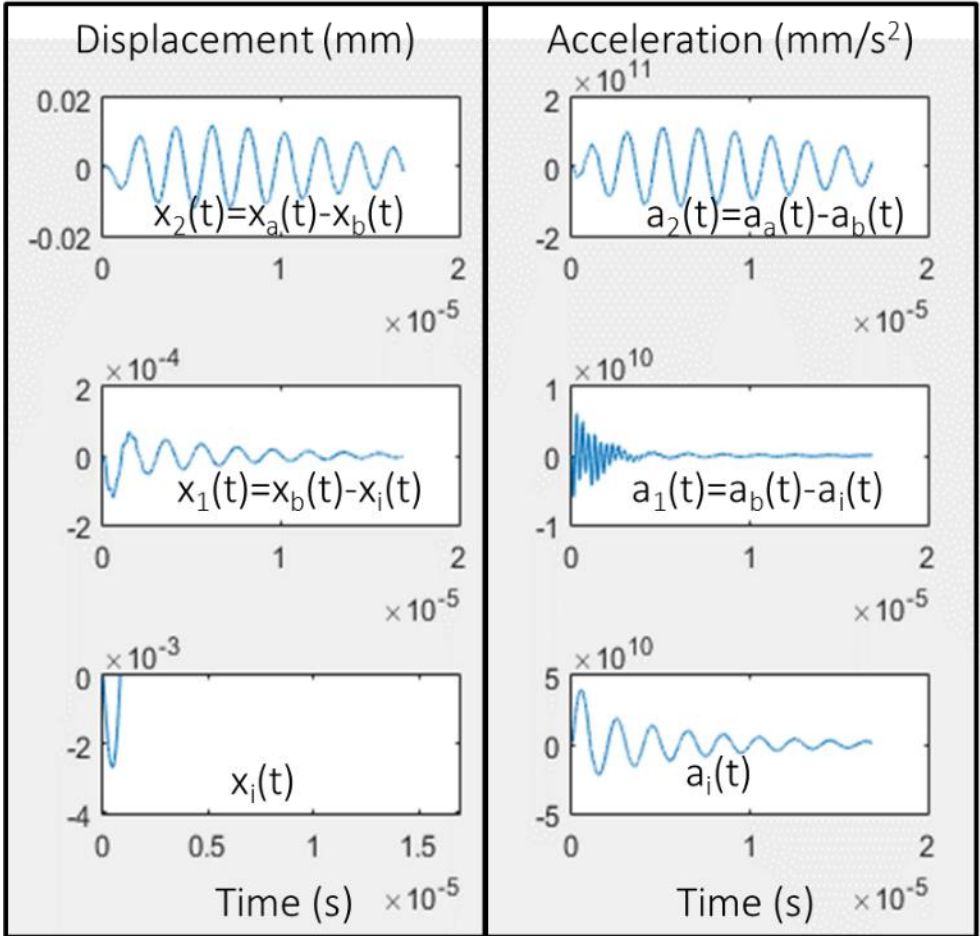


Figure 48: Sample Outputs from the 2-DOF Model, 1.2 mm Clearance, No trench, $\zeta_i = \zeta_a = \zeta_b = 0.05$, $f_p = 0.5\text{MHz}$

The physical parameters of the 2-DOF model are obtained from the MEMS microphone component used in prior studies [103]. For illustration purpose, the real-scenario conditions are simplified by neglecting the following features in the 2-DOF model: i) material plasticity, inhomogeneity and anisotropy; ii) pre-stress in the microscale structure; iii) geometric imperfections; and iv) influence of the 2-DOF system on the base excitation. Also, the geometry of the internal micro-scale structure is selected to match its primary natural frequency with typical values encountered in

MEMS structures. By conducting virtual material-level tests in FEA, as shown in Figure 46, the equivalent dynamic parameters used in the 2-DOF model are obtained. As summarized in Table 14, k is the stiffness, m is the mass, ω is the angular natural frequency, E is the modulus of elasticity, ν is Poisson's ratio, and ρ is density. Subscripts a , b and r denotes the corresponding parameters of FM-a, FM-b, and the ratio between FM-a and FM-b. Nondimensional parameters are defined as follows:

$$\begin{aligned}\omega_r &= \frac{\omega_a}{\omega_b} = \frac{k_r}{\sqrt{m_r}}, k_r = \frac{k_a}{k_b}, m_r = \frac{m_a}{m_b}, \\ \zeta_a &= \frac{c_a}{2m_a\omega_a}, \zeta_b = \frac{c_b}{2m_b\omega_b}\end{aligned}\tag{16}$$

6.3.5. Solutions of the 2-DOF Analytical Model

The linear 2-DOF system under a transient base excitation is solved using standard Laplace transform procedure in the frequency domain [113], and finally, the response is transformed back to the time domain by conducting inverse Laplace transform.

Using the nondimensional quantities defined in Equation (16), the governing differential equation for the 2-DOF system in Figure 45 can be obtained as:

$$\begin{aligned}\frac{d^2x_a}{d\tau^2} + 2\zeta_a\omega_r \frac{dx_a}{d\tau} + \omega_r^2 x_a - 2\zeta_a\omega_r \frac{dx_b}{d\tau} - \omega_r^2 x_b &= 0 \\ \frac{d^2x_b}{d\tau^2} + (2\zeta_b + 2\zeta_a m_r \omega_r) \frac{dx_b}{d\tau} + (1 + m_r \omega_r^2) x_b \\ - 2\zeta_a m_r \omega_r \frac{dx_a}{d\tau} - m_r \omega_r^2 x_a - 2\zeta_b \frac{dx_b}{d\tau} - x_b &= 0\end{aligned}\tag{17}$$

Then, taking the Laplace transform of Equation (17), $X_a(s)$ and $X_b(s)$ can be identified [113], where $X_a(s)$, $X_b(s)$, $X_i(s)$ are the Laplace transforms of $x_a(\tau)$, $x_b(\tau)$ and $x_i(\tau)$ respectively, with τ defined as nondimensionalized time $\tau = \omega_{nb}t$. The transfer functions for deformations at the sites of FM-a and FM-b can be obtained by taking the ratios between $X_a(s)$ and $X_i(s)$, $X_b(s)$ and $X_i(s)$, respectively:

$$\begin{aligned}
TF_{ai} &= \frac{X_a(s)}{X_i(s)} = \frac{(2\zeta_b s + 1)(s^2 + 2\zeta_a \omega_r s + \omega_r^2)}{D}, \\
TF_{bi} &= \frac{X_b(s)}{X_i(s)} = \frac{(2\zeta_b s + 1)(2\zeta_a \omega_r s + \omega_r^2)}{D}, \\
D &= s^4 + (2\zeta_b + 2\zeta_a \omega_r m_r + 2\zeta_a \omega_r) s^3 + \\
&(1 + \omega_r^2 m_r + \omega_r^2 + 4\zeta_a \zeta_b \omega_r) s^2 + (2\zeta_a \omega_r + 2\zeta_b \omega_r^2) s + \omega_r^2
\end{aligned} \tag{18}$$

The transfer functions in Equation (18) are plotted in Figure 47. The main outputs of interest from the 2-DOF model are the relative displacements $x_1(t)$ and $x_2(t)$. Since these outputs are independent of initial conditions, all the involved initial values of displacements and velocities are assumed to be zero. A function was programed in Matlab to obtain all the relevant time domain outputs in response to any specified acceleration excitation $a_i(t)$. A sample plot is shown in Figure 48. For visualization, $x_i(t)$ is plotted with a selected initial velocity.

In this study, $a_i(t)$ histories for the 2-DOF model are obtained in two steps. First, the impact acceleration data is obtained from the component's footprint in the PWB-level secondary impact model shown in Figure 42-a. Since the through-thickness 'breathing' deformation mode of the PWB is missing in FEA shell elements, an associated damped sinusoidal oscillation with maximum magnitude of γA_0 (Section 6.3.3) is superimposed to the impact acceleration data, starting at its peak. A damping

ratio ζ_i is defined to describe the decay rate of the PWB ‘breathing’ oscillation after the impact.

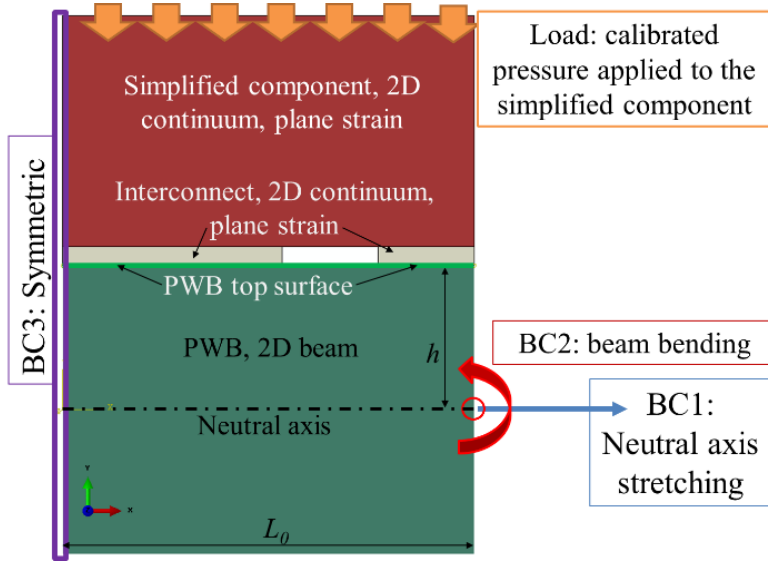


Figure 49: FEA Half-Symmetric Model for FA-b

6.3.6. Stress Estimation for FM-a and FM-b

The stresses are estimated using quasi-static FEA models at the sites of both FM-a and FM-b. There are two sets of model inputs: PWB flexural strain histories from the calibrated secondary impact FEA model, and relative displacements from the 2-DOF model. The quasi-static FEA models are shown in Figure 49 for FM-b and in Figure 51 for FM-a.

In the 2D FM-b FEA model demonstrated in Figure 49, the SMT component is represented with a simplified monolithic mass that is attached to the PWB via interconnect materials. The length of the PWB (modeled with beam elements) is L_0 and the distance between the PWB top surface and the neutral axis is h . The vertical

deformation history of the interconnect material, obtained from the 2-DOF analytic model, is simulated by adding a calibrated pressure to the top of the component.

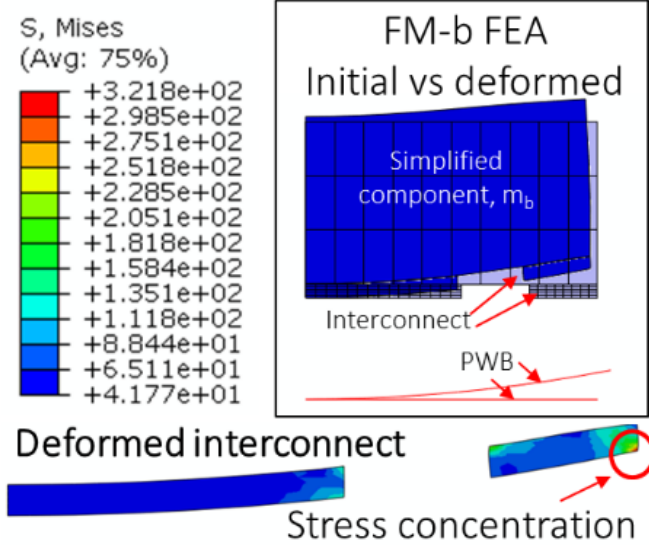


Figure 50: Sample Contour Plot for FM-b

In addition to the vertical motion of the system, the contribution from PWB bending and stretching to the stress field of the interconnect material is also considered. To control the deformation of the PWB, rotation and horizontal displacement boundary conditions are simultaneously applied to the right-end node of the PWB. From the secondary impact simulation, both top-surface and neutral-plane PWB strain can be obtained, denoted as ε_T and ε_m , respectively. $L_0\varepsilon_m$ is directly used as the horizontal stretching magnitude of the neutral axis of the PWB. The rotation at each node of the PWB elements φ is calculated from ε_T , ε_m , L_0 and h , using the following equation:

$$\varphi = \frac{L_0(1 + \varepsilon_m)(\varepsilon_m - \varepsilon_T)}{h(1 + \varepsilon_T)} \quad (19)$$

From the FM-b model, both von Mises stress σ_{eq} and hydrostatic stress σ_m are evaluated for each set of inputs: $x_I(t)$, φ and $L_0\varepsilon_m$. A sample contour plot of von Mises' stress in the FM-b model is shown in Figure 50.

Fatigue life of some alloys are dependent on hydrostatic stress [62], [68] because damage accumulation mechanisms can be inhibited by compressive hydrostatic stress and facilitated by tensile hydrostatic stress. Considering the contributions of both σ_{eq} and σ_m to the fatigue life of the interconnect material, a stress index, σ_b , is proposed based on the assumption that when the magnitude of compressive hydrostatic stress is as high as that of the von Mises stress, no damage will be accumulated:

$$\sigma_b = \left(1 + \frac{\sigma_m}{\sigma_{eq}}\right)\sigma_{eq} \quad (20)$$

Stress estimation for FM-a is relatively straightforward. Since the substrates of micro-scale structures in the SMT components are stiff compared to the structure itself, they are rarely affected by the bending behavior of the PWB in second level packaging. Therefore, stress concentration in FM-a is only dependent on x_2 . Figure 51 schematically illustrates the approximations required to derive lumped parameters of the FM-a model. Similar to the “beam to spring-mass analogy” discussed by Wong [121], $x_2(t)$ from the spring-mass equivalence is identical to the deflection of nodes P_{fm-a} , which is a set of nodes a fixed distance from the center. Based on the FEA, maximum principal stress in FM-a is linearly dependent on x_2 :

$$\sigma_{\max.p} = 1.04e5 \cdot x_2 \quad (21)$$

where the maximum principal stress $\sigma_{max,p}$ is in unit of MPa, deflection x_2 is in unit of mm.

6.4. Results and Discussions

In this section, dynamic signals from the secondary impact FEA model are first computed for different test conditions and compared. Then, displacement responses at sites of FM-a and FM-b are parametrically studied with respect to pulse width and oscillation frequency of $a_i(t)$. Finally, a qualitative comparison is conducted to investigate the role of secondary impact in terms of failure risks of competing failure modes, followed by a qualitative experimental verification of the major conclusions.

6.4.1. Secondary Impact Model Outputs

The dynamic signals are extracted and compared to show how the secondary impact and its geometric constraints (such as clearance and trench) can affect acceleration and strain histories of the PWB.

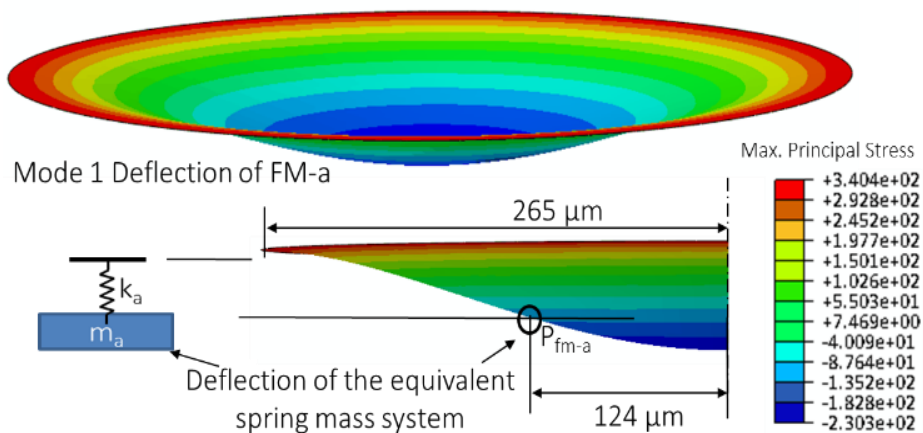


Figure 51: FEA Model for FA-a

In Figure 52, the acceleration histories are plotted from six test conditions with finite clearance, all without the trench on the substrate. At each test condition, acceleration

history from the PWB underneath each component is extracted. The observed acceleration magnitudes from secondary impacts are about 50 to 113 times higher than that of the acceleration input measured from the drop tower. At the same time, the widths of the resulting acceleration pulses are up to 47 times narrower than that of the acceleration input. By contrast, at the infinite clearance condition (no secondary impact), acceleration magnitude peaks at 12,000g (lower than the boundary).

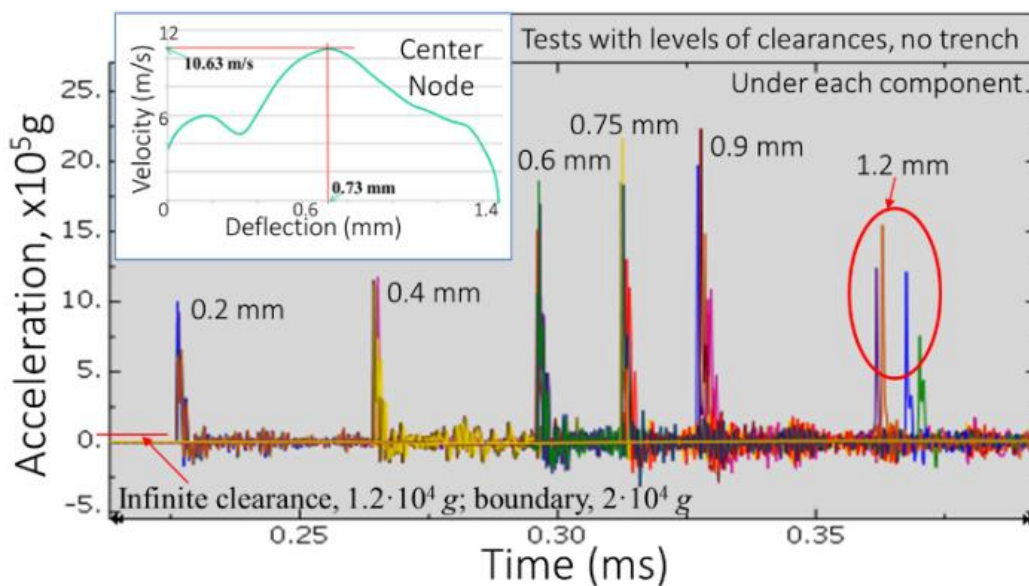


Figure 52: Impact Acceleration Histories at the Footprints of SMT Packages, for Various Clearances

As the clearance increases, the variation of peak acceleration is non-monotonic, accelerations with the highest amplitudes occur between clearances of 0.6 mm and 0.9 mm. This is partially due to the variation of impact velocities of the PWB prior to the impact: when clearances are between 0.6 and 0.9, the impact velocities are at least 50% higher than 0.2, 0.4 and 1.2 mm of clearances.

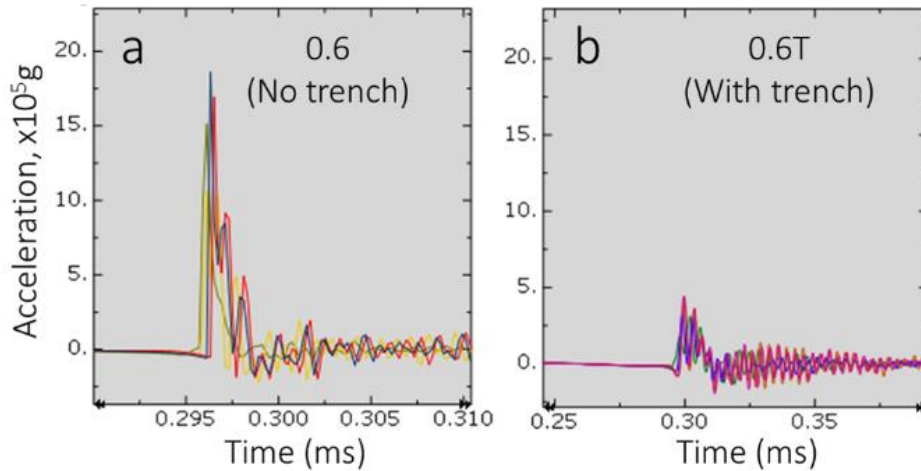


Figure 53: Acceleration from Direct (No Trench) and Indirect (With Trench) Impacts for 0.6 mm Clearance

When a trench is present on the fixture base plate, the impact site on the PWB is not directly underneath the component, but rather, beside the component footprint. This situation is termed ‘indirect impact’ in this study. In contrast, the absence of a trench can cause the impact site to be immediately underneath the component (when PWB fundamental mode dominates the dynamic deformation history). This case is termed ‘direct impact’ in this study. The acceleration history for these two cases is compared for 0.6 mm clearance in Figure 53. The peak acceleration for direct impact is 5 times that under indirect impact. Furthermore, high frequency vibration (bending) of PWB might be excited under indirect impact (in the presence of the trench).

Contact stiffness also plays an important role in determining both the width and magnitude of the acceleration pulse. When the contact stiffness is decreased by a factor of 50, with 0.6 mm clearance, the pulse peak magnitude becomes 13 times lower and the pulse width is 9 times higher.

In terms of strain, the magnitude increases with the increase of clearance at both top-surface and mid-plane. The difference made by the trench is negligible, except during the impact: Then the trench allows for a sudden concavity at the PWB's top surface and for a sudden stretching at the mid-plane.

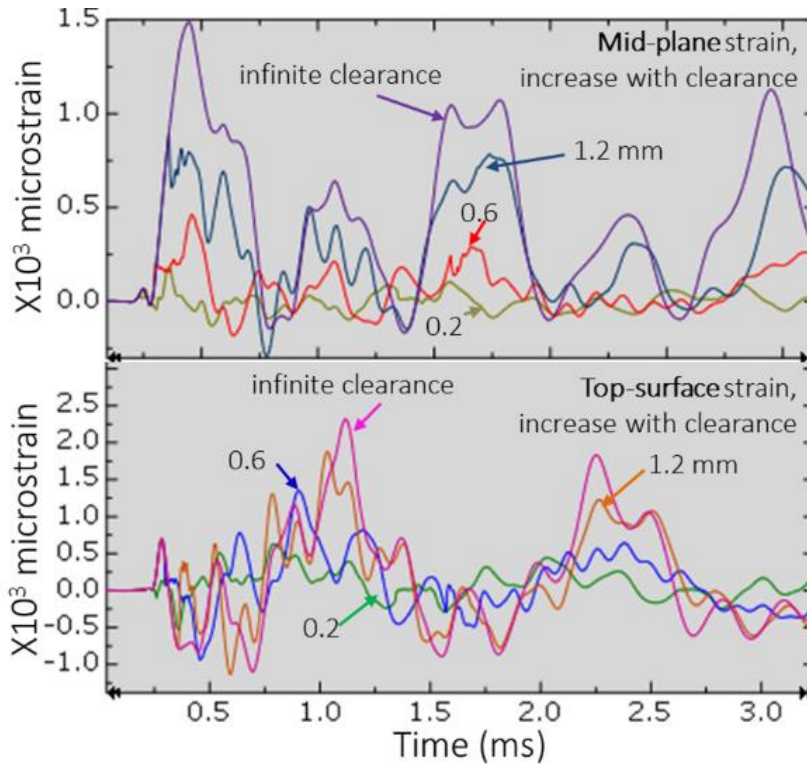


Figure 54: PWB Strain underneath the Components

Based on the secondary impact FEA outputs, data to be further analyzed is summarized in Table 15 for the following test conditions (in sequence): 0.2, 0.6 and 1.2 mm clearance with no trench; maximum concave (Inf1) and convex (Inf2) bending in infinite clearance condition; 0.6 mm clearance with trench; and 0.6 mm clearance with 50 times softer contact and with no trench.

6.4.2. Responses of FM-a and FM-b to Input Accelerations

Responses at sites of FM-a and FM-b to a base excitation $a_i(t)$ are expected to be different due to the differences in the natural frequencies. To explore such differences, an acceleration base excitation is defined in the following form:

$$\begin{aligned}
 a_i(t) = & A_0 \sin(\pi t_p^{-1} t) [u(t) - u(t - t_p)] \\
 & + \gamma A_0 \sin(\pi t_p^{-1} t - t_p / 2 + 1 / 4 f_p^{-1}) \cdot \\
 & u(t - t_p / 2 + 1 / 4 f_p^{-1}) \exp[-\zeta_i \pi f_p^{-1} (t - t_p / 2 + 1 / 4 f_p^{-1})] \quad (22)
 \end{aligned}$$

f_p is the natural frequency of the PWB's through-thickness 'breathing' mode and is excited by the impact acceleration of pulse width t_p , at the bottom surface of the PWB. γ is the amplitude ratio defined earlier, approximated either as a constant $\gamma=0.2$ or as a piecewise power-law representation (Figure 44-d). Equation (22) is capable of representing the high frequency 'breathing' vibration of PWBs in addition to the initial impact acceleration pulse at the contact surface. The small phase difference between the maximum amplitude of 'breathing' mode of vibration and the peak of the half-sine pulse is neglected. f_p was varied within the range $[2 \cdot 10^5 \text{Hz}, 8 \cdot 10^5 \text{Hz}]$ [108] and t_p within the range $[10^{-7} \text{s}, 10^{-4} \text{s}]$. The displacement magnitudes are plotted in Figure 55, assuming $\zeta_i=0.01$. All the displacement magnitudes presented in Figure 55 are normalized by the corresponding displacements at a fixed acceleration condition ($t_p=1.5 \cdot 10^{-5} \text{s}, \gamma=0$).

When $\gamma=0.2$, the displacement magnitudes at sites of FM-a and FM-b are observed to have their own resonance at a critical pulse width ($t_p=1.4 \cdot 10^{-6} \text{s}$ for FM-a, $t_p=2.5 \cdot 10^{-7} \text{s}$ for FM-b), and both yield an amplification of two. When γ follows the piecewise power-law, the displacement magnitude become more dependent on t_p with increase

in γ and reaches a peak amplification of four for both failure modes. In the selected range of high frequency ‘breathing’ vibration, deformation at site of FM-a is more sensitive than that at site of FM-b to pulse parameters, because FM-a’s natural frequency is within the selected frequency range. In an ideal case of zero damping, the combined contribution from t_p and f_p lead to amplification factors as high as 60, in the displacement response at site of FM-a, whereas the maximum amplification for FM-b is only around 4.

Table 15: Outputs from the Secondary Impact Model

Raw data\clearance	0.2	0.6	1.2	Inf1	Inf2	0.6T	0.6 soft
Acceleration pulse							
A_0 (1,000g)	924	1686	1382	12	-12	385	125
t_p (1e-6s)	1.25	1.30	1.06	170.00	170.00	2.74	11.83
PWB Strain							
During impact							
ϵ_m ($\mu\epsilon$)	22	80	800	1480	485	600	120
ϕ (1e-3 radian)	-0.02	-0.86	3.73	6.63	-5.21	4.87	-0.60
Max. bending							
ϵ_m ($\mu\epsilon$)	-92	-56	210	1480	485	-13	-90
ϕ (1e-3 radian)	-2.07	-4.02	-4.77	6.63	-5.21	-4.21	-2.90

Based on the insights gained from Figure 55 and the extracted acceleration profiles obtained in Table 15, the magnitudes of $x_1(t)$ and $x_2(t)$ are computed for each test condition, as summarized in Table 16. Under any clearance, displacement of FM-b is two orders of magnitude lower than FM-a. It is also noticed that secondary impact can significantly amplify the displacement response at both failure sites.

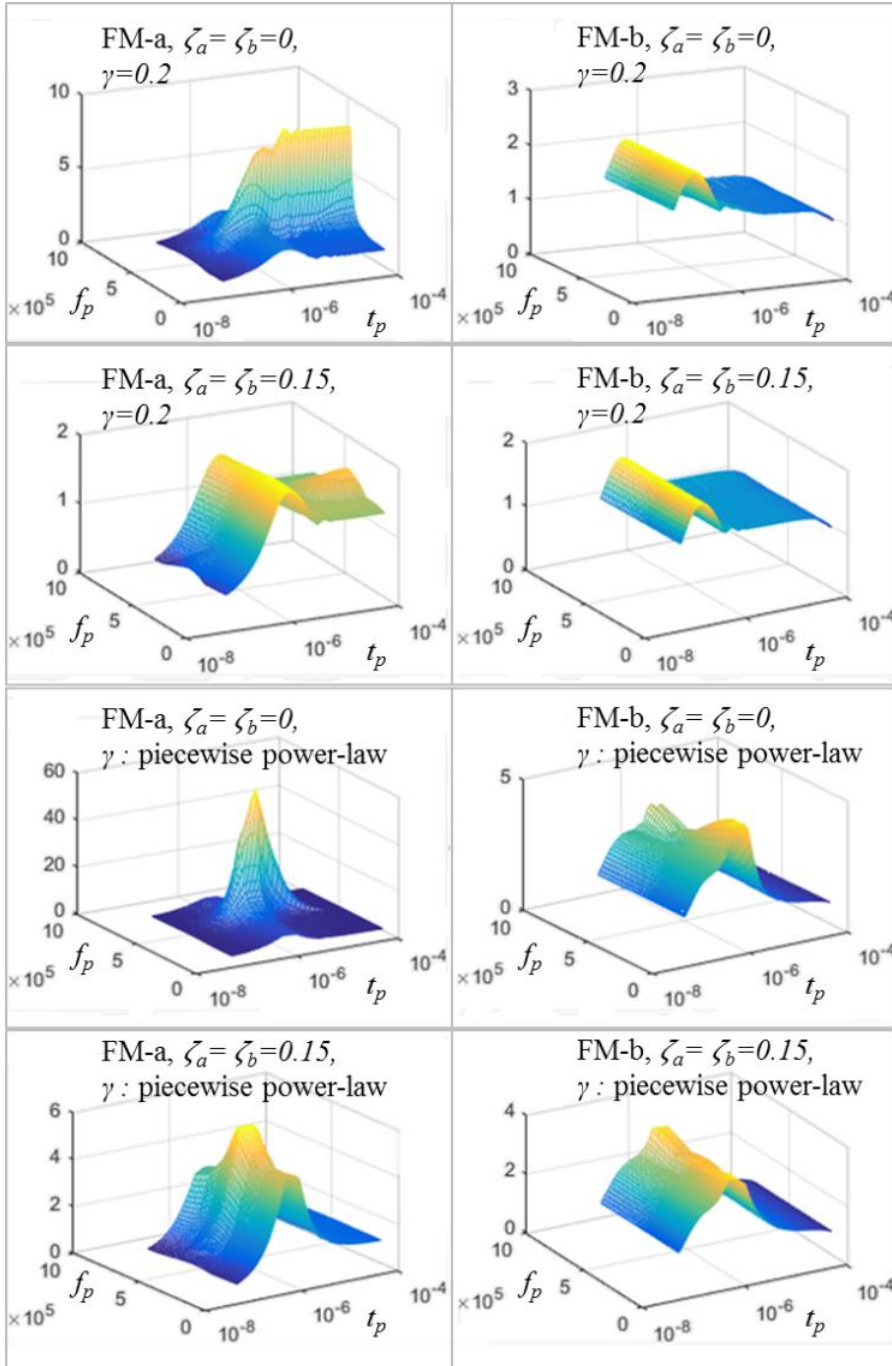


Figure 55: Amplifications of x_1 and x_2 for Impact Pulses with Various t_p and f_p Pulses, Based on Two Approximation of γ

Table 16: Outputs from the 2-DOF Model

Raw data\clearance	0.2	0.6	1.2	Inf1	Inf2	0.6T	0.6 soft	
(μm)	FM-a, x_2	8.0E+00	1.5E+01	1.2E+01	1.3E-02	-1.3E-02	8.3E-01	2.0E-01
	FM-b, x_1	7.9E-02	1.4E-01	1.2E-01	1.3E-04	-1.3E-04	1.3E-02	4.3E-03

6.4.3. The Sensitivity of each Failure Site to Secondary Impacts

The selected test conditions in Table 15 and Table 16 allow for four comparisons about secondary impacts. Such comparisons are expected to semi-quantitatively show the effect of various types of secondary impacts on the resulting stress concentrations at the failure site of each failure mode. Utilizing the stress estimation approach discussed in Section 6.3.6, stresses are computed and summarized in Table 17.

The results are obtained with assuming the following assumed constants: $\zeta_i = \zeta_a = \zeta_b = 0.05$, $f_p = 0.5\text{MHz}$. Since there is no secondary impact in the infinite clearance test condition, γ is equal to zero for stress estimations under Inf1, Inf2 and 0.6T test conditions. In addition, the high frequency PWB bending observed in Figure 53.b is considered for 0.6T.

In general, it is observed that under finite clearance test conditions without the trench, very high stress values are estimated for FM-a. Stress values are also rather high for FM-b at the moment of impact due to high compression. However, if the influence of hydrostatic stress on damage accumulation is considered, the stress index σ_b indicates that FM-b failures are still dominated by the maximum bending of the PWB. When a board is tested with infinite clearance, the maximum convex bending of the PWB (Inf2) induces a higher stress concentration than the concave shaped half-cycle (Inf1).

Table 17: Stress Estimations for FM-a and FM-b

(MPa)\clearance	0.2	0.6	1.2	Inf1	Inf2	0.6T	0.6 soft
FM-a, $\sigma_{\max,p}$	835	1525	1243	1	1	86	21
FM-b							
During impact							
σ_{eq}	224	341	507	270	447	303	50
σ_m	-133	-205	-297	-152	237	-169	25
σ_b	91	136	210	118	684	135	75
Max. bending							
σ_{eq}	137	283	375	248	446	302	197
σ_m	74	152	200	-140	237	162	106
σ_b	210	434	575	108	683	465	303

The first comparison is conducted between 0.6 and Inf2 to analyze the change in stress concentrations of FM-a and FM-b due to a secondary impact. The comparison is shown in Figure 56.

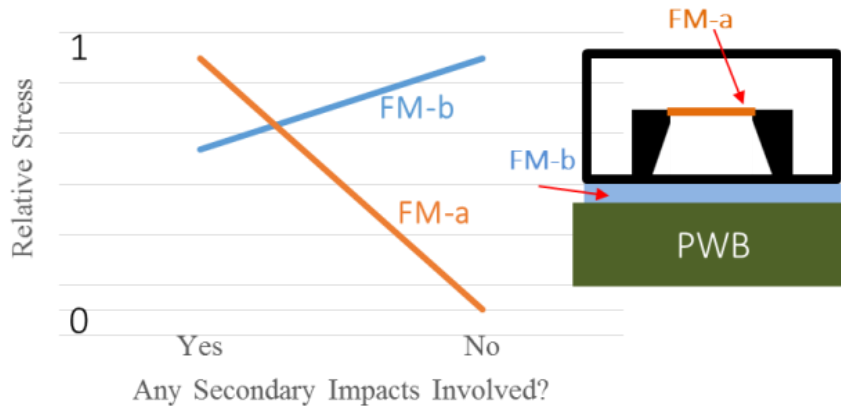


Figure 56: Sensitivity of FM-a and FM-b to Secondary Impacts

FM-a is shown to be more likely than FM-b when secondary impact occurs. The amplification of maximum principal stress can increase up to a thousand times, mainly because the extremely short pulse (10^{-6} s) contains energy in a frequency range which excites the micro-scale structure for FM-a. Also, the natural frequency of FM-a may be near that of the PWB (hundreds of kHz).

On the other hand, less interconnect failures are expected due to secondary impact because the stress index is more dependent on deflection than acceleration of the PWB and the finite clearance would limit the PWB's deflection. The comparison in Figure 56 shows the secondary impact test method can potentially be an accelerated life testing (ALT) method for FM-a type failure modes.

The second comparison is conducted between 0.6 and 0.6T, to analyze the influence of a direct impact versus an indirect impact on the resulting stress levels in each failure mode. The comparison is shown in Figure 57.

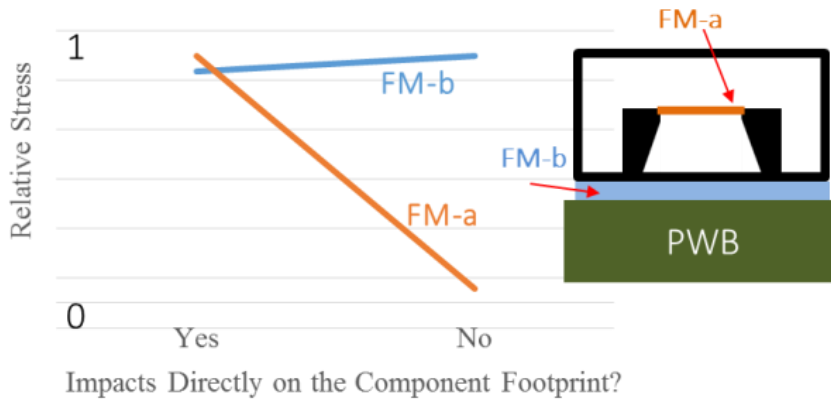


Figure 57: Sensitivity of FM-a and FM-b to Direct and Indirect Impacts

When the secondary impact is not directly applied to the portion of PWB where components are mounted on, stress in the micro-scale structure can be reduced by 90~94%. This is because the acceleration pulse from indirect impact is much lower than that from an impact site. As a result, such an acceleration pulse from indirect impact is less likely to excite high deflections in FM-a. Even though high frequency bending vibration may be induced, the relatively low magnitude makes the

contribution from high frequency bending insignificant. For the interconnect failure mode, no significant difference in stress index is expected.

The third comparison is conducted among three finite clearance cases, 0.2, 0.6, and 1.2 mm, all for direct impact without the trench. This comparison is utilized to demonstrate the effect of the cavity prior to secondary impacts. The result is shown in Figure 58.

The stress in the microscale structure changes non-monotonically with clearance: the peak is reached when the clearance has the highest acceleration or impact velocity (mid cavity) among the three conditions. Whereas for interconnects, stress index is expected to increase as clearance increases because higher deflection and strain magnitudes (Figure 54) are allowed by larger clearances.

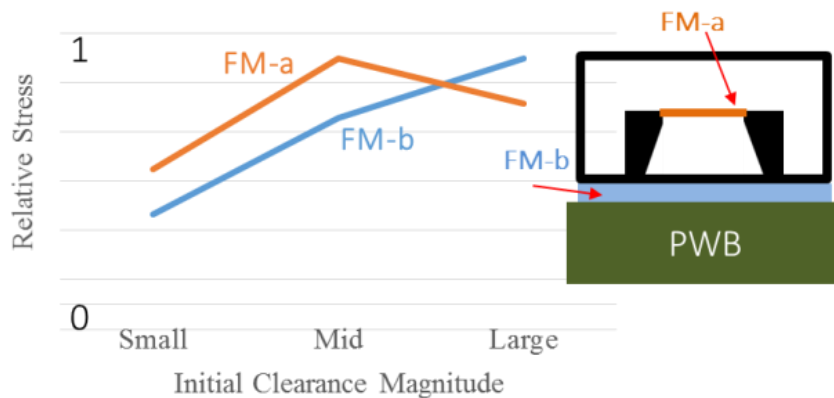


Figure 58: Sensitivity of FM-a and FM-b to Clearance

The fourth comparison is conducted between two contact stiffness cases for 0.6 mm clearance, to study the difference made by the contact stiffness. The result of this comparison is shown as Figure 59.

As the contact stiffness is reduced, stresses at both failure sites become lower, as more kinetic energy is absorbed at the contact site during a softer contact, as discussed below. Stress in the microscale structure modeled within the SMT component shows a higher sensitivity to the contact stiffness than the stress at the interconnect. This is because as contact stiffness varies, the change in magnitude and width (and hence frequency spectrum) of the acceleration pulse has a more direct influence on the dynamic response of the microscale structure than that of the interconnect. When the contact stiffness is increased 50 times, the stress increases up to 73 times at the microscale structure, but only 1.4 times in the interconnect.

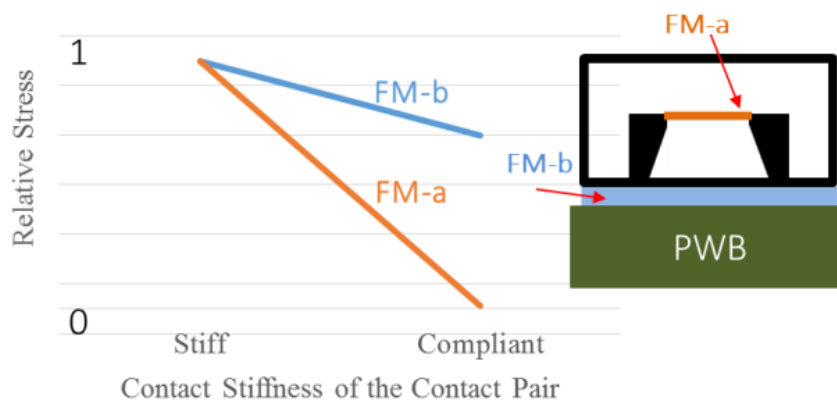


Figure 59: Sensitivity of FM-a and FM-b to Contact Stiffness

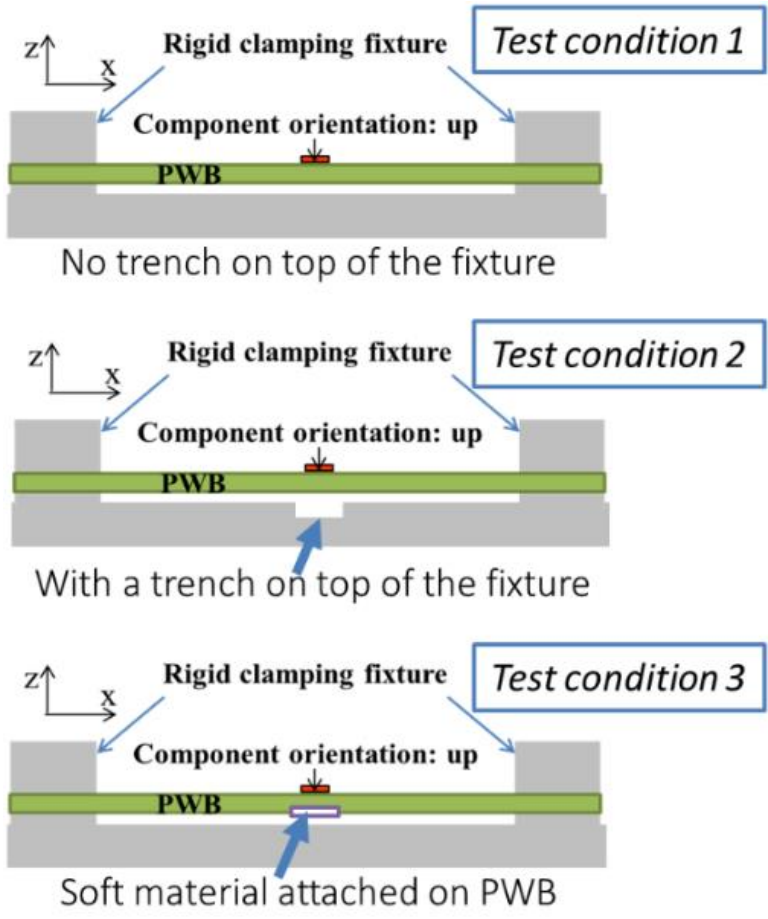


Figure 60: Schematics of the Three Test Conditions

6.4.4. Experiments: Results and Insights

A set of experiments are conducted to further investigate the comparative trends obtained in Section 6.4.3. Three board-level drop test conditions are selected, as demonstrated in Figure 60, and discussed later in this section. The fixture is mounted on DMSA [5] which provides a measured highly repeatable 20,000g acceleration with 0.05 milliseconds of pulse width. All the tests have secondary impacts, with a common finite clearance of 1.0 mm. The selected SMT component is a COTS MEMS microphone. FM-a represents fracture of the MEMS microphone diaphragm, FM-b

represents failure of the solder interconnect under the MEMS component. At least 12 components are tested under each of the three tests conditions discussed below.

As shown in Figure 19, Test condition 1 has direct impact (a flat metal substrate with no trench in the PWB-metal contact pair); Test condition 2 has indirect impact because of a trench provided in the metal substrate; Test condition 3 has a flat contact surface (no trench) as in Test condition 1, but the PWB-metal contact pair is softened by a strip of scotch tape attached to the PWB's bottom surface.

Test results are summarized in Table 18. Weibull characteristic life η , Weibull shape parameter β , and the percentage of FM-a type failure modes for each test condition are listed. In Figure 61, a sample probability density function and optical microscope images of a FM-a type failure taken from failure analysis are presented.

Table 18: Experimental Results

Test condition	Number of Components	η , Weibull	β , Weibull	P% of FM-a
1. No trench, stiff contact	12	4	1.3	100%
2. With trench, stiff contact	18	237	2.8	0%
3. No trench, compliant contact	18	205	1.5	11%

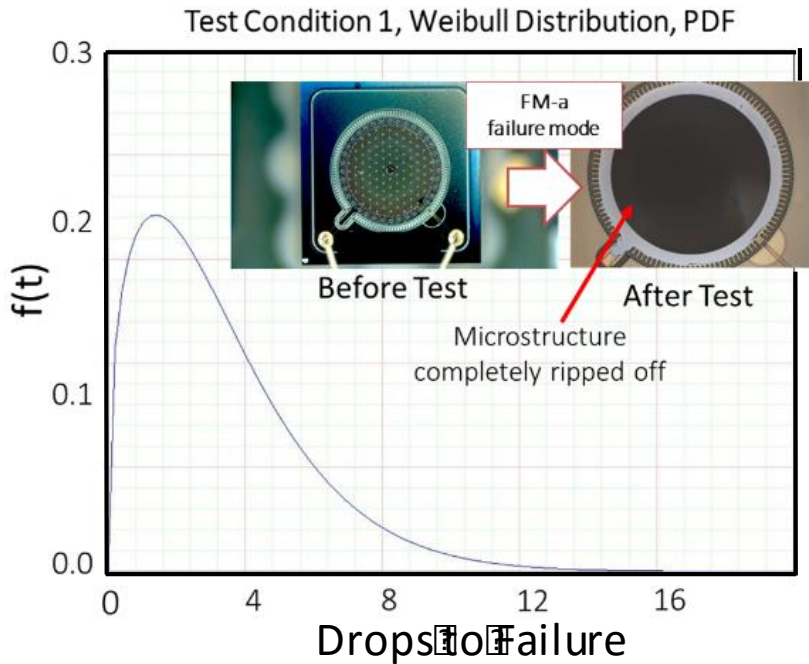


Figure 61: Sample Probability Density Function and Failure Mode

Test condition 1 results in a very short characteristic life of the selected MEMS microphone component. When the secondary impact is not directly on the PWB's bottom surface (Test conditions 2 and 3), the characteristic lives of the components are increased by two orders of magnitude. In terms of failure modes, all the failures in Test condition 1 are FM-a type. However much lower percentages of FM-a type failures are observed in the other two test conditions.

These test results provide evidence that the miniature structures in SMT packages are very sensitive to secondary impacts. When the impact is severe enough for the miniature structure, very early failures are expected. When the severity is decreased by avoiding stiff and direct impacts to the footprints of SMT packages, durability of the components is significantly improved. Along with the increase of the

characteristic life of the MEMS component, a higher percentage of packaging related failure modes (such as interconnects) appears. This trend also exhibits different sensitivities of competing failure modes as the conditions of secondary impact changes, which agrees with a prior experimental study conducted by the authors [6]. In [6], secondary impact tests were conducted at a series of clearances with the trench. Competing failure modes were identified to vary non-monotonically with the clearance. As clearance increases, the FM-b type failures are more dominant than the FM-a type failures.

Even though the analytical approach presented in this paper includes quite a few simplifications such as lumped parameter idealization and linearizing of material behavior and contact properties, the analytical model findings still provide valuable qualitative insights into the influence of secondary impacts on competing failure modes in SMT packages.

6.5. Summary and Conclusion

Secondary impacts on PWAs can result in distinctly different responses of different SMT failure modes with different resonant frequencies. This paper is the second of a two-part sequence addressing issues of secondary impact in PWAs. The first paper in this sequence discussed the generation of high-frequency ‘breathing mode’ of vibration in PWBs due to propagation of contact stresses. This second part focuses on the effect of such ‘breathing modes’ of PWB vibration on the failure modes of SMT components with different resonant frequencies. Different sensitivities of two selected failure modes are evaluated using a systematic dynamic analysis approach, involving 2-DOF analytical lumped-parameter modeling and 3-D transient dynamic FEA for response analysis; and quasi-static FEA for stress analysis.

The displacement magnitudes at the sites of the selected failure modes from secondary impacts depend on the pulse width of the input acceleration and the natural frequency of the ‘breathing’ mode of PWB vibration. Within the pulse width and frequency ranges of interest, displacement responses of miniature structures in SMT packages are up to 15 times more sensitive than that of solder interconnects to the impact acceleration profile.

At the site of secondary impact, acceleration pulse can be up to 113 times higher and 47 times narrower than that of the acceleration input measured from the rigid fixture. The level of amplification is also dependent on various factors such as the clearance of the contact pair and the shape and stiffness of the contact pair. As such factors vary, the amplification of acceleration decreases within an order of magnitude. By

contrast, strain magnitudes of the PWB are generally smaller when secondary impact occurs than when secondary impact is prevented.

Rather high compressive stress in the interconnect materials at the moment of secondary impact is expected. However, if the influence of hydrostatic stresses to fatigue failures is considered, PWB's maximum bending strain could still be the dominating factor leading to interconnect failures. On the other hand, failures in miniature structures are much more vulnerable to secondary impacts. The amplification of maximum principal stress can increase up to a thousand times, mainly because the extremely short pulse width and the resonant oscillation of PWB both contribute to the excitation of resonant vibrations of the miniature structure.

The distinctly different sensitivity of the two failure modes explains why miniature structures are less likely to fail in conventional board level drop test than in tests with secondary impacts. Therefore, the secondary impact method, provides an option of accelerated life testing for miniature structures in SMT packages. More importantly, the results can be utilized for establishing design rules to avoid or alleviate microstructure failures by eliminating or softening the secondary impacts.

Acknowledgements

We wish to acknowledge the members of Center for Advanced Life Cycle Engineering (CALCE) at the University of Maryland for sponsoring this study. We would like to thank Microsoft Mobile (Finland) for the continuous support of this research.

Chapter 7. Discussions and Summary

This dissertation has investigated the effect of secondary impact on board-level-drop durability of PWAs. Common failure modes in surface mount packages (e.g. MEMS) under secondary impacts include not only failure in interconnect materials but also failure of internal miniature structures. In particular, with the change of secondary impact conditions, the participation of multiple competing failure modes were experimentally identified, numerically simulated, and analytically explored. An overall discussion about the outcome of this dissertation is provided in Section 7.1. In Section 7.2, the contributions of the dissertation are highlighted. Finally, the limitations of the current study are listed in Section 7.3.

7.1. Conclusions

Reliability experiments and analysis on a selected COTS MEMS microphone assembly reveal that:

- In board-level-drop tests at 20,000 g, secondary impacts between the test board and fixture significantly amplify the damage of the components up to 84 times, even with a fully supported, tightly clamped PWA. The drop durability of PWAs with MEMS microphone components is observed to decrease by 95% as the clearance between the PWA and the fixture increases from 20% to 120% of the board thickness. At any given clearance, the drop durability of the MEMS PWAs tested with components facing upwards is up to 11 times higher than that of the MEMS PWAs with components facing downwards, depending on the clearance.

- The majority of functional failures in the tested MEMS microphone components are caused by MEMS package related failure modes, including wire bond fracture, solder fracture, and die attach delamination. MEMS package failure modes occur four times more than MEMS device failures. Furthermore, a transition in dominant failure mode (quantified as characteristic life, based on 2-parameter Weibull distribution) is observed as clearance between PWB and the fixture base changes. Participation of multiple PWB bending modes are expected to contribute to the rapid changes in the dominant failure mode.
- A proposed 2-parameter (hydrostatic stress and von Mises' strain) based fatigue damage model for multiple failure sites is capable of describing the effect of competing failure modes. The fatigue damage accumulated during drop tests are captured by combining a hydrostatic stress correction factor and a time domain integration feature, with an equivalent shear stress criterion. Rayleigh damping coefficients defined with nonlinear contact stiffness are useful to simulate the secondary impact event.

Based on a detailed multi-scale dynamic analysis using a simplified model structure that is representative of key dynamic features in of a typical SMT assembly (containing an interconnect and a microscale internal structure), the following insights are gained:

- Amplification of drop severity from secondary impacts are quantified: at the site of secondary impact, impact can increase acceleration by two orders of magnitude and frequency bandwidth by one order of magnitude, with respect

to the rigid fixture. The level of amplification is also dependent on various factors such as the clearance, shape, and stiffness of the contact pair. As such factors are varied, the amplification of acceleration decreases reduces to below one order of magnitude. By contrast, strain magnitudes of the PWB decreased during secondary impact by a flat rigid surface.

- Through-thickness dynamic response: “breathing mode” of the PWB increases the dynamic acceleration of SMT miniature structures by 50x depending on the shape and duration of the impact pulse, the laminated structure of the PWB, and the damping ratios. The magnitude (displacement) of “breathing mode” of the PWB can be up to 4 times that of the input.
- Dynamic response of internal miniature structures in SMT components is shown to be highly sensitive to secondary impacts. The theoretical amplification of maximum principal stress can increase by three orders of magnitude. Theoretical displacement response can be 15x more sensitive than interconnects.

7.2. Contributions

- First detailed study of the role of secondary impact on dynamic PWB response
 - A mechanistic calibration procedure for obtaining non-linear contact properties to improve the precision of secondary impact simulation.
 - Influence of geometry/constraints of the assembly (contact stiffness, trench, and clearance) on accelerations at the impact site.
 - Effect of impact acceleration profile (e.g. shape, magnitude, pulse width) on PWB modes (flexural and “breathing modes”).
- A new study to analyze the sensitivity of competing failure modes in SMT assemblies from secondary impact
 - Effect of “breathing mode” on the resonance of miniature structure failure modes (for example, in MEMS devices).
 - Parametric understanding of the relative importance of PWB post-impact dynamic modes (bending, stretching and “breathing mode”) and inertial force on the dynamic response at competing failure sites (interconnects and miniature structural elements within the component).
- First study to provide fundamental understanding of the role of secondary impacts on dynamic response and damage in SMT PWAs under drop conditions:
 - Dominant sources of stress and competing failure modes
 - Relationship between excitation parameters (clearance) and drop durability.

- First comprehensive study of damage modes in MEMS microphone assemblies during drop tests with secondary impact:
 - Most comprehensive experimental results to date, for drop test durability of MEMS assemblies under various conditions of secondary impact.
 - Most comprehensive documentation of dominant failure modes.
- First mechanism-based drop damage modeling approach that account for drop orientation and post-impact vibration
 - Quantifies the damage accumulation rate for three package related failure modes based on a combination of dynamic stress analysis and test results

The contributions of this dissertation are meant to prove that the secondary impact method provides an option of accelerated life testing for miniature structures in SMT packages. More importantly, the results can be utilized for establishing design rules to avoid or alleviate microstructure failures by eliminating or softening the secondary impacts.

7.3. Limitations & Future Work

There are several limitations in this dissertation that can be addressed in future studies.

- Material property: room temperature mechanical properties of some materials used in MEMS systems are rate-dependent; they should be modeled in drop test simulation
 - Strain rates are expected to be up to $5 \cdot 10^3 \text{s}^{-1}$, for solders, other alloys, and polymers, etc.
 - Solder joints are modeled using Cowper-Symond rate-dependent constitutive law.
 - Other rate-sensitive material behaviors in the assembly are suggested to be modeled.
- Completeness of damage models: the damage modeling in this study focused only on the packaging failure modes in the MEMS assembly.
 - The MEMS device failure modes (e.g fracture of diaphragm, back-plate or runners) would help in forming a more comprehensive damage model.
 - The considerations of strain rate effect, as well as the effect of “breathing mode” would further improve the completeness of the damage models.
- High sampling frequency data acquisition: through thickness oscillations (“breathing mode”) of a 1 mm thick PWB are suggested to be captured
 - Experimentally at more than 1MHz using high resolution vibrometers.

- Numerically with sufficiently small time increments in transient dynamic drop test simulation
- Dynamic interactions: some possible effects are to be verified in board level drop test simulation
 - Compliance of clamping fixture for the PWB due to its finite stiffness, fastening torque, and friction with the PWB.
 - Influence of component response to PWB response
- Accuracy of the dynamic modeling approach can be enhanced by considering additional real-scenario complexities
 - Material plasticity, inhomogeneity, and anisotropy
 - Influence of the 2-DoF system on the base excitation (“breathing mode”)
 - Plastic deformation of the PWB
 - Air pressure (fluid dynamics) between the contact pair
- Some parameter idealizations are suggested to be quantified in FEA
 - Dispersion of stress wave propagation in PWBs
 - Pre-stress in miniature structures induced by the manufacturing process
 - Higher modes and deformation of the lumped parameter representations
 - Experimental verification could be used to further calibrate the idealized parameters used in the 2-DoF model.

- Using S-N curves so that the durability of the SMT assembly are directly related to the analytical response
 - A response sensitivity study based on durability (instead of stress or displacement) further improve the value of this study
 - Different S-N curves are needed to correlated stress and durability of relevant materials

Appendices

A1. MATLAB Code: Amplifications of x_1 and x_2 with Varying t_p and f_p

The function is used to parametrically obtain the displacement magnitudes for FM-a and FM-b with respect to f_p ='freqh' and t_p ='timp'. Outputs of this function are the displacement response of FM-a='d2' and FM-b='d1'

```
function [d1 d2]=f(timp,freqh)

syms s

%% parameters define

k1=3.39770E+06;

k2=4.74943E+01;

m1=9.53000E-09;

m2=5.13000E-12;

wn1=1.88819E+07; %freq1=3MHz

wn2=3.04272E+06; %freq2=0.484MHz

ep1=0.50;

ep2=0.50;

epi=0.01;

%% Conversions to/from Hz and rad/s

Hz2rps=2*pi; rps2Hz=1/2/pi;

% timp=1.5E-5;

% freqh=5E5; % Hz, high frequency oscillation

wnh=freqh*Hz2rps;
```

```

wni=1/2/timp*Hz2rps; %freqimp=0.02MHz

%% direct inputs

kr=k2/k1;

mr=m2/m1;

wr=wn2/wn1;

om0=wni/wn1;

omh=wnh/wn1;

amp=7.47E8; %acceleration peak (m/s^2)

hsr=1; % eith 0 (turn-off the half-sine) or 1 (turn-on
the half-sine)

% hfr=0;

if timp>2e-6;

    hfr=2/(0.000002^(-1.2))*timp.^(-1.2);

elseif timp>1e-6

    hfr=2;

elseif timp>1e-8

    hfr=2e6*timp;

end

%% transfer functions, X3=base, X2=microstructure,
X1=package&solder

% D2 E2 C, non-dimensional

D2(s)=s^4+(2*ep1+2*ep2*wr*mr+2*ep2*wr)*s^3+(1+mr*wr^2+wr^
2+4*ep1*ep2*wr)*s^2+(2*ep2*wr+2*ep1*wr^2)*s+wr^2;

E2(s)=s^2+2*ep2*wr*s+wr^2;

C(s)=2*ep2*wr*s+wr^2;

% X1(s)/X3(s), solder joint & package

X13=(2*ep1*s+1)*E2/D2;

```

```

X13 = collect(X13,s);
[N13,D13] = numden(X13);
nominator13 =sym2poly(N13);
denominator13=sym2poly(D13);
sys13=tf(nominator13, denominator13);
% X2(s)/X3(s), micro-structure
X23=(2*ep1*s+1)*C/D2;
X23 = collect(X23,s);
[N23,D23] = numden(X23);
nominator23 =sym2poly(N23);
denominator23=sym2poly(D23);
sys23=tf(nominator23, denominator23);
%% Input Base excitation
% input signal at x3
taup=0:round(50/om0)/19999:round(50/om0);
tau=taup';
tp=0:round(50/om0)/19999/wn1:round(50/om0)/wn1;
t=tp';
ai=hsr*amp*sin(om0*wn1*t).* (heaviside(t)-heaviside(t-
pi/om0/wn1))+hfr*amp*sin(omh*wn1*(t-
pi/om0/2/wn1+pi/omh/2/wn1)).*heaviside(t-
pi/om0/2/wn1+pi/omh/2/wn1).*exp(-epi*omh*wn1*(t-
pi/om0/2/wn1+pi/omh/2/wn1));
vi=cumtrapz(t,ai);
wi=cumtrapz(t,vi);
% response at mode1(w1) and mode2(w2)
w1=lsim(sys13,wi,tau);

```



```
w2=lsim(sys23,wi,tau);  
d1=max(abs(min(w1-wi)),abs(max(w1-wi)))/1;  
d2=max(abs(min(w2-w1)),abs(max(w2-w1)))/1;
```

A2. MATLAB Code: γ of high frequency acceleration

The function is used to parametrically obtain the amplitude response of PWB top surface when subjected to a half-sine impact acceleration with pulse width 'timp', output of the function is the peak coordinate of the response spectrum [ar,fp]

```
function [ar,fp]=ampf01(timp)

%% Conversions to/from Hz and rad/s

load PWBTF

Hz2rps=2*pi; rps2Hz=1/2/pi;

fs=2e8; %sampling frequency

wni=1/2/timp*Hz2rps; %freqimp=0.02MHz

wnh=5e5; %freqimp=0.02MHz

delta=5e-4; % inspect duration

eta=0.01;

TF=AR_L5p01;

%% direct inputs

amp=1; % 1.50E9; %acceleration peak (m/s^2)

hsr=1; % eith 0 (turn-off the half-sine) or 1 (turn-on
the half-sine)

hfr=0.0; % amplitude of high frequency oscillation vs.
half-sine inpulse

epi=0.01;

%% Input Base excitation

% input signal at x3

tp=0:1./fs:delta;
```

```

t=tp';

ai=hsr*amp*sin(wni*t).*(heaviside(t)-heaviside(t-
pi/wni))+hfr*amp*sin(wni*(t-
pi/2/wni+pi/2/wni)).*heaviside(t-
pi/2/wni+pi/2/wni).*exp(-epi*wnh*(t-pi/2/wni+pi/2/wnh));

%% figure(3)

% plot(t,ai);

[ff Y]=fftspc(ai,fs); % fft

Yn=interp1(ff, Y, A_F, 'linear');

Yr=TF.*Yn;

A_Fn=A_F(101:430);

Yrn=Yr(101:430);

[ap nfp]=max(Yrn);

fp=A_Fn(nfp);%nfp L1=89; L2=206; L3=16

omp=fp*Hz2rps;

lamda=(1-exp(-eta*omp*delta))/(eta*omp*delta);

ar=ap/lamda/amp;

end

%% this is the code to plot the gama vs. timp, presented in
Chapter 4.

clc

clear all

impfreq=logspace(-6,-4,1000);

load PWBTF

for i = 1:length(impfreq);

```

```
[amri natF]=ampf01(impfreq(i));  
amrip(i)=amri;  
natFp(i)=natF;  
end  
  
figure (1)  
plot(impfreq,amrip)  
  
figure (2)  
plot(impfreq,natFp)
```

A3. Laminated PWB's orthotropic property calculation

In the literature, PWB laminates are usually modeled as a homogeneous isotropic or orthotropic material. In reality, the PWB laminate is much more complicated than a homogeneous board. The recommended built-up multilayer PWB technology used in this study contains up to 17 layers [7] including solder masks, dielectric and conductor layers.

Under shock and impact loading, PWB is subjected to vibration of high frequency. According to the classical lamination theory [122], since both extensional stiffness and flexural rigidity are going to be calculated, not only the properties of each layer but also the sequence of the layers are necessary to be included in the laminated shell simulation in FEA.

$$\begin{Bmatrix} N_x \\ N_y \\ N_{xy} \end{Bmatrix} = \begin{bmatrix} A_{11} & A_{12} & A_{16} \\ A_{12} & A_{22} & A_{26} \\ A_{16} & A_{26} & A_{66} \end{bmatrix} \begin{Bmatrix} \epsilon_x^0 \\ \epsilon_y^0 \\ \gamma_{xy}^0 \end{Bmatrix} \quad (23)$$

A brief review of the relevant equations which are being used in this study, N_x, N_y and N_{xy} are in-plane normal and shear forces per unit length. ϵ_x, ϵ_y and γ_{xy} are in-plane normal and shear strain components. \mathbf{A} is the 2-D extensional stiffness matrix.

$$\begin{Bmatrix} M_x \\ M_y \\ M_{xy} \end{Bmatrix} = \begin{bmatrix} D_{11} & D_{12} & D_{16} \\ D_{12} & D_{22} & D_{26} \\ D_{16} & D_{26} & D_{66} \end{bmatrix} \begin{Bmatrix} \kappa_x^0 \\ \kappa_y^0 \\ \kappa_{xy}^0 \end{Bmatrix} \quad (24)$$

M_x, M_y and M_{xy} are in-plane bending and twisting moments per unit length.

κ_x, κ_y and κ_{xy} are the in-plane bending and twisting curvature components. D is the 2-D flexural stiffness matrix. The A and D matrices are obtained from the mechanical stiffness properties and thickness of individual layers, as follows:

$$A_{ij} = \sum_{k=1}^N (\bar{Q}_{ij})_k (z_k - z_{k-1}) \quad (25)$$

\bar{Q}_{ij} is the reduced stiffness matrix (stiffness matrix for plane stress) of each layer,

which is defined in terms of the engineering constants. z_k is the distance of the k^{th} layer from the reference plane of the symmetric laminate. Since the extensional stiffness A of the laminate is only related to the thickness of each layer, they are independent of the sequence of the layers. However, bending stiffness is related to z to the power of 3, and a different sequence of laminate can result in a dramatic difference of bending stiffness. Thus, it is necessary to include the laminate stack-up sequence for flexural stiffness of the PWBs when modeling the flexural response under shock and impact loading.

In this study, the PWB laminate contains 8 conductor layers, 2 RCF layers and 5 layers of FR-4. Material properties for all three types of plies are listed. E is Young's modulus, ν is Poisson's ratio and G is shear modulus of each ply material. FR-4 plies are modeled as orthotropic materials to reflect the effect of the reinforcing glass fabric; the conductor layers are made of copper meshes and are also modeled as

orthotropic materials. The homogenized orthotropic mechanical stiffness properties are obtained via FEA sub-models of the copper mesh, The RCF layer is modeled as an isotropic material. Conductor layer and FR-4 are both modeled as transverse isotropic materials.

$$D_{ij} = \frac{1}{3} \sum_{k=1}^N (\bar{Q}_{ij})_k (z_k^3 - z_{k-1}^3) \quad (26)$$

Table 19: Material Properties for PWB Laminate

Conductor layer		FR-4		RCF layer	
E ₁₁ (GPa)	24.53	E ₁₁ (GPa)	22.02	E (GPa)	5.92
E ₂₂ (GPa)	24.53	E ₂₂ (GPa)	22.02	v	0.30
E ₃₃ (GPa)	63.68	E ₃₃ (GPa)	9.63	G (GPa)	2.28
v ₁₂	0.57	v ₁₂	0.14		
v ₂₃	0.13	v ₂₃	0.37		
v ₁₃	0.13	v ₁₃	0.37		
G ₁₂ (GPa)	27.57	G ₁₂ (GPa)	3.70		
G ₂₃ (GPa)	19.91	G ₂₃ (GPa)	2.90		
G ₁₃ (GPa)	19.91	G ₁₃ (GPa)	2.90		

The material property of the MEMS substrate FR-4 is consistent with [123]. However, the Young's modulus (E₁, E₂ and E₃) of the FR-4 used in the PWB laminate analysis (both in Level 1 and Level 2 models) are scaled by a factor of 1.16, in order to match the overall extensional stiffness matrix and natural frequency of the

PWB with the experiments. The material property values in the ABAQUS inp file are calculated based on the Young's modulus, Poisson's ratio and shear modulus.

A4. Material properties used in simulation, Chapter4

In this section, material properties of all the materials in Table 4 are listed [103].

Table 20: Isotropic Elastic Material Properties

Material	Density(g/cc)	E (GPa)	ν
Au	19.30	66.70	0.29
Brass	8.80	110.00	0.34
Cu	8.93	102.00	0.34
Die attach	2.00	3.00	0.35
Sillicon	2.33	3.00	0.35
Solder Mask	1.60	6.00	0.35
Solder	7.33	47.00	0.35
RCF layer	1.00	5.92	0.30

Table 21: Orthotropic Elastic Material Properties

Properties	Conductor layer	FR-4
Density (g/cc)	5.53	2.00
E_{11} (GPa)	24.53	22.02
E_{22} (GPa)	24.53	22.02
E_{33} (GPa)	63.68	9.63
ν_{12}	0.57	0.14
ν_{23}	0.13	0.37
ν_{13}	0.13	0.37
G_{12} (GPa)	27.57	3.70
G_{23} (GPa)	19.91	2.90
G_{13} (GPa)	19.91	2.90

Table 22: Plastic Material Property of Au

Plastic Strain	Yield Stress (MPa)
0.000	89.18
0.002	106.91
0.005	120.17
0.010	130.47
0.025	145.76
0.042	156.73
0.093	176.00

Table 23: Strain Rate Dependent Plastic Property of Solder (MPa)

Plastic strain	Strain rate (1/s)					
	0	0.001	0.1	10	1000	5000
0.000	11.00	23.67	35.79	59.49	105.86	130.93
0.001	11.84	25.48	38.52	64.03	113.93	140.91
0.007	13.16	28.31	42.80	71.15	126.60	156.58
0.027	15.36	33.05	49.97	83.07	147.81	182.81
0.044	16.56	35.65	53.90	89.59	159.41	197.16
0.280	25.04	53.88	81.47	135.42	240.96	298.02

Bibliography

- [1] S. Goyal, S. Upasani, and D. M. Patel, "Improving impact tolerance of portable electronic products: Case study of cellular phones," *Exp. Mech.*, vol. 39, no. 1, pp. 43–52, Mar. 1999.
- [2] C. T. Lim, C. W. Ang, L. B. Tan, S. K. W. Seah, and E. H. Wong, "Drop impact survey of portable electronic products," in *Electronic Components and Technology Conference, 2003. Proceedings. 53rd*, 2003, pp. 113–120.
- [3] A. F. Askari Farahani, M. Al-Bassyiouni, and A. Dasgupta, "Shock and Dynamic Loading in Portable Electronic Assemblies: Modeling and Simulation Results," *J. Electron. Packag.*, vol. 133, no. 4, pp. 041012–041012, Dec. 2011.
- [4] S. T. Douglas, M. Al-Bassyiouni, and A. Dasgupta, "Experiment and Simulation of Board Level Drop Tests With Intentional Board Slap at High Impact Accelerations," *IEEE Trans. Compon. Packag. Manuf. Technol.*, vol. 4, no. 4, pp. 569–580, Apr. 2014.
- [5] S. Douglas, J. Meng, J. Akman, I. Yildiz, M. Al-Bassyiouni, and A. Dasgupta, "The effect of secondary impacts on PWB-level drop tests at high impact accelerations," in *Thermal, Mechanical and Multi-Physics Simulation and Experiments in Microelectronics and Microsystems (EuroSimE), 2011 12th International Conference on*, 2011, pp. 1/6 –6/6.
- [6] J. Meng, T. Mattila, A. Dasgupta, M. Sillanpaa, R. Jaakkola, G. Luo, and K. Andersson, "Drop qualification of MEMS components in handheld electronics at extremely high accelerations," in *2012 13th IEEE Intersociety Conference on Thermal and Thermomechanical Phenomena in Electronic Systems (ITherm)*, 2012, pp. 1020 –1027.
- [7] JESD22-B111, "Board Level Drop Test Method of Components for Handheld Electronic Products." JEDEC Solid State Technology Association, Arlington, VA, USA, Jul-2003.
- [8] J. Wu, G. Song, C.-P. Yeh, and K. Wyatt, "Drop/impact simulation and test validation of telecommunication products," in *The Sixth Intersociety Conference on Thermal and Thermomechanical Phenomena in Electronic Systems, 1998. I THERM '98*, 1998, pp. 330–336.
- [9] C. T. Lim and Y. J. Low, "Investigating the drop impact of portable electronic products," in *Electronic Components and Technology Conference, 2002. Proceedings. 52nd*, 2002, pp. 1270–1274.
- [10] Y. C. Ong, V. P. W. Shim, T. C. Chai, and C. T. Lim, "Comparison of mechanical response of PCBs subjected to product-level and board-level drop impact tests," in *Electronics Packaging Technology, 2003 5th Conference (EPTC 2003)*, 2003, pp. 223–227.
- [11] S. K. W. Seah, E. H. Wong, Y. W. Mai, R. Rajoo, and C. T. Lim, "Failure mechanisms of interconnections in drop impact," in *Electronic Components and Technology Conference, 2006. Proceedings. 56th*, 2006, p. 9 pp.–.
- [12] J. Varghese and A. Dasgupta, "Test methodology for durability estimation of surface mount interconnects under drop testing conditions," *Microelectron. Reliab.*, vol. 47, no. 1, pp. 93–103, Jan. 2007.

- [13] J. Varghese and A. Dasgupta, "An experimental approach to characterize rate-dependent failure envelopes and failure site transitions in surface mount assemblies," *Microelectron. Reliab.*, vol. 47, no. 7, pp. 1095–1102, Jul. 2007.
- [14] E. H. Wong, S. K. W. Seah, W. D. van Driel, J. F. J. M. Caers, N. Owens, and Y.-S. Lai, "Advances in the drop-impact reliability of solder joints for mobile applications," *Microelectron. Reliab.*, vol. 49, no. 2, pp. 139–149, Feb. 2009.
- [15] G. . Li and F. . Shemansky Jr., "Drop test and analysis on micro-machined structures," *Sens. Actuators Phys.*, vol. 85, no. 1–3, pp. 280–286, Aug. 2000.
- [16] V. T. Srikar and S. D. Senturia, "The reliability of microelectromechanical systems (MEMS) in shock environments," *J. Microelectromechanical Syst.*, vol. 11, no. 3, pp. 206–214, 2002.
- [17] S. Goyal, S. S. Upasani, and D. M. Patel, "Designing best-in-class impact-tolerant cellular phones and other portable products," *Bell Labs Tech. J.*, vol. 3, no. 3, pp. 159–174, 1998.
- [18] S. K. W. Seah, C. T. Lim, E. H. Wong, V. B. C. Tan, and V. P. W. Shim, "Mechanical response of PCBs in portable electronic products during drop impact," in *Electronics Packaging Technology Conference, 2002. 4th*, 2002, pp. 120–125.
- [19] J. Karppinen, J. Li, J. Pakarinen, T. T. Mattila, and M. Paulasto-Kröckel, "Shock impact reliability characterization of a handheld product in accelerated tests and use environment," *Microelectron. Reliab.*, vol. 52, no. 1, pp. 190–198.
- [20] T. Y. Tee, J. Luan, E. Pek, C.-T. Lim, and Z. Zhong, "Advanced experimental and simulation techniques for analysis of dynamic responses during drop impact," in *Electronic Components and Technology Conference, 2004. Proceedings. 54th*, 2004, vol. 1, pp. 1088–1094 Vol.1.
- [21] K. . Low, "Drop-impact cushioning effect of electronics products formed by plates," *Adv. Eng. Softw.*, vol. 34, no. 1, pp. 31–50, Jan. 2003.
- [22] H. Shan, J. Su, F. Badiu, J. Zhu, and L. Xu, "Modeling and simulation of multiple impacts of falling rigid bodies," *Math. Comput. Model.*, vol. 43, no. 5–6, pp. 592–611, Mar. 2006.
- [23] L. B. Tan, C. W. Ang, C. T. Lim, V. B. C. Tan, and X. Zhang, "Modal and impact analysis of modern portable electronic products," in *Electronic Components and Technology Conference, 2005. Proceedings. 55th*, 2005, pp. 645–653 Vol. 1.
- [24] S. Goyal, "The Dynamics of Clattering I: Equation of Motion and Examples," *J Dyn Sys Meas Control J. Dyn. Syst. Meas. Control*, vol. 120, no. 1, p. 83, 1998.
- [25] S. Goyal, "The Dynamics of Clattering II: Global Results and Shock Protection," *J Dyn Sys Meas Control J. Dyn. Syst. Meas. Control*, vol. 120, no. 1, p. 94, 1998.
- [26] T. T. Mattila, L. Vajavaara, J. Hokka, E. Hussa, M. Makela, and V. Halkola, "An approach to board-level drop reliability evaluation with improved correlation with use conditions," in *Electronic Components and Technology Conference (ECTC), 2013 IEEE 63rd*, 2013, pp. 1259–1268.
- [27] J. B. Hart and R. B. Herrmann, "Energy Transfer in One-Dimensional Collisions of Many Objects," *Am. J. Phys.*, vol. 36, pp. 46–48, Jan. 1968.

- [28] W. G. Harter, "Velocity Amplification in Collision Experiments Involving Superballs," *Am. J. Phys.*, vol. 39, no. 6, pp. 656–663, Jun. 1971.
- [29] J. D. Kerwin, "Velocity, Momentum, and Energy Transmissions in Chain Collisions," *Am. J. Phys.*, vol. 40, no. 8, pp. 1152–1158, Aug. 1972.
- [30] B. Rodgers, S. Goyal, G. Kelly, and M. Sheehy, "The Dynamics of Multiple Pair-Wise Collisions in a Chain for Designing Optimal Shock Amplifiers," *Shock Vib.*, vol. 16, no. 1, pp. 99–116, 2009.
- [31] G. Kelly, J. Punch, S. Goyal, and M. Sheehy, "Shock Pulse Shaping in a Small-Form Factor Velocity Amplifier," *Shock Vib.*, vol. 17, no. 6, pp. 787–802, 2010.
- [32] British Standards Institute, *Surface Mounting Technology. Environmental and Endurance Test Methods for Surface Mount Solder Joint. Cyclic Drop Test*. BSI Group, 2009.
- [33] P. Normalizacyjny, *Environmental Engineering (EE) - Environmental conditions and environmental tests for telecommunications equipment - Part 2-7: Specification of environmental tests - Portable and non-stationary use PN-ETSI EN 300 019-2-7 V3.0.1*. Polski Komitet Normalizacyjny, 2005.
- [34] D10 Committee, "Test Methods for Mechanical-Shock Fragility of Products, Using Shock Machines," ASTM International, 2010.
- [35] J. Luan, T. Y. Tee, E. Pek, C. T. Lim, and Z. Zhong, "Modal analysis and dynamic responses of board level drop test," in *Electronics Packaging Technology, 2003 5th Conference (EPTC 2003)*, 2003, pp. 233–243.
- [36] Y. Q. Wang, K. H. Low, F. X. Che, H. L. J. Pang, and S. P. Yeo, "Modeling and simulation of printed circuit board drop test," in *Electronics Packaging Technology, 2003 5th Conference (EPTC 2003)*, 2003, pp. 263–268.
- [37] E. H. Wong, R. Rajoo, Y. W. Mai, S. K. W. Sean, K. T. Tsai, and L. M. Yap, "Drop Impact: Fundamentals and Impact Characterisation of Solder Joints," in *Electronic Components and Technology Conference, 2005. Proceedings. 55th*, 2005, pp. 1202–1209.
- [38] G. M. Heaslip, J. M. Punch, B. A. Rodgers, C. Ryan, and M. Reid, "A stress-life methodology for ball grid array lead-free and tin-lead solder interconnects under impact conditions," in *Proceedings of the 6th International Conference on Thermal, Mechanical and Multi-Physics Simulation and Experiments in Micro-Electronics and Micro-Systems, 2005. EuroSimE 2005*, 2005, pp. 277–284.
- [39] J. Varghese, *Effect of Dynamic Flexural Loading on the Durability and Failure Site of Solder Interconnects of Printed Wiring Assemblies*. ProQuest, 2007.
- [40] J.-K. Lin, A. De Silva, D. Frear, Y. Guo, J.-W. Jang, L. Li, D. Mitchell, B. Yeung, and C. Zhang, "Characterization of lead-free solders and under bump metallurgies for flip-chip package," in *Electronic Components and Technology Conference, 2001. Proceedings., 51st*, 2001, pp. 455–462.
- [41] Y.-S. Lai, P. C. Chen, C.-L. Yeh, and J. C. B. Lee, "The effect of IMC microstructure of solder joint on the mechanical drop performance in SnxAgCu and SnAgCuX CSP package," in *Electronic Components and Technology Conference, 2006. Proceedings. 56th*, 2006, p. 5 pp.–.
- [42] T. T. Mattila, P. Marjamaki, L. Nguyen, and J. K. Kivilahti, "Reliability of chip scale packages under mechanical shock loading," in *Electronic Components and Technology Conference, 2006. Proceedings. 56th*, 2006, p. 6 pp.–.

- [43] D. Y. R. Chong, K. Ng, J. Y. N. Tan, P. T. H. Low, J. H. L. Pang, and F. X. Che, "Drop test reliability assessment of leaded amp; lead-free solder joints for IC packages," in *Electronics Packaging Technology Conference, 2004. EPTC 2004. Proceedings of 6th*, 2004, pp. 210–217.
- [44] D. Y. R. Chong, F. X. Che, L. H. Xu, H. J. Toh, J. H. L. Pang, B. K. Xiong, and B. K. Lim, "Performance assessment on board-level drop reliability for chip scale packages (fine-pitch BGA)," in *Electronic Components and Technology Conference, 2006. Proceedings. 56th*, 2006, p. 8 pp.
- [45] T. C. Chai, S. Quek, W. Y. Hnin, E. H. Wong, J. Chia, Y. Y. Wang, Y. M. Tan, and C. T. Lim, "Board level drop test reliability of IC packages," in *Electronic Components and Technology Conference, 2005. Proceedings. 55th*, 2005, pp. 630–636 Vol. 1.
- [46] L. Xu and J. H. L. Pang, "Effect of intermetallic and Kirkendall voids growth on board level drop reliability for SnAgCu lead-free BGA solder joint," in *Electronic Components and Technology Conference, 2006. Proceedings. 56th*, 2006, p. 8 pp.–.
- [47] D. Tian, H. Chen, and C. Wang, "Effect of thermal aging on microstructure, shear and mechanical shock failures for solder ball bonding joint," in *2005 6th International Conference on Electronic Packaging Technology*, 2005, pp. 1–7.
- [48] Z. Sherf, P. Hopstone, G. Ostrovski, R. Klein, and D. Yehuda, "Problems in the Analysis of a Shock Sequence with Application to Gunfire Analysis and Simulation," *J. IEST*, vol. 45, no. 1, pp. 161–177, Sep. 2002.
- [49] U. Koro, M. Hiroshi, U. Hideo, and P. J., "Impact Reduction of an Automotive Occupant by 'Ride Down' Effect in Head-on Collision," *Trans. Jpn. Soc. Mech. Eng. C*, vol. 70, no. 697, pp. 2624–2630, 2004.
- [50] K. Jacobsen, D. Tyrell, and B. Perlman, "Rail car impact tests with steel coil: collision dynamics," in *Rail Conference, 2003. Proceedings of the 2003 IEEE/ASME Joint*, 2003, pp. 73–82.
- [51] R. . Newton, "Fragility assessment : theory and test procedure." Monterey Research Laboratory, 1968.
- [52] S. Goyal, J. M. Papadopoulos, and P. A. Sullivan, "Shock Protection of Portable Electronic Products: Shock Response Spectrum, Damage Boundary Approach, and Beyond," *Shock Vib.*, vol. 4, no. 3, pp. 169–191, 1997.
- [53] C. Y. Zhou and T. X. Yu, "Analytical models for shock isolation of typical components in portable electronics," *Int. J. Impact Eng.*, vol. 36, no. 12, pp. 1377–1384, Dec. 2009.
- [54] J. Zhao and L. J. Garner, "Mechanical modeling and analysis of board level drop test of electronic package," in *Electronic Components and Technology Conference, 2006. Proceedings. 56th*, 2006, p. 7 pp.–.
- [55] E. H. Wong, K. M. Lim, N. Lee, S. Seah, C. Hoe, and J. Wang, "Drop impact test - mechanics physics of failure," in *Electronics Packaging Technology Conference, 2002. 4th*, 2002, pp. 327 – 333.
- [56] J. Luan, T. Y. Tee, K. Goh, H. S. Ng, X. Baraton, R. Bronner, M. Sorrieul, E. Hussa, T. Reinikainen, and A. Kujala, "Drop impact life prediction model for lead-free BGA packages and modules," in *Proceedings of the 6th International Conference on Thermal, Mechanical and Multi-Physics Simulation and*

- Experiments in Micro-Electronics and Micro-Systems, 2005. EuroSimE 2005, 2005, pp. 559–565.*
- [57] L. Zhu and W. Marcinkiewicz, “Drop impact reliability analysis of CSP packages at board and product levels through modeling approaches,” *IEEE Trans. Compon. Packag. Technol.*, vol. 28, no. 3, pp. 449–456, 2005.
- [58] Q. Yu, H. Kikuchi, S. Ikeda, M. Shiratori, M. Kakino, and N. Fujiwara, “Dynamic behavior of electronics package and impact reliability of BGA solder joints,” in *The Eighth Intersociety Conference on Thermal and Thermomechanical Phenomena in Electronic Systems, 2002. IThERM 2002, 2002, pp. 953–960.*
- [59] V. Gektin, A. Bar-Cohen, and S. Witzman, “Coffin-Manson based fatigue analysis of underfilled DCAs,” *IEEE Trans. Compon. Packag. Manuf. Technol. Part A*, vol. 21, no. 4, pp. 577–584, Dec. 1998.
- [60] J. H. L. Pang, T.-I. Tan, and S. K. Sitaraman, “Thermo-mechanical analysis of solder joint fatigue and creep in a flip chip on board package subjected to temperature cycling loading,” in *48th IEEE Electronic Components and Technology Conference, 1998, 1998, pp. 878–883.*
- [61] A. Dasgupta, C. Oyan, D. Barker, and M. Pecht, “Solder Creep-Fatigue Analysis by an Energy-Partitioning Approach,” *J. Electron. Packag.*, vol. 114, no. 2, pp. 152–160, Jun. 1992.
- [62] J. Morrow, “Cyclic Plastic Strain Energy and Fatigue of Metals,” in *Internal Friction, Damping, and Cyclic Plasticity*, B. Lazan, Ed. 100 Barr Harbor Drive, PO Box C700, West Conshohocken, PA 19428-2959: ASTM International, 1965, pp. 45–45–43.
- [63] T. Y. Tee, H. S. Ng, C. T. Lim, E. Pek, and Z. Zhong, “Board level drop test and simulation of TFBGA packages for telecommunication applications,” in *Electronic Components and Technology Conference, 2003. Proceedings. 53rd, 2003, pp. 121–129.*
- [64] P. Lall, D. R. Panchagade, P. Choudhary, S. Gupte, and J. C. Suhling, “Failure-Envelope Approach to Modeling Shock and Vibration Survivability of Electronic and MEMS Packaging,” *IEEE Trans. Compon. Packag. Technol.*, vol. 31, no. 1, pp. 104–113, 2008.
- [65] F. Ellyin, *Fatigue Damage, Crack Growth and Life Prediction*. Springer Science & Business Media, 1997.
- [66] L. . Jr Coffin, *A Study of the Effects of Cyclic Thermal Stresses on a Ductile Metal*. Knolls Atomic Power Laboratory, 1953.
- [67] S. S. Manson, *Thermal stress and low-cycle fatigue*. McGraw-Hill, 1966.
- [68] P. W. Bridgman, “Effects of High Shearing Stress Combined with High Hydrostatic Pressure,” *Phys. Rev.*, vol. 48, no. 10, pp. 825–847, Nov. 1935.
- [69] F. A. McClintock, S. M. Kaplan, and C. A. Berg, “Ductile fracture by hole growth in shear bands,” *Int. J. Fract. Mech.*, vol. 2, no. 4, pp. 614–627, Dec. 1966.
- [70] W. A. S. A. Brownrigg, “The influence of hydrostatic pressure on the flow stress and ductility of a spheroidized 1045 steel,” *Acta Metall.*, vol. 31, no. 8, pp. 1141–1150, 1983.

- [71] D. F. Socie and J. Morrow, "Review of Contemporary Approaches to Fatigue Damage Analysis," in *Risk and Failure Analysis for Improved Performance and Reliability*, J. J. Burke and V. Weiss, Eds. Springer US, 1980, pp. 141–194.
- [72] S. S. Manson and G. R. Halford, "Practical implementation of the double linear damage rule and damage curve approach for treating cumulative fatigue damage," *Int. J. Fract.*, vol. 17, no. 2, pp. 169–192, Apr. 1981.
- [73] A. Varvani-Farahani, "Silicon MEMS components: a fatigue life assessment approach," *Microsyst. Technol.*, vol. 11, no. 2–3, pp. 129–134, Feb. 2005.
- [74] T. Hauck, G. Li, A. McNeill, H. Knoll, M. Ebert, and J. Bagdahn, "Drop Simulation and Stress Analysis of MEMS Devices," in *7th International Conference on Thermal, Mechanical and Multiphysics Simulation and Experiments in Micro-Electronics and Micro-Systems, 2006. EuroSime 2006*, 2006, pp. 1–5.
- [75] D. M. Tanner, J. A. Walraven, K. Helgesen, L. W. Irwin, F. Brown, N. F. Smith, and N. Masters, "MEMS reliability in shock environments," in *Reliability Physics Symposium, 2000. Proceedings. 38th Annual 2000 IEEE International*, 2000, pp. 129–138.
- [76] H. R. Shea, "Reliability of MEMS for space applications," in *Proc. of SPIE*.
- [77] S. Mariani, A. Ghisi, A. Corigliano, and S. Zerbini, "Modeling Impact-induced Failure of Polysilicon MEMS: A Multi-scale Approach," *Sensors*, vol. 9, no. 1, pp. 556–567, Jan. 2009.
- [78] J. a. R. Bomidi, N. Weinzapfel, and F. Sadeghi, "Three-dimensional modelling of intergranular fatigue failure of fine grain polycrystalline metallic MEMS devices," *Fatigue Fract. Eng. Mater. Struct.*, vol. 35, no. 11, pp. 1007–1021, 2012.
- [79] W. Merlijn van Spengen, "MEMS reliability from a failure mechanisms perspective," *Microelectron. Reliab.*, vol. 43, no. 7, pp. 1049–1060, Jul. 2003.
- [80] A. Ghisi, F. Fachin, S. Mariani, and S. Zerbini, "Multi-scale analysis of polysilicon MEMS sensors subject to accidental drops: Effect of packaging," *Microelectron. Reliab.*, vol. 49, no. 3, pp. 340–349, Mar. 2009.
- [81] F. Alsaleem, M. I. Younis, and R. Miles, "An Investigation Into the Effect of the PCB Motion on the Dynamic Response of MEMS Devices Under Mechanical Shock Loads," *J. Electron. Packag.*, vol. 130, no. 3, pp. 031002–031002, Jul. 2008.
- [82] H. A. C. Tilmans, J. De Coster, P. Helin, V. Cherman, A. Jourdain, P. De Moor, B. Vandeveld, N. P. Pham, J. Zekry, A. Witvrouw, and I. De Wolf, "MEMS packaging and reliability: An undividable couple," *Microelectron. Reliab.*, vol. 52, no. 9–10, pp. 2228–2234, Sep. 2012.
- [83] T. C. Togami, W. E. Baker, and M. J. Forrestal, "A Split Hopkinson Bar Technique to Evaluate the Performance of Accelerometers," *J. Appl. Mech.*, vol. 63, no. 2, pp. 353–356, Jun. 1996.
- [84] H. D. Danny Joe Frew, "A modified Hopkinson pressure bar experiment to evaluate a damped piezoresistive MEMS accelerometer," 2009.
- [85] M. Pandey, K. Aubin, M. Zalalutdinov, R. B. Reichenbach, A. T. Zehnder, R. H. Rand, and H. G. Craighead, "Analysis of Frequency Locking in Optically

- Driven MEMS Resonators,” *J. Microelectromechanical Syst.*, vol. 15, no. 6, pp. 1546–1554, Dec. 2006.
- [86] Z. J. Zhou, L. Rufer, E. Salze, S. Ollivier, and M. Wong, “Wide-band aero-acoustic microphone with improved low-frequency characteristics,” in *2013 Transducers Eurosensors XXVII: The 17th International Conference on Solid-State Sensors, Actuators and Microsystems (TRANSDUCERS EUROSENSORS XXVII)*, 2013, pp. 1835–1838.
- [87] M. Sheehy, M. Reid, J. Punch, S. Goyal, and G. Kelly, “The failure mechanisms of micro-scale cantilevers in shock and vibration stimuli,” in *Symposium on Design, Test, Integration and Packaging of MEMS/MOEMS, 2008. MEMS/MOEMS 2008*, 2008, pp. 2–7.
- [88] L. Pochhammer, “Ueber die Fortpflanzungsgeschwindigkeiten kleiner Schwingungen in einem unbegrenzten isotropen Kreiscylinder.,” *J. Für Reine Angew. Math.*, vol. 81, pp. 324–336, 1876.
- [89] R. M. Davies, “A Critical Study of the Hopkinson Pressure Bar,” *Philos. Trans. R. Soc. Lond. Math. Phys. Eng. Sci.*, vol. 240, no. 821, pp. 375–457, Jan. 1948.
- [90] A. H. Shah and S. K. Datta, “Harmonic waves in a periodically laminated medium,” *Int. J. Solids Struct.*, vol. 18, no. 5, pp. 397–410, 1982.
- [91] A. N. Podlipenets, “Propagation of harmonic waves in orthotropic materials with a periodic structure,” *Sov. Appl. Mech.*, vol. 20, no. 7, pp. 604–607, Jul. 1984.
- [92] C.-T. Sun, J. D. Achenbach, and G. Herrmann, “Time-Harmonic Waves in a Stratified Medium Propagating in the Direction of the Layering,” *J. Appl. Mech.*, vol. 35, no. 2, pp. 408–411, Jun. 1968.
- [93] B. Hu, W. Schiehlen, and P. Eberhard, “Comparison of Analytical and Experimental Results for Longitudinal Impacts on Elastic Rods,” *J. Vib. Control*, vol. 9, no. 1–2, pp. 157–174, Jan. 2003.
- [94] J. Kimberley, J. Lambros, I. Chasiotis, J. Pulskamp, R. Polcawich, and M. Dubey, “A Hybrid Experimental/Numerical Investigation of the Response of Multilayered MEMS Devices to Dynamic Loading,” *Exp. Mech.*, vol. 50, no. 4, pp. 527–544, Jun. 2009.
- [95] S. Douglas, M. Al-Bassyiouni, and A. Dasgupta, “Simulation of drop testing at extremely high accelerations,” in *2010 11th International Conference on Thermal, Mechanical Multi-Physics Simulation, and Experiments in Microelectronics and Microsystems (EuroSimE)*, 2010, pp. 1–7.
- [96] P. Lall, K. Patel, R. Lowe, M. Strickland, J. Blanche, D. Geist, and R. Montgomery, “Modeling and reliability characterization of area-array electronics subjected to high-g mechanical shock up to 50,000g,” in *Electronic Components and Technology Conference (ECTC), 2012 IEEE 62nd*, 2012, pp. 1194–1204.
- [97] S. T. Douglas, “High Accelerations Produced Through Secondary Impact And its Effect on Reliability of Printed Wiring Assemblies,” Thesis, 2010.
- [98] J. Li, M. Broas, J. Raami, T. T. Mattila, and M. Paulasto-Kröckel, “Reliability assessment of a MEMS microphone under mixed flowing gas environment and shock impact loading,” *Microelectron. Reliab.*, vol. 54, no. 6–7, pp. 1228–1234, Jun. 2014.

- [99] J. W. McPherson, *Reliability Physics and Engineering: Time-To-Failure Modeling*. Springer, 2010.
- [100] J. Gomez and C. Basaran, "A thermodynamics based damage mechanics constitutive model for low cycle fatigue analysis of microelectronics solder joints incorporating size effects," *Int. J. Solids Struct.*, vol. 42, no. 13, pp. 3744–3772, Jun. 2005.
- [101] D. Farley, A. Dasgupta, Y. Zhou, J. F. J. Caers, and J. W. C. De Vries, "Fatigue model based on average cross-section strain of Cu trace cyclic bending," in *2011 12th International Conference on Thermal, Mechanical and Multi-Physics Simulation and Experiments in Microelectronics and Microsystems (EuroSimE)*, 2011, pp. 1/10–10/10.
- [102] A. Dasgupta, P. Sharma, and K. Upadhyayula, "Micro-Mechanics of Fatigue Damage in Pb-Sn Solder Due to Vibration and Thermal Cycling," *Int. J. Damage Mech.*, vol. 10, no. 2, pp. 101–132, Apr. 2001.
- [103] J. Meng, T. Mattila, A. Dasgupta, M. Sillanpaa, R. Jaakkola, K. Andersson, and E. Hussa, "Testing and multi-scale modeling of drop and impact loading of complex MEMS microphone assemblies," in *2012 13th International Conference on Thermal, Mechanical and Multi-Physics Simulation and Experiments in Microelectronics and Microsystems (EuroSimE)*, 2012, pp. 1/8 – 8/8.
- [104] J. Meng and A. Dasgupta, "Influence of Secondary Impact on Printed Wiring Assemblies Part I: High Frequency 'Breathing Mode' Deformations in the Printed Wiring Board," *J. Electron. Packag.*, Jan. 2016.
- [105] P. Lall, S. Shantaram, J. Suhling, and D. Locker, "Stress–Strain Behavior of SAC305 at High Strain Rates," *J. Electron. Packag.*, vol. 137, no. 1, pp. 011010–011010, Mar. 2015.
- [106] P. Lall, N. Kothari, and J. Glover, "Mechanical Shock Reliability Analysis and Multiphysics Modeling of MEMS Accelerometers in Harsh Environments," p. V003T07A007, Jul. 2015.
- [107] N. Raghunathan, W. Tsutsui, W. Chen, and D. Peroulis, "A single crystal silicon low-g switch tolerant to impact accelerations up to 24,000 g," in *2015 Transducers - 2015 18th International Conference on Solid-State Sensors, Actuators and Microsystems (TRANSDUCERS)*, 2015, pp. 1144–1147.
- [108] Meng, Jingshi and Dasgupta, Abhijit, "Influence of Secondary Impact on Failure Modes in PWAs with High Resonant Frequency," in *ASME International Technical Conference and Exhibition on Packaging and Integration of Electronic and Photonic Microsystems (InterPACK)*, San Francisco, CA, July 6-9, 2015, 2015, pp. InterPACKICNMM2015–48669.
- [109] S. T. Douglas, M. Al-Bassyiouni, A. Dasgupta, K. Gilman, and A. Brown, "Simulation of Secondary Contact to Generate Very High Accelerations," *J. Electron. Packag.*, vol. 137, no. 3, pp. 031011–031011, Sep. 2015.
- [110] A. Zhang, "High acceleration board level reliability drop test using Dual Mass Shock Amplifier," in *Electronic Components and Technology Conference (ECTC)*, 2014 IEEE 64th, 2014, pp. 1441–1448.

- [111] E. Habtour, M. Paulus, and A. Dasgupta, “Modeling Approach for Predicting the Rate of Frequency Change of Notched Beam Exposed to Gaussian Random Excitation,” *Shock Vib.*, vol. 2014, p. e164039, Feb. 2014.
- [112] A. L. Morales, A. J. Nieto, J. M. Chicharro, and P. Pintado, “An adaptive pneumatic system for the attenuation of random vibrations,” *J. Vib. Control*, vol. 21, no. 5, pp. 907–918, Apr. 2015.
- [113] B. Balachandran and E. Magrab, *Vibrations*. Cengage Learning, 2008.
- [114] Dassault Systemes, “Contact pressure-overclosure relationships.” 2012.
- [115] J. A. Greenwood and J. B. P. Williamson, “Contact of Nominally Flat Surfaces,” *Proc. R. Soc. Lond. Math. Phys. Eng. Sci.*, vol. 295, no. 1442, pp. 300–319, Dec. 1966.
- [116] A. A. Polycarpou and I. Etsion, “Analytical Approximations in Modeling Contacting Rough Surfaces,” *J. Tribol.*, vol. 121, no. 2, pp. 234–239, Apr. 1999.
- [117] X. Shi and A. A. Polycarpou, “Measurement and Modeling of Normal Contact Stiffness and Contact Damping at the Meso Scale,” *J. Vib. Acoust.*, vol. 127, no. 1, pp. 52–60, Mar. 2005.
- [118] S. P. Timoshenko, *Vibration Problems in Engineering*. John Wiley & Sons, 1990.
- [119] H. Kolsky, *Stress Waves in Solids*. Courier Corporation, 1963.
- [120] J. Liu, D. T. Martin, K. Kadirvel, T. Nishida, L. Cattafesta, M. Sheplak, and B. P. Mann, “Nonlinear model and system identification of a capacitive dual-backplate MEMS microphone,” *J. Sound Vib.*, vol. 309, no. 1–2, pp. 276–292, Jan. 2008.
- [121] E. H. Wong, “Dynamics Of Board-Level Drop Impact,” *J. Electron. Packag.*, vol. 127, no. 3, pp. 200–207, Jul. 2004.
- [122] R. M. Jones, *Mechanics Of Composite Materials*. CRC Press, 1998.
- [123] S. M. Bhandaraka, “Thermomechanical Analysis and Fatigue Life Cycle Prediction of Plated-Through Holes in Multilayered Printed Wiring Board,” University of Maryland, 1992.